Simultaneous Registration and Segmentation Coupling Using the Jensen Rényi Divergence for Adaptive Radiotherapy

Daniel Markel

Doctor of Philosophy

Physics

McGill University
Montreal,Quebec
2016-08-15

A thesis submitted to McGill University in fulfillment of the requirements of the degree of doctor of philosophy

Copyright ©2016 Daniel Markel

DEDICATION

This document is dedicated to Alicia Klurfan, 1950-2003.

ACKNOWLEDGEMENTS

First and foremost I would like to thank my supervisor Issam El Naga, whom without his guidance and encyclopedic knowledge of imaging and image processing, I would not have been able to complete this doctorate. Dr. El Naga first suggested investigating the Jensen Rényi divergence while I was experimenting with a number of statistical divergence measures for the purposes of segmentation. His consistent support and encouragement has allowed that initial project to blossom into more advanced methods and hardware to properly evaluate it. Secondly I would like to sincerely thank Dr. Jan Seuntjens who despite a relentlessly busy schedule always found time to get involved and keep an open door policy for not just me but all students in the department. Thirdly, I would like to thank James Renaud for his technical support and encouragement through 5 years. I would also like to thank Joe Larkin and Pierre Léger for their significant contributions in designing and constructing the control circuit and respirator for the biomechanical phantom used in this thesis. They had very little to gain other than the challenge and willingness to help with this work and for that they have my gratitude and respect. Dr. Ives Levesque was paramount in his help evolving the design of the synthetic lesions used in the phantom along with his patience in designing MRI scanning protocols. Finally, I would like to thank Shirin Emadi for putting up with the late nights and whining.

ABSTRACT

Adaptive radiotherapy is the process of modifying radiation therapy treatment parameters in order to accommodate anatomical changes that manifest during a single fraction (ie. breathing) or over the course of treatment (ie. weight loss, tumor growth/recession). This process relies heavily on the use of imaging available within the treatment room such as cone-beam computed tomography (CBCT) and megavoltage computed tomography (MVCT), of which image quality is often sub-par compared to diagnostic scans. Plan adaptation often necessitates re-segmentation of targets and organs-at-risk as well as registration with previous scans which add time and cost to their implementation. In this dissertation, we attempt to address these problems through the investigation of a coupled segmentation and registration algorithm using the Jensen Rényi information objective. This divergence metric can be tuned to optimize performance depending on the image context such as mono-modal or multi-modal inputs and specific modalities by using a parameter α contained in the objective function. Coupling of the two processes has the potential to realize efficiencies and improved accuracy for both processes. We began by investigating the usage of the Rényi entropy for the sole purpose of segmentation using an active contour method based on the level-sets approach. The method was found to have direct applications to Positron Emission Tomography (PET), where noise, blurring and variable target contrast make segmentation a challenging prospect. Application to computed tomography (CT) and the combination of PET and CT was included to investigate the interplay of the α parameter with choice of imaging modality.

Registration was then coupled with segmentation using the same metric. The investigation focused on the performance effects of coupling, the alpha parameter with regard to registration and artificially modified noise and contrast. In conjunction with the joint segmentation and registration algorithm we developed a 4D biomechanical phantom using preserved swine lungs and a computer controlled respirator in order to evaluate this specific subset of algorithms. The system contains a set of synthetic lesions allowing us to determine segmentation ground truths. An airway bifurcation tracking pipeline was implemented in order to provide points of comparison for registration evaluation. Through the use of an in-house phantom we were able to show benefits from coupling and performance under a varying degree of contrast and noise conditions.

ABRÉGÉ

La radiothérapie adaptative est le processus de modification des paramètres des traitements par radiations afin de tenir compte des changements anatomiques qui se manifestent durant une seule fraction (exemple: respiration) ou au cours du traitement (exemple: perte de poids, croissance/récession tumorale). Ce processus repose en grande partie sur l'utilisation de l'imagerie disponible dans la salle de traitement telle que la tomodensitométrie par faisceau conique et la tomodensitomtrie par hautvoltage, dont la qualit est souvent inférieure par rapport aux scans diagnostiques. L'adaptation des plans de traitements nécessite souvent la re-segmentation des cibles et des organes risques ainsi que le recalage des images avec les scans précédemment effectués, ce qui ajoute un temps et un coût considérable à leur mise en œuvre. Dans cette thése, nous tentons de résoudre ces problèmes via l'étude d'un algorithme couplant simultanément la segmentation et le recalage d'image et utilisant l'information de Jensen Rényi comme objectif d'optimisation. Cette mesure de divergence permet un réglage de l'algorithme pour plusieurs combinaisons spécifiques d'imagerie en utilisant une pondération de la contribution du bruit de chaque image. Le couplage des deux processus a le potentiel d'améliorer la précision des deux processus pris séparément, tout en conservant l'efficacité de chacun. Tout d'abord, nous avons étudié l'utilisation de l'entropie de Rényi dans le seul but de la segmentation en utilisant une approche dite par "ensemble de niveau". Nous avons pu déterminer que la méthode conduit à des applications directes à la tomographie par émission de positrons (TEP), où le bruit, le flou et la variation de contraste de la cible font de la segmentation une tâche difficile. Une application à la tomodensitométrie (TDM) et la combinaison de la TEP et la TDM a été incluses afin d'étudier l'interaction du paramètre alpha avec le choix du type de modalité d'imagerie. Le recalage d'image a ensuite été couplé avec la segmentation en utilisant la même métrique et a été mis en œuvre. L'étude s'est concentrée sur les effets de performance du couplage du paramètre alpha vis- à-vis le recalage d'image et le bruit et le contraste d'image artificiellement modifiés. Conjointement avec l'algorithme de couplage de segmentation et de recalage d'image, nous avons développé un fantôme biomécanique 4D en utilisant des poumons de porcs préservés et un respirateur contrôlé par ordinateur afin d'évaluer ce sous-ensemble spécifique d'algorithmes. Les systèmes contiennent un ensemble de lésions synthétiques nous permettant de déterminer les valeurs réelles de segmentation. Une séquence de suivi des voies de bifurcation a été mise en œuvre afin de fournir des points de comparaison pour l'évaluation de l'algorithme de recalage d'image. Grâce à l'utilisation d'un fantôme que nous avons développé, nous avons pu démontrer les avantages du couplage et les performances pour diverses conditions de variation de bruit et de contraste d'image.

TABLE OF CONTENTS

| DED | OICATI | ON . | | i |
|------|--------------------------|----------------------------------|--|------------------|
| ACK | KNOWI | LEDGE | EMENTS ii | i |
| ABS | TRAC' | Т | | V |
| ABR | ÆÉGÉ | | | i |
| LIST | OFT | ABLES | S | i |
| LIST | OF F | IGURE | S xi | i |
| 1 | Introd | uction | | 1 |
| | 1.1 1.2 1.3 1.4 | Motiva Challe | nges | 1 2 5 7 |
| 2 | Backg | round: | Information Theory, Segmentation and Registration |) |
| | 2.1 | 2.1.1 2.1.2 2.1.3 2.1.4 | tal Beam Radiation Therapy | 3 5 1 |
| | 2.2 | Image 2.2.1 2.2.2 | Segmentation | 3 |
| | 2.3 | Regist: 2.3.1 2.3.2 2.3.3 2.3.4 | ration 29 Metric 31 Transformation 32 Interpolation 35 Optimization 37 | 1 2 5 |

| 0.4 | 2.3.5 Regularization |
|------|---|
| 2.4 | Information Theory |
| | el multimodality Segmentation Using Level Sets and the Jensen-Rényi |
| Di | vergence |
| 3.1 | Abstract |
| 3.2 | Introduction |
| 3.3 | Materials and Methods |
| | 3.3.1 Theory |
| | 3.3.2 Datasets and Validation |
| | 3.3.3 Clinical Studies |
| 3.4 | Results |
| | 3.4.1 Phantom Studies |
| | 3.4.2 Clinical PET Evaluation: Louvain Database 6 |
| | 3.4.3 Clinical PET/CT Evaluation: MAASTRO Database |
| 3.5 | Discussion |
| 3.6 | Conclusions |
| 3.7 | Acknowledgements |
| 3.8 | Conflict of Interest |
| 3.9 | Appendix |
| A 4D | |
| | Biomechanical Lung Phantom for Joint Segmentation/Registration |
| Ev | raluation |
| 4.1 | Abstract |
| 4.2 | Introduction |
| 4.3 | Materials and Methods |
| | 4.3.1 Lung Tissue |
| | 4.3.2 Computer Controlled Airflow System |
| | 4.3.3 Synthetic Targets |
| | 4.3.4 Bifurcation Tracking Pipeline |
| | 4.3.5 Scanning Parameters |
| | 4.3.6 Human Breathing Reproduction |
| 4.4 | Comparable Methods |
| 4.5 | Results |
| | 4.5.1 Bifurcation Tracking Evaluation |
| | 4.5.2 Breathing Reproducibility |
| | 4.5.3 Segmentation Evaluation |

| | | 4.5.4 Registration Evaluation |
|------|--------|--|
| | 4.6 | Discussion |
| | 4.7 | Conclusions |
| | 4.8 | Conflict of Interest |
| | 4.9 | Acknowledgements |
| 5 | Simult | aneous Registration/Segmentation using the Jensen Rényi Diver- |
| | gene | ce |
| | 5.1 | Abstract |
| | 5.2 | Introduction |
| | 5.3 | Materials and Methods |
| | | 5.3.1 Theoretical Background |
| | | 5.3.2 Adaptive Meshing |
| | | 5.3.3 4D Phantom Based Evaluation |
| | | 5.3.4 Noise Simulation |
| | | $5.3.5 Sensitivity \ Analysis \dots \dots \dots 145$ |
| | | 5.3.6 Coupling Dependency |
| | 5.4 | Discussion |
| | 5.5 | Conclusions |
| | 5.6 | Acknowledgements |
| | 5.7 | Appendix |
| | | 5.7.1 Continuing the 2D Case |
| | | 5.7.2 Extension to 3D |
| 6 | Conclu | asions |
| | 6.1 | Thesis Summary |
| | 6.2 | Discussion and Future Work |
| Refe | rences | |

LIST OF TABLES

| <u>Table</u> |] | page |
|--------------|--|------|
| 3–1 | Scanning parameters for the CBCT | 63 |
| 4–1 | Summary of the reproduction error for the three profiles | 115 |
| 4–2 | Optimal parameters for segmenting the targets of the lung phantom. The $\lambda_{1,2,3}$ array is shown such that λ^+, λ^- are represented in the columns with i shown along the rows | 117 |
| 4-3 | Registration error metrics for the three registration algorithms. 1) The mean error comparing the vector field of the method to the reference vector field, 2) The maximum error of the vector field comparison, 3) The mean bifurcation landmark error and 4) the mean vector field error evaluated only at those landmark coordinates. The uncertainties stated here are the 95% confidence intervals calculated | |
| | using Equation 4.11 | 121 |

LIST OF FIGURES

| LIST OF TROUBLES | |
|---|--|
| | page |
| A visual example of the ground truths needed for registration and segmentation. In a) Two squares represent an object imaged at two different times and has undergone rotation. Our ground truth is represented by the vectors that describe the movement at any point in the first image. Shown in b) and c) is an example for segmentation, where our ground truth is represented by a curve (in 2D) or surface (in 3D) that accurately defines the boundary of the object in question. In this case the dark grey square which exists over a lighter grey background is the object we wish to segment. The boundary shown in red in c) is our ground truth or what we will compare against | 7 |
| Hypothetical cell survival curves for late and early responding cell types reproduced from Podgorsak, 2005 [1] | 11 |
| Coronal view of an image acquired with a PET scan on left and fused PET/CT on the right of a subject with lesions throughout the lymphatic system. Elevated ¹⁸ F uptake is seen in the liver and bladder due to elimination of the tracer by the body. (L. Vaalavirta / CC-BY-SA-2.0)[2] | 18 |
| Sagital view of the head and neck of a patient deemed 'normal' using a T1-weighted scan. (Relgh LeBlanc / CC-BY-SA-2.0) | 19 |
| CBCT (a) versus conventional CT (b) scan of a pair of preserved swine lungs demonstrating the differences in contrast and noise | 21 |
| Application of the snakes segmentation approach applied to an octagon and a circle. Image a) shows us the algorithm after the 1st iteration after being initialized through a manual selection of points. In b) we see the algorithm after 30 iterations. It is unable to split the shape without implementing a special procedure and encompasses both test shapes | 25 |
| | A visual example of the ground truths needed for registration and segmentation. In a) Two squares represent an object imaged at two different times and has undergone rotation. Our ground truth is represented by the vectors that describe the movement at any point in the first image. Shown in b) and c) is an example for segmentation, where our ground truth is represented by a curve (in 2D) or surface (in 3D) that accurately defines the boundary of the object in question. In this case the dark grey square which exists over a lighter grey background is the object we wish to segment. The boundary shown in red in c) is our ground truth or what we will compare against. Hypothetical cell survival curves for late and early responding cell types reproduced from Podgorsak, 2005 [1] Coronal view of an image acquired with a PET scan on left and fused PET/CT on the right of a subject with lesions throughout the lymphatic system. Elevated ¹⁸ F uptake is seen in the liver and bladder due to elimination of the tracer by the body. (L. Vaalavirta / CC-BY-SA-2.0)[2] Sagital view of the head and neck of a patient deemed 'normal' using a T1-weighted scan. (Relgh LeBlanc / CC-BY-SA-2.0) CBCT (a) versus conventional CT (b) scan of a pair of preserved swine lungs demonstrating the differences in contrast and noise. Application of the snakes segmentation approach applied to an octagon and a circle. Image a) shows us the algorithm after the 1st iteration after being initialized through a manual selection of points. In b) we see the algorithm after 30 iterations. It is unable to split the shape without implementing a special procedure and |

| 2-6 | Visual representation of a level set surface intercepting a test image containing an octagon. The contour is defined by this intercept | 25 |
|-----|---|----|
| 2-7 | An example of the Chan Vese level set algorithm segmenting the same example from Figure 2–5. The procedure is shown after a) 1 iteration, b) 10 iterations and c) 25 iterations where the contour has split into two | 29 |
| 2-8 | Example of the use of a Gaussian Parzen window to estimate an intensity distribution. Part a) shows the population distribution, b) three values sampled from the distribution along with their surrounding Parzen windows. In c) we see the addition of the Parzen windows of all three samples compared to the original distribution, this is further refined with more samples in d)-f) | 42 |
| 2-9 | A Venn diagram explanation of mutual information, represented as the overlap symbolizing the redundant information described by two populations or in our context intensity values taken from two images or image regions. Each circle represents the entropy/image information from each of these populations. The joint entropy is effectively the union of these two circles/entropies | 44 |
| 3-1 | Mesh plots of the JRD energy space using Bernoulli distributions for P_1 and P_2 . In this context $P_k = (p_k, 1 - p_k)$ replaces $P(J(x_i), \Omega)$ in equations 3.4 and 3.8. In a) alpha is chosen equal to 1 with equal weights. b) shows the function with $\alpha = 5$ and equal weights. c) shows the function with $\alpha = 5$, $w_1 = 0.75$ and $w_2 = 0.25$. The segmentation algorithm would maximize the JRD, these are the spots in the energy space where there is the largest difference between P_1 and P_2 if the weighting values are equal. Changing the weighting parameters affects where these maxima occur | 57 |
| 3-2 | The inner jar wrapped in the bolus sheet (left) and the two containers, one inside the other (right) | 61 |
| 3–3 | Transverse slices of phantom PET scan for scan times of 4, 6, 9, 15, 62, and 246 seconds (from left to right in the top row). Slices of the phantom taken with the CBCT are shown in the bottom row with increasing SNR from left to right | 62 |

| 3-4 | Inhomogeneity correction with a) the original CBCT slice (from scan #6). b) The ideal phantom whose values are equal to the mean within the 4 regions found in a). c) The ratio of b) to a) following a bilateral filter smoothing, using $\sigma_1 = 13$, $\sigma_2 = 18$ and a tolerance of 0.02, and finally d) the corrected image | 65 |
|------|---|----|
| 3–5 | JRD and mutual information measured for circles of growing radius centered at the inner jar using the CBCT images. The low SNR scan had an SNR value of 32 and the high SNR scan had a value of 36. The peak is clearly preserved using the JRD when applied to the lower SNR image set | 69 |
| 3–6 | JRD and mutual information measured for circles of growing radius centered at the inner jar using the PET images. The low SNR scan had an SNR value of 9.2 and the high SNR scan had a value of 26. | 70 |
| 3–7 | The Jensen Rényi divergence measured for the PET scan of the noise phantom with circles of increasing radii. The profiles are shown with varying choices of parameter α . When α is equal to 1, the values become negative since the Rényi entropy reduces to the Shannon entropy as shown in equation 3.8 | 71 |
| 3–8 | The average concordance index of the active contour based on mutual information and the Jensen Rényi divergence for varying CBCT SNR values. The JRD shows a linear response to noise whereas the mutual information shows a somewhat exponential decrease in performance | 72 |
| 3–9 | The average concordance index of the active contour based on mutual information and the Jensern Rényi divergence for varying PET SNR values, controlled by the scan time | 73 |
| 3–10 | The average concordance index of the JRD based active contour compared to 9 other PET segmentation algorithms evaluated using the same data from Zaidi et al. [3]. Using only the PET intensity, the JRD based segmentation had an average CI of 0.55 versus 0.59 for the ECM-SW. The error bars represent one standard deviation | 74 |

| 3–11 | The average classification error of the JRD based active contour compared to 9 other PET segmentation algorithms evaluated using the same data from Zaidi et al. [3]. The JRD based segmentation had an average CE of 65% versus 50% for the FCM-SW. The error bars represent one standard deviation | 75 |
|------|--|-----|
| 3-12 | The estimation error for the JRD based segmentation method of the GTV compared to the macroscopically determined maximum diameter. The average error was 63%, 19.5% and 14.8% for the segmentations using CT only, PET only and PET/CT. Particularly, high errors for cases 4 and 21 were seen when using CT alone due to the small size of the lesions and their proximity to the chest wall causing contour leakage | 77 |
| 3-13 | The correlation of the JRD estimated maximum diameters versus the macroscopically determined maximum GTV diameters using only the PET image. The solid line shows the linear fit to the data while the dotted line represents the ideal 1 to 1 linear relationship. The JRD based method shows a higher correlation compared to the SBR technique with an R ² value of 0.85 versus 0.82 | 78 |
| 3–14 | The correlation of the JRD estimated maximum diameters versus the macroscopically determined maximum GTV diameters using both the PET and CT. The incorporation of both modalities shows an improved correlation versus using PET alone | 79 |
| 3–15 | A comparison of the JRD method applied to the Louvain (a and b) and MAASTRO (c and d) datasets with their respective references. In a and b, the JRD method is shown in blue compared to the macroscopically determined contour in green. For c and d, the JRD method using the CT only is drawn in magenta, using PET only in green and using combined PET and CT together in blue. It is compared to the maximum diameter shown with the yellow arrow. | 80 |
| 4–1 | The computer controlled airflow system model shown from the a)side, b)top, c)front and d)photographed connected to the swine lungs. The main piston has a 4 cm range of motion and is held horizontal by a pair of pillow block bearings attached to a mounting plate | 100 |

| 4–2 | Transverse views of the synthetic targets scanned with CT (a)-c)), MRI (d)-f)) and PET (g)-i)). The targets 1-3 are organized from left to right. Target 1 consists of compartments 1.2, 13.9 and 20.2 cm ³ in volume from the inside to the outside. Target 2 is made up of compartments with volumes of 0.85 and 21.9 cm ³ . Likewise, target 3 has compartments of 10.8 and 13.9 cm ³ in volume. Maximal diameters for each compartment are shown in white. Image scaling for each target may not match | 103 |
|-----|--|-----|
| 4–3 | The compartment obfuscating procedure with a) the original image, b) the image after the compartment has been replaced with NaN values, c) the image following inpainting and smoothing and d) the original image smoothed using the same filter. e)-h) show a range of contrast values by varying λ in Equation 4.2 from 0.9 to 1.05 in 0.05 increments. These same values were used to evaluate the three segmentation methods shown in Figure 4–9. A horizontal profile of the synthetic tumor taken from e)-h) is shown below in i)-l) | 104 |
| 4-4 | The bifurcation tracking pipeline. This consisted of an initial region growing of the air in the lungs, followed by morphological hole filling and subtraction from the original mask to segment the lung airways. A 3D skeletonization procedure determines the medial axis of the airways which are then compared against a bank of automatically generated 3D templates to detect bifurcations. The detected bifurcations from two lung volumes are then matched using the estimated diameter of the bronchi and an initial rigid alignment using cluster centers | 107 |
| 4–5 | Graphical User Interface written for quality control of matched bifurcation points. Red croses show the point pair selected by the iterative point matching algorithm. Green crosses represent detected bifurcations in each volume. The GUI shows a CT scan of the lungs from three planes, transverse, coronal and sagittal (ordered left to right) | 109 |
| 4–6 | Bifurcation tracking error as a function of deformation magnitude for human and phantom lungs | 115 |

| 4-7 | The three profiles tested using the computer controlled respirator. The measured breathing trace using the respiratory bellows belt is shown in blue with the feedback from the optical encoder showing the piston position is plotted in red |
|------|---|
| 4-8 | A summary of the segmentation results for the three algorithms (Chan-Vese, Hybrid and MVLS) using three synthetic lesions for a) CBCT, b) CT, c) MRI and d) PET |
| 4-9 | The Dice coefficient of the three segmentation methods evaluated using the lungs for varying CNR values of the active compartments of synthetic lesion 1 |
| 4–10 | Error maps using the vector field differences of the original Demons algorithm with b) The fast Symmetric Forces registration b)Diffeomorphic demons and c)MiMVista's deformable registration algorithm. The side bar represents the error in voxel widths. The red crosses mark detected bifurcation points within the current slice and adjoining 3 slices |
| 5-1 | An outline of the algorithm highlighting the adaptive mesh generation using a 3D Floyd-Steinberg dithering filter and the iso2mesh package for mesh creation. The level set segmentation function is updated by calculating the gradient of the JR divergence with respect to raising or lowering the level set function. The iterative update to the deformation vectors is calculated from the regular registration gradient and a coupling term which applies deformation vectors in order to better align the image in the local region surrounding the segmentation target |
| 5–2 | Adaptive meshing pipeline beginning with uing the eigenvalue of the Hessian matrix to exemplify image features. The Floyd-Steinberg dithering filter is used to determine the locaton of points which after randomly selecting can be used to produce a 3D mesh 137 |
| 5–3 | Photo of the computer controlled respirator connected to the preserved swine lungs. A 186 watt motor is used to manipulate the rubber bellows at the end, inflating and deflating the lungs. 141 |

| 5–4 | Photo of the synthetic tumor consisting of multiple vacuum sealed compartments | 142 |
|------|---|-----|
| 5–5 | The bifurcation pipeline used to provide a ground truth for registration evaluation | 143 |
| 5–6 | Examples of the addition of artificial noise to the CT volumes for varying SNR values | 146 |
| 5–7 | Tuning of the α parameter with regard to use with CT. Overall target registration was minimized with a value of 0.7. Error bars represent the 95% confidence interval | 147 |
| 5–8 | Tuning of α_2 the seperate α value applied solely to the segmentation step of the regmentation process. Error bars represent the standard deviation across 10 trials for each data point | 148 |
| 5–9 | Example of the registration performed on the lungs at two adjacent phases of breathing. Shown is a)the reference image, b) the deformed reference image and c)the deformed image along with the registrations vectors in proximity to that slice. Also shown is d) the difference image between the reference and target images before registration and e) following registration | 149 |
| 5–10 | Dependancy of target registration error (TRE) on the coupling parameter within the local region of the targets being segmented and for overall lung region | 150 |
| 5–11 | Dependency of the DSC on the coupling term C for the three targets within the biomechanical phantom | 151 |
| 5–12 | Dependency of the JR regmentation method compared to the Demons algorithm and Lucas-Kinade optical flow method for various SNR values | 152 |
| 6–1 | T1-weighted 3D FFE scans of the jar phantom with SNR values of 11.6,14.3,18.,21.7,25.7 and 28.3 dB | 165 |

CHAPTER 1 Introduction

1.1 Author Contributions

I would like to thank all my co-authors for their contributions to this work and would like to specify their contributions here.

Dr. Issam El Naqa: Contributed through general guidance, supervision and acquisition of funding. Dr. El Naqa first suggested investigating the use of the Jensen Rényi divergence and contributed example code detailing the use of a 2D the level-set algorithm in addition to interpolation and filtering using the adaptive meshing scheme presented in Chapter 5. He also assisted in acquiring data using the CT simulator in addition to data sets from outside sources. Dr. El Naqa also edited all documents present in this thesis.

Dr. Habib Zaidi: Dr. Zaidi was kind enough to contribute the Louvain data set presented in Chapter 3 along with performance data of comparable algorithms. This was critical for evaluating the Jensen Rényi segmentation algorithm. Dr. Zaidi also contributed through review and editing of the work presented in Chapter 3.

Dr. Ives Levesque: Dr. Levesque contributed significantly by offering guidance in developing the synthetic tumors presented in Chapters 4 and 5. Dr. Levesque was also responsible for training in the use of the MRI scanner and developing a protocol for scanning the lung phantom. Dr. Levesque has also contributed through editing of this thesis.

Pierre L éger: Mr. Léger was responsible for designing and constructing the control circuit used to operate the airflow system of the biomechanical lung phantom presented in Chapter 4.

Joe Larkin: Mr. Larkin contributed significantly through education on the use of the machine shop and physical construction of the airflow system presented in Chapters 4 and 5.

1.2 Motivation

Cancer accounts for 1 in 7 deaths worldwide, approximately 8.2 million in 2012. Lifestyle choices are expected to add to this number with smoking as the number one contributor. In low to middle-income countries the number of tobacco related deaths are projected to double by 2030 (as compared to 2002 statistics)[4]. The treatment of lung cancer is and will continue to be a significant challenge in healthcare.

The choice of treatment in 60-70% of cancer diagnoses includes radiation therapy for curative or palliative intent[5]. This is accomplished through the delivery of radiation dose to a pre-defined target while minimizing the collateral dose to healthy tissue. This is usually achieved with the use of a linear accelerator or radiation source that will emit photons and/or electrons in order to apply a dose of radiation to a specific tissue region in the body. This treatment is often divided into many sessions over the course of weeks due to the radiobiological response, called fractions. Changes in tumour volume of nearly 2%[6] per day by volume has been observed throughout courses of treatment. As such, efficacy is largely dependent on knowledge of the extent of the biologically active tumour region and the ability to account for these changes through adaptive strategies that tailor treatment to each patient's

progression. Unfortunately, such a course of action often puts a strain on clinical resources due to re-planning time of the treatment and equipment requirements, increasing costs by as much as 40%[7] and compromising its practicality.

With more complex treatment regimens becoming the norm, this considerable burden has motivated commercial software vendors to include automated planning tools to assist with planning processes such as segmentation and registration. Segmentation within the context of radiation therapy is the act of partitioning biologically relevant regions within a medical image such as active tumours or critical organs. Manual segmentation is a time consuming and laborious process prone to subjectivity and a large degree of variability. The degree of interobserver variability has been determined to be one of the largest sources of uncertainty in regards to knowledge of the boundary of the tumor in radiotherapy [8] reaching up to 700% by volume when using Computed Tomography (CT) information [9].

Registration on the other hand involves warping or transforming one set of images so that they align with a second set taken at a different time or with another scanner. These image processing tools allow planners not only the ability to account for anatomical changes, but also to leverage additional imaging information from modalities such as Positron Emission Tomography (PET) and Magnetic Resonance Imaging (MRI) in addition to conventional CT. This can be used to increase knowledge of the anatomy during planning, ultimately leading to improved survival and reduced risk of toxicity and secondary cancers. An example of this is with the incorporation of hybrid PET/CT scanners into the treatment planning process. Future necessity for these tools is further highlighted by the recent emergence of

hybrid MRI-linear accelerators which are able to deliver a prescribed radiation dose while imaging the treatment site simultaneously. Such a treatment strategy relies heavily on fast and accurate registration of CT and MRI information assuming that treatment planning was performed using the CT.

Automated methods have potential to reduce uncertainty and treatment planning time, ultimately saving costs and making adaptive radiotherapy increasingly feasible for a larger number of patients.

The difficulty in using automated registration and segmentation tools is the potential for compromised performance under changing image variables such as contrast, image noise and artifacts. Such conditions are common when dealing with on-board imagers such as Cone-Beam CT (CBCT) and Mega-Voltage CT (MVCT) or with PET imaging. These are areas where human input and interpretation contributes the largest value but again is susceptible to observer subjectivity.

The processes of registration and segmentation as applied in this thesis are framed as optimization problems using a chosen cost function. The cost function is used in this context to determine when the segmentation algorithm has reached the visual border of an object as seen on an image, or in the case of registration, when the two images have been accurately aligned with one another. As a cost function the Jensen Rényi divergence has the potential to partially alleviate concerns when poor contrast and image noise conditions are present. The divergence measure relies on a parameter α to determine its curvature and thus how the algorithms reliant on it will behave. In addition to investigating the usage of the Jensen Rényi divergence, simultaneous coupling of the segmentation and registration processes can

further improve efficiency and accuracy for both methods by introducing additional information into the processes of each.

1.3 Challenges

Our work addresses several difficulties faced when using the Jensen Rényi divergence in general and simultaneous registration and segmentation algorithms in particular.

One of the difficulties faced in incorporating the Jensen Rényi divergence is optimization of its α parameter in application to a specific imaging context. The α parameter determines the curvature of the cost function and significantly influences the performance of the registration and segmentation processes. We have taken an experimental approach to optimization of the α parameter, giving recommended values for the different imaging modalities studied. Additionally, as with the α parameter, the degree of coupling neccessary between the registration and segmentation terms was unknown and required its own optimization as well.

The second challenge faced was finding a suitable dataset for evaluating the algorithm. Since the joint registration/segmentation algorithm represents an uncommon approach, most datasets available lacked the ability to evaluate both registration and segmentation. Added to this, the fact that our algorithm has the built in flexibility to tackle multiple modalities requires compatibility of the dataset/phantom to MRI and/or PET. Anatomical and kinetic realism was another important factor in order to reproduce the image detail, texture and deformation field seen on clinical scans rather than resorting to homogenous regions and simplistic movement patterns. To this end we constructed our own phantom using preserved tissue. In order to evaluate

segmentation and registration algorithms, we need data to compare against in which we have a reasonable degree of certainty of its validity. This data will constitute our ground truth. This invites further difficulties as we required a segmentation and registration ground truth beyond manually selecting a series of points and boundaries which by the very nature of how they are acquired contain significant uncertainties.

Creating a segmentation ground truth required a target that was MRI/PET/CT compatible, contained a degree of heterogeneity in appearance and could be obfuscated. This requires 'hiding' the target boundary using a second compartment and varying the contrast of the target compartment in order to increase the difficulty of segmentation. In this way we can evaluate performance differences between mutliple segmentation algorithms. When considering PET imaging, user safety becomes a concern since contact with the radiotracer can lead to contamination and uneccessary dose.

Extracting a registration ground truth is a challenge within the image processing field. The use of fiducial markers (artificial objects placed into the object being scanned acting as landmarks) could be utilized for this purpose, but would potentially bias the registration since they alter the intensity information in the image used by the registration algorithms. Artificial digital deformations can be used but ensuring anatomical correctness then becomes a challenge.

New tools are required to address the aforementioned concerns and perform simultaneous registration and segmentation evaluation while avoiding the pitfalls to commonly existing techniques.

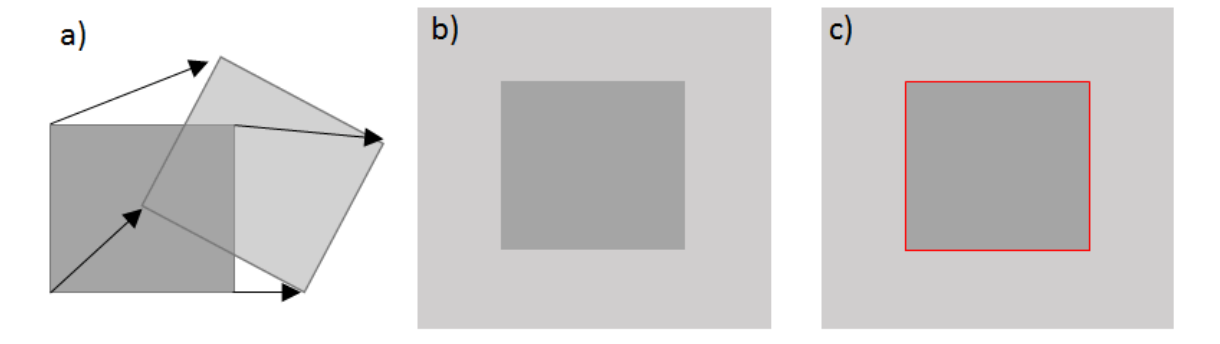


Figure 1–1: A visual example of the ground truths needed for registration and segmentation. In a) Two squares represent an object imaged at two different times and has undergone rotation. Our ground truth is represented by the vectors that describe the movement at any point in the first image. Shown in b) and c) is an example for segmentation, where our ground truth is represented by a curve (in 2D) or surface (in 3D) that accurately defines the boundary of the object in question. In this case the dark grey square which exists over a lighter grey background is the object we wish to segment. The boundary shown in red in c) is our ground truth or what we will compare against.

1.4 Contributions

The work described in this thesis contributes to the fields of radiotherapy and image processing in three ways.

First, we developed a novel segmentation algorithm by investigating the use of the Jensen Rényi divergence applied to a level-sets methodology. We reported a performance on par with current state of the art algorithms for the task of PET segmentation and demonstrated multimodal applications using PET/CT. We describe the Jensen Rényi segmentation algorithm in Chapter 3.

Second we developed a quality assurance (QA) platform for evaluating joint segmentation/registration algorithms that is MRI/PET/CT compatible, and is physically and kinetically realistic from an anatomical standpoint. Part of the platform is a computer controlled respirator that can fully replicate human breathing traces, a feature useful for evaluating motion prediction algorithms and for testing registration under realistic conditions. Details on the phantom are included in Chapter 4.

Finally, we combined the segmentation algorithm previously developed with a non-rigid registration technique to see if simultaneous application could improve convergence and accuracy for both methods. We optimized the α and coupling coefficients through experiments. The simultaneous algorithm is described in Chapter 5.

CHAPTER 2

Background: Information Theory, Segmentation and Registration

In this section we describe the background theory on radiation therapy, segmentation, registration and divergence measures that will be neccessary to understand the rest of the chapters. An overview of the practice of adaptive external beam radiotherapy will be given to contextualize the image processing algorithms and their role. The segmentation and registration algorithms in turn are each dependent on an objective function which they seek to maximize through optimization. The underlying innovation is the exploration of the Jensen Rényi divergence as a cost function and as such, this chapter will conclude with a review of information theory in Section 2.4.

2.1 External Beam Radiation Therapy

As stated in the motivation section, radiation therapy is a popular choice in the treatment of cancer, particularly in cases where surgical resection is deemed too risky, prior to surgery in order to reduce the disease burden or simply in conjunction following surgery in order to improve survival. External beam radiotherapy involves the application of radiation from outside the body either using a natural source such as Cobalt-60 or an electronic one such as with the use of a medical linear accelerator. The accelerators can usually produce both electrons (in the kinetic energy range of 4-25 MeV) and photons (in the energy range of 4-25 MV). Photon irradiation can cause cell death or eliminate the ability of cells to reproduce through two approaches,

namely direct or indirect ionization. The first involves the interaction of radiation directly with the DNA or critical structures of the cell causing ionization in molecules that lead to a loss of function, or irreversible damage to genetic material through the breaking of DNA bonds. This may happen through several mechanisms. For photons they occur primarily through photoelectric effect, compton scattering and photonuclear interactions. This leads to photon and electron scattering and positron production which go on to further deposit energy in the surrounding medium. Rather than direct ionization of critical structures in the cell, additional damage is applied indirectly through the production of free radicals such as hyodroxyl (OH⁻) through the ionization of water particles. These go on to interact chemically which can lead to further DNA bond breaking. One way of measuring radiation dose is in units of Gy, equivalent to the deposition of one J/kg of material.

2.1.1 Fractionation

The effect of radiation on cell populations is complex and depends on a number of factors such as sensitivity, the presence of radiosensitizers and radioprotectors and the ability of the cell to repair damage. The main goal of radiotherapy and radiotherapy planning is to maximize the dose delivered to diseased areas of the body while minimizing the dose received by healthy regions. This leads to a maximization of what is termed the tumor control probability (TCP) and minimization of the normal tissue complication probability (NTCP). The ratio of TCP to NTCP is called the therapeutic ratio and is an indicator of a treatment plan's quality. In order to take advantage of the ways in which cells respond to radiation and maximize the therapeutic ratio, dose is not delivered in one treatment session but usually divided

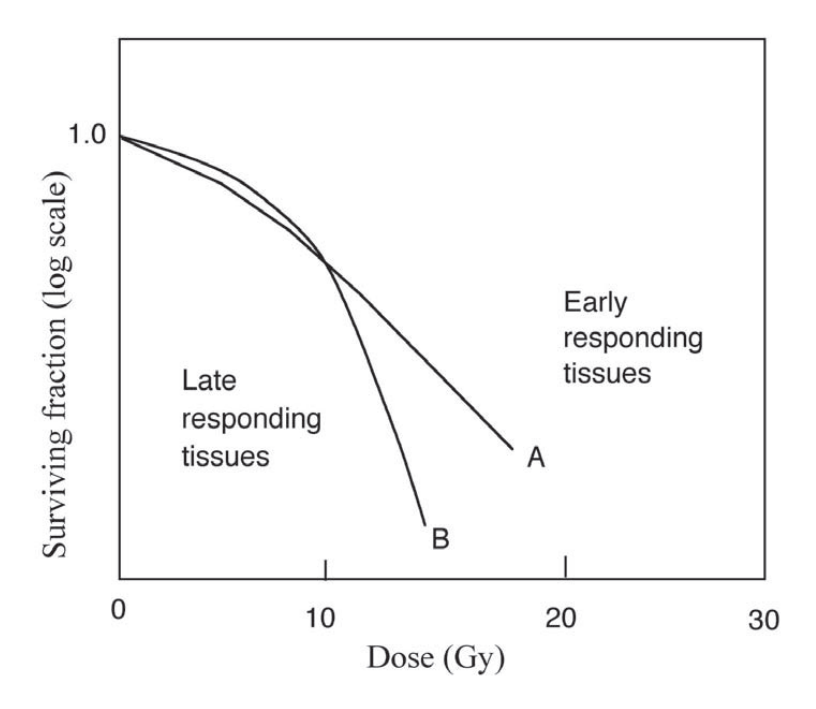


Figure 2–1: Hypothetical cell survival curves for late and early responding cell types reproduced from Podgorsak, 2005 [1]

into 1-2 Gy fractions. Total treatments are delivered over many fractions over a few weeks. The rationale for and proper application of fractionated radiotheray are summarized by the 5 R's of radiobiology (previously the 4 R's, so we see some progress in this area).

Repair: By fractionating treatment, normal tissue is given the chance to repair while malignant cancer cells often have suppressed repair pathways hindering their ability to recover from sublethal damage. The application of this idea is a bit more nuanced in that the proximity and type of tissue around the target area or in the radiation beams pathway must be considered.

Sublethal damage can be repaired during the treatment itself and thus tissue generally exhibit one of two types of behaviour, late or early responding which is of course relative to other tissues. Late responding tissues react early to repair damage from radiation but once those repair mechanisms are overwhelmed, cell death occurs at a greater rate than early responding tissue. This is illustrated in Figure 2–1. This is the main idea behind fractionation schemes. If the target region responds later than adjacent healthy tissue than higher doses per fraction are needed to seperate the cell survival curves of the two tissue types and fewer fractions are needed. Likewise if the target regions respond earlier, smaller doses spread over a larger number of fractions becomes more appropriate.

Redistribution: Cell sensitivity to radiation is dependent on the stage of the cell cycle that it is found in when irradiated. The G2 and M phases of the cell cycle are the most sensitive while the S-phase is found to be the most radioresistant. Because of this there is a differential in cell survival based on the distribution of phases that cells are found in. Fractionating radiotherapy allows the cell population to redistribute so that those in the S phase during the first fraction have a chance to change to the G2 or M phase in future fractions.

Reoxygenation: One of the chemical species that radiosensitizes cells to radiation is oxygen. Due to large demands on energy and oxygen that tumors have, they tend to grow quickly and signal the growth of new blood vessels in highly irregular patterns. This inefficient distribution of resources leads to hypoxic areas, with oxygen rich regions tending to exist at the edges of a tumor. Higher radiosensitization in these areas leads to a higher cell kill and thus reduced competition for oxygen,

allowing areas deeper in the tumor to re-oxygenate following a dose of radiation. This allows them to be more susceptible to treatment in the following fraction. A pattern that would not be observed with a single application.

Repopulation: Repopulation of cells in the body plays a large role in treatment outcome. It is found that cancer cells can undergo rapid repopulation following radiation treatment. Thus continued and frequent fractions of radiation are necessary to manage the disease.

Radiosensitivity: Different cell types and tumor types have intrinsicly different sensitivities to radiation which must be taken into account when considering treatment options and techniques. For example activation of Epidermal Growth Factor (EGFR)[10], the p53 protein [11] and presence of the Human Papilloma Virus (HPV)[12] have been identified as sources of radiosensitivity or radioresistance.

The need for fractionation presents a significant problem when considering the need to ensure consistent geometric accuracy throughout treatment. Patient anatomy along with tumor dimensions have the very real possibility of changing throughout the course of treatment which typically stretches over a few weeks and even during treatment itself due to patient movement.

2.1.2 Planning

Treatment planning for external beam radiotherapy involves several steps following initial diagnosis and prescription of a treatment option. The first step in planning involves a CT simulation in conjunction with immobilization of the patient. A CT simulation differs from a diagnotic CT scan in terms of quality, a larger bore size (to allow a larger array of patients and immobilization equipment) and the use of

a robotic flat-top couch similar to that installed in the linear accelerator treatment bunker in order to replicate the conditions under which the patient will be treated. Careful attention is made to immobilize the patient using a combination of devices such as deflatable polyurethane foam molds, vacuum molded plastic masks for the head, bite blocks and skin tattoos to precisely reposition the patient in the same pose the day of the treatment. The CT simulation is used to give planners information on the attenuation properties of the patient. This scan is imported into a sophisticated treatment planning system (TPS) where the 3D anatomy of the patient is used to simulate the deposition of dose under varying beam configurations. The planners must then define the boundaries of tissues in the vicinity of the treatment site that they seek to spare, called organs at risk (OARs). Both the OARs and the boundaries of the tumor must be defined in a process called segmentation. This is typically done manually however more recently semi-automated and fully automated methods have made their way into the clinic [13, 14]. Several contours are defined for the tumor, the first is the gross tumor volume (GTV) which encompasses the gross tumor that is visible on the scan. A margin of a few mm is defined around the GTV to include the sub-clinical extent of the disease that is not visible on the scan, the boundary is referred to as the clinical target volume (CTV). An additional margin is defined around this to encompass the positional uncertainty of the target (ie. the full extent of motion during or between fractions that is expected to occur) called the internal target volume (ITV). Finally, one last margin is added to account for setup uncertainties on the day of treatment called the planning target volume (PTV) in which the planners attempt to ensure a uniform dose. Once the regions of interest have been defined, the number of beams, beam geometry and energy are determined in order to conform the dose to the PTV while attempting to spare the OARs as much as possible. This may consist of a set of static beams conformed to the shape of the target volume or more sophisticated approaches such as intensity modulated radiation therapy (IMRT) or volumetric arc therapy (VMAT). IMRT makes use of a large number of beams with sophisticated geometries that are planned on a grid using a multi-leaf collimator (MLC) to shape and vary the fluence from the beam's eye view which when added together over all angles, produce a dose distribution that conforms to the target geometry. VMAT incorporates one fluid motion of the linear accelerator and MLC around the patient rather than stopping for each beam position. The beam parameters of the chosen treatment type are optimized using multiple criteria based on the dose received by the PTV and surround OARs. Based on the weighting given to each criteria a plan that satisfies each of them (or comes as close as possible) is presented to the planner and can be accepted or rejected in order to change the chosen criteria and receive an improved plan.

2.1.3 Imaging

Treatment planning and diagnosis is heavily reliant on medical imaging available in the clinic and while radiotherapy is primarily concerned with CT, CBCT and MVCT other imaging modalities can also be incorporated in the cancer treatment.

CT

Computed tomography was first conceived by Sir Godfrey Hounsfield in 1967 while working for EMI [15]. Computed tomography works by using a fan beam of kilovoltage x-rays that pass through a subject and are measured by an opposing row

of detectors. Using the attenuation of the beam by subject and rotating the beam and detector around the subject, a 2D image can be reconstructed using a number of techniques such as filtered back projection of the data. Modern CT scanners use multiple rows of detectors in order to acquire hundreds of slices at once [16] which is particularly useful for 4D imaging of the lungs and heart. As CT makes use of kilovoltage X-rays, the primary mode of photon interaction is through the photoelectric effect. Thus image contrast in CT is strongly dependent on electron density.

CT provides higher soft-tissue contrast compared to X-ray radiographs in addition to 4D data when multiple volumes are acquired in series and sub-millimeter spatial resolutions. The values recorded in a CT image are called Hounsfield units (HU) and are defined in Equation 2.1.

$$HU = 1000 \times \frac{\mu - \mu_{water}}{\mu_{water} - \mu_{air}} \tag{2.1}$$

The Hounsfield unit normalizes the values of the image to the attenuation coefficient of water.

PET

Positron emission tomography is a functional imaging modality used to image the distribution of radiopharmaceuticals injected into a subject. The most commonly used radioisotope in the clinic is Fluorodeoxyglucose (¹⁸F-FDG) which has a radioactive isotope of fluorine attached to a glucose molecule in place of a hydroxyl group. This works as a glucose surrogate for imaging regions of the body with increased metabolism and glucose uptake such as the brain, heart and tumor lesions. ¹⁸F is

a convenient isotope as it has a decay time of 109.8 min, long enough for practical use but not too long that it will remain radioactive longer than needed. ¹⁸F decays through beta-plus emission where an emitted positron travels on the order of a few millimeters before anihilating with an electron. This interaction results in the emission of two gamma-rays at 180°. A ring of detectors is used to detect the gamma rays within a time window on the order of 10 ns. By recording these coincidences, activity is recorded as having occurred along the line connecting the location of the two detectors. In this way a singeram can be constructed similar to how CT reconstruction is performed. However due the activity statistics and effects such as misregistration of anihilation events, false detections and non-colinearity due to residual kinetic energy during anihilation, special reconstruction techniques are required. The most common of which are the ordered subset expectation maximization (OSEM), 3D-row action maximum-likelihood (3D-RAMLA) and the maximum likelihood expectation maximization (MLEM) algorithms. These use statistical models of the detector and anihilation process that take into account positional uncertainties when iteratively reconstructing the images through forward and back projection steps. The low energy of emitted positrons from ¹⁸F-FDG is also ideal as it leads to a shorter path length before anihilation, reducing the geometric uncertainty of the original decay event. FDG-PET is a highly sensitive modality, able to detect clonogen densities as low as 10^5 cells/cm³ compared to 10^{5-6} cells/cm³ for MRI and CT[17]. Hybrid PET/CT scanners have provided immense clinical utility by offering physically registered images that combine functional and anitomical information. This has greatly aided in detection and segmentation of lesions and has also been used to predict

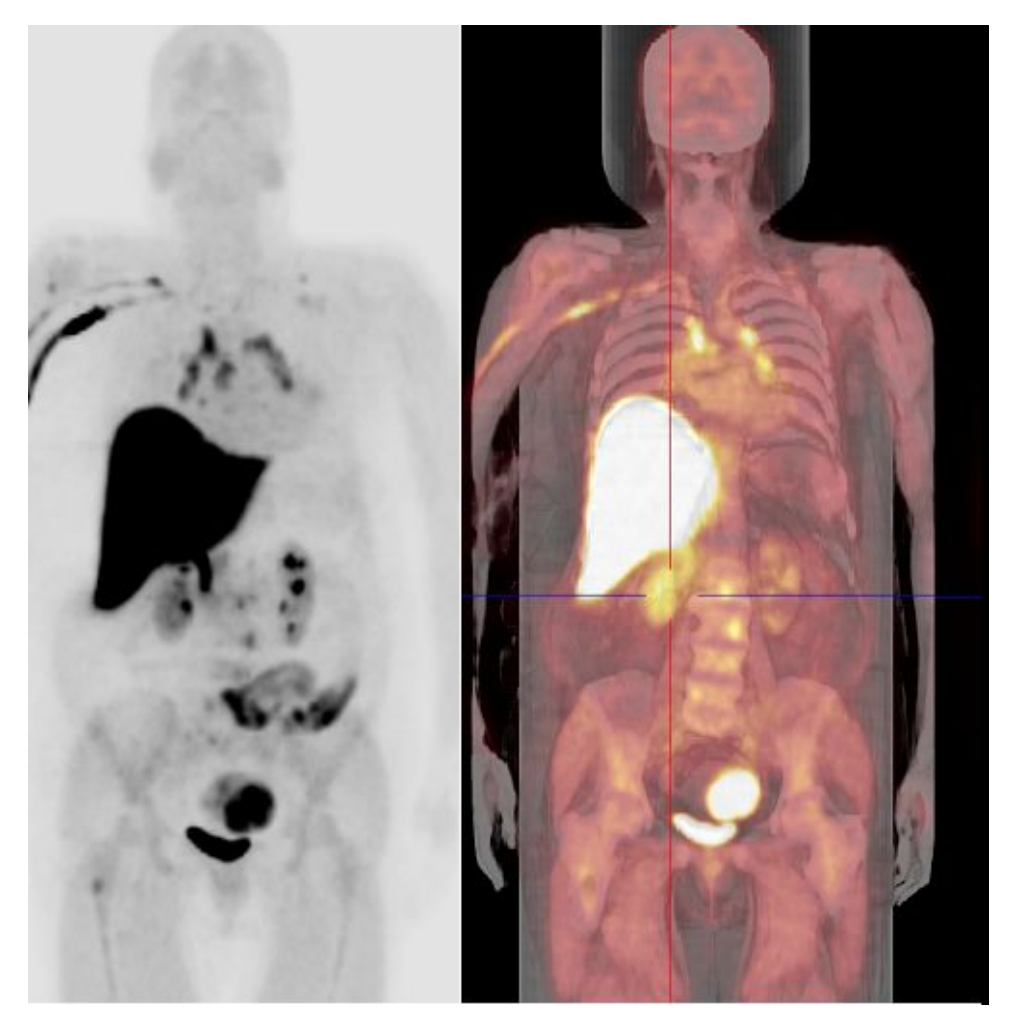


Figure 2–2: Coronal view of an image acquired with a PET scan on left and fused PET/CT on the right of a subject with lesions throughout the lymphatic system. Elevated ¹⁸F uptake is seen in the liver and bladder due to elimination of the tracer by the body. (L. Vaalavirta / CC-BY-SA-2.0)[2]

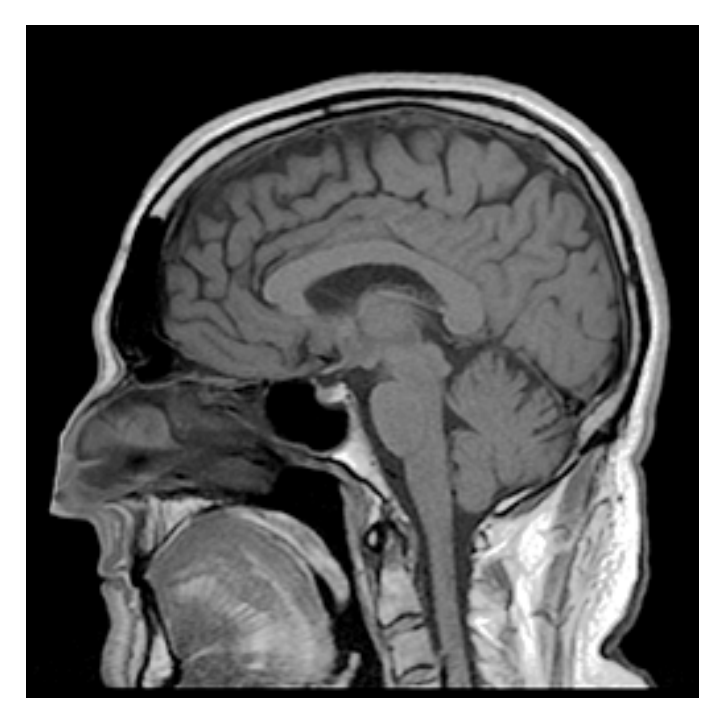


Figure 2–3: Sagital view of the head and neck of a patient deemed 'normal' using a T1-weighted scan. (Relgh LeBlanc / CC-BY-SA-2.0)

treatment response [18]. An example image is shown in Figure 2–2. One of the drawbacks to PET is the reduced spatial resolution (3-6 mm) compared to other modalities and increased noise that makes precise segmentation of objects difficult.

MRI

Magnetic resonance imaging is a profoundly varied and useful modality that can offer a wide variety of physical information and instrument flexibility for influencing image content. The operating principle of MRI is based on the application of high strength magnetic fields in the range of 0.23-9.4 T (clinical scanners do not tend to exceed 3 T). The main B-field is used to align the proton spins of molecules (signal is primarily dominated by water) while a secondary radiofrequency (RF) field is used

to precess these spins into the tangential plane. This RF field also aligns the phases of the spins. After cessation of the RF field, dephasing of the spins occurs due to influence of the microenvironment in addition to a return in spin orientation to the axis of the main B-field. The loss of RF signal and the increase in signal oriented in the main B-field direction are measurable properties directly linked to T2 and T1 weighted images [19]. Figure 2–3 shows an example image of the head and neck acquired using a T1-weighted scan. Spatial encoding is accomplished through the use of a linear gradient field applied in the same direction as the main B-field but varying in field strength over the x and y axes. This alters the precession frequency of the protons over space. When the fourier transform of the return signal is recorded, each frequency encodes a specific x and y location.

MRI is advantageous as a non-invasive, non-ionizing imaging technique that poses no adverse health effect when operated correctly. The disadvantages to using MRI include cost, scanning time, the preclusion of certain patients with ferric implants and difficulties imaging lung. Difficulties in imaging lung stem from blood flow, organ movement, molecular diffusion and the heterogenous structure of the lung parenchyma leading to fast signal loss. Contrast agents for use in MRI consist mainly of Gadolinium based molecules.

CBCT

Cone-beam computed tomography works on a similar principle as computed tomography except that it is designed as more accessible option with a smaller form factor allowing integration onto the linear accelerator itself. Cone-beam CT differs from conventional CT in that, as its name implies, it uses a cone shaped X-ray beam

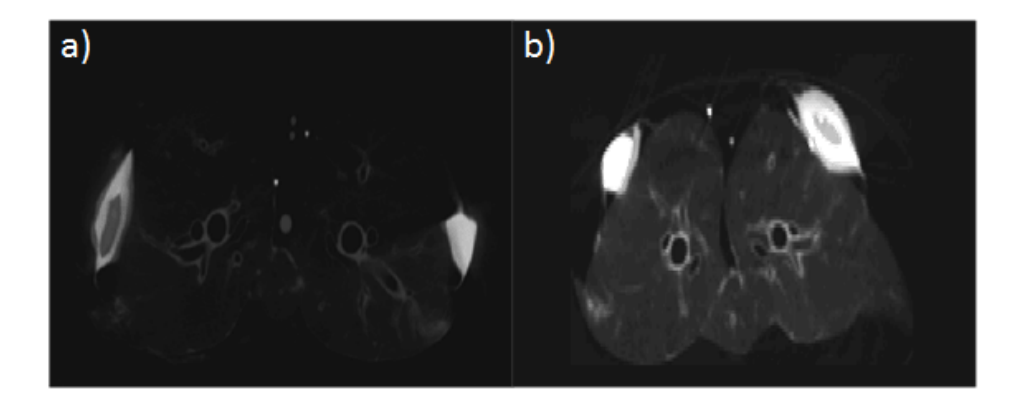


Figure 2–4: CBCT (a) versus conventional CT (b) scan of a pair of preserved swine lungs demonstrating the differences in contrast and noise.

opposite a flat panel detector. One single rotation over 200° is sufficient to acquire enough information to reconstruct a 3-dimensional volume. This is advantageous for ensuring proper alignment of the patient with the planning CT while they lie on the treatment couch. Due to the differing beam geometry, CBCT requires alter reconstruction methods.

One major drawback to using CBCT is reduced contrast and increased noise caused by scattering events resulting from the use of a cone beam as opposed to a fan-beam where many of these scattering events end up outside of the detector field of view. An example of this can be seen in Figure 2–4

2.1.4 Adaptive Strategies

Adaptive radiotherapy (ART) encompasses a number of techniques that account for anatomical changes over different time scales. Intrafractional adaptive therapy attempts to track tumor and OARs during involuntary movement such as swallowing or free breathing. While simpler methods such as breath holding during beam on time are possible, many patients due to poor physical condition are unable to comply. Gating is an approach where the free breathing of a patient is tracked using either an infrared reflective block or using a pressure sensitive respiratory belt strapped around the thorax followed by the treatment beam turning on during a specific breathing phase. These two procedures do of course require significantly longer treatment times. Dynamic tracking of the target using the MLC during free breathing is one alternative currently being researched but requires a method of imaging the tumor or an implanted seed. Specialized products such as the Synchrony Respiratory Tracking System along with the Cyberknife linac (Accuray, Inc., Sunnyvale, California) or the Calypso 4G localization system from Varian (Palo Alto, California) system often rely on implanted gold seeds tracked through stereo radiographic panels. A drawback to this method is the need for invasive insertion of the seed and risks the possibility of pneumothorax (leakage of air into the pleural cavity surrounding the lungs).

Interfractional adaptive radiotherapy applies to anatomical changes experienced over multiple fractions of treatment. This can incorporate modalities such as CBCT and MVCT or offline modalities such as PET, CT or MRI. Typically, compromises to the treatment planning objectives (usually quantified by TCP, NTCP and dose coverage to specific structures) are used as a selection criteria for re-planning in response to limited time and physician resources [20, 21]. Replanning in this context requires adapting patient contours to the current anatomical context. This can be done through image registration of the original planning scans to the current scans and deforming the previous set of contours. However, for regions where tissue deformation is insufficent to account for biological changes (primarily loss or

gain of tissue), alterations of the contours may necessitate re-segmentation through manual or computer assisted means. Reoptimization is then required to derive new beam parameters that will fulfill a new required dose distribution within the patient. Deformable registration also serves another purpose within ART to track and accumulate total dose in order to ensure overall dose objectives are met.

Considering their importance in the larger context of image-guided adaptive radiotherapy (IGART), the theory and knowledge of the approaches to both segmentation and registration are necessary for proper understanding of this work.

2.2 Image Segmentation

Haralick and Shapiro define segmentation as a "partition of an image into a set of non-overlapping regions whose union is the entire image" [22]. During treatment planning, this is often referred to as contouring. Image segmentation simply entails defining an object's boundaries using an enclosing curve (in 2D) or surface (in 3D) either manually or using software to assist. Segmentation is a significant challenge within the medical imaging and computer science field particularly when there is a lack of information separating the object from its background. This section will cover the two main approaches to variational methods of segmentation, explicit and implicit representations. Variational methods revolve around the initialization and evolution of a contour to satisfy a particular cost function.

2.2.1 Explicit Representation: Snakes

The snakes method of segmentation is where the contour in question is explicitly defined by a series of line segments connecting an array of points represented by C in Euclidean space. The arc length along C is defined by s. It was first proposed

in 1987 by Kass, Witkins, and Terzopoulous [23]. The proposed cost function is represented by Equation 2.2,

$$E(C(t)) = \int_0^1 \left(\alpha(s) \left| \frac{\partial C(s;t)}{\partial s} \right| + \beta(s) \left| \frac{\partial^2 C(s;t)}{\partial s^2} \right|^2 \right) ds + \gamma \int_0^1 P(C(s;t)) ds; \quad (2.2)$$

where the first integral refers to the internal energy that stems from the curvature of the contour. The first and second order terms within this integral correspond to the membrane and thin plate behaviour (or sensitivity to the degree of stretching and curvature) of the contour, regulated by the coefficients $\alpha(s)$ and $\beta(s)$. The second integral in Equation 2.2 refers to the potential energy which drives the evolution of a contour based on image information. It may take many forms but it is commonly a function of the image gradient.

Equation 2.2 can be solved using the following Euler-Lagrange partial differential equation (PDE),

$$\frac{\partial}{\partial s} \left(\alpha \frac{\partial C}{\partial s} \right) + \frac{\partial^2}{\partial s^2} \left(\beta \frac{\partial^2 C}{\partial s^2} \right) + \nabla P \left(C(s, t) \right) = 0 \tag{2.3}$$

One of the general drawbacks to using explicit representations of active contours is that they require additional attention in regulating point density as well as splitting/combining multiple regions. In particular, handling areas of high curvature such as object corners can be challenging. This can be seen in Figure 2–5 where the snakes algorithm is used to attempt to segment an octagon and a circle. In the next section we will see how an alternative representation can alleviate this challenge.

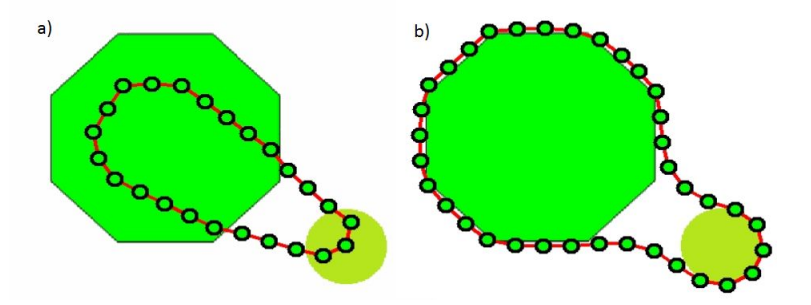


Figure 2–5: Application of the snakes segmentation approach applied to an octagon and a circle. Image a) shows us the algorithm after the 1st iteration after being initialized through a manual selection of points. In b) we see the algorithm after 30 iterations. It is unable to split the shape without implementing a special procedure and encompasses both test shapes.

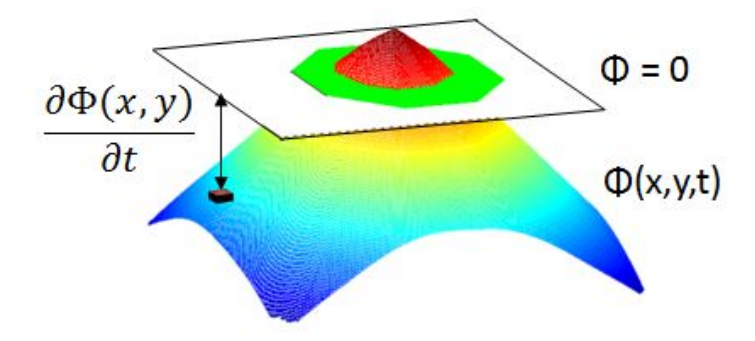


Figure 2–6: Visual representation of a level set surface intercepting a test image containing an octagon. The contour is defined by this intercept.

2.2.2 Implicit Representation: Level Set Method

The implicit approach to active contours involves the use of a level sets mapping to represent the contour boundary. This technique was influenced and developed from the work of Osher and Sethian [24] in 1988.

A level-set is a scalar function (ϕ) that adds an additional dimension to the image space, defining a surface (in a 2D case), the zero-crossing of which defines the contour boundary (ie. $\phi(C,t)=0$). In this case, C represents the contour

curve and t, time. In an explicit representation, the expansion and contraction of the contour is defined by the movement vectors of the boundary points, the level sets function expands and contracts through raising and lowering of the level sets function according to Equation 2.4 and shown in Figure 2–6.

$$\frac{\delta\phi}{\delta t} = V(\kappa) |\nabla\phi| + F(\Theta) \tag{2.4}$$

This is a simplified representation of a level set evolution function where $V(\kappa)$ is a function of the curvature and image gradient and $F(\theta)$ represents the external forces such as shape related constraints. κ represents the curvature term and can be calculated numerically from ϕ using Equation 2.5.

$$\kappa = \nabla \left(\frac{\nabla \phi}{|\nabla \phi|} \right) \tag{2.5}$$

Using level sets allows significant advantages such as stability, and intuitive curve breaking and combining as shown in Figure 2–7. However it is dependant on image gradients to determine the stopping point. Some objects may not have clearly defined borders encompassing the entire shape and thus are prone to leakage issues where the active contours grows beyond the boundary of the object. An alternative formulation of the variational framework was proposed by Mumford and Shah in 1989 [25]. Here the following energy function is minimized:

$$F(u,C) = \sum_{i} \mu_{i} \int \int_{\Omega} |u - g_{i}|^{2} dx dy + \nu |K|, \qquad (2.6)$$

where u refers to the image in question, particularly the set of intensity values for each pixel in question and x and y in this context symbolize the Euclidean coordinates within a 2D image. Here μ and ν are positive weighting coefficients for the different terms of the function. The first term attempts to minimize the difference between the intensity values found in each region, indexed by i and g_i the mean value within these regions. The second term is a shape energy term, and determines the overall curvature of the final contour. High values lead to more rounded contours with fewer regions of high curvature (ie. corners). Ω in this context defines the region of possible values of x and y. For example, the simplest application of the Mumford Shah formulation contains two regions, inside and outside the contour boundary usually represented by Ω_- and Ω_+ , the union of which constitutes the entire image space. This approach was combined with a level set formulation in the Chane-Vese implementation in which the proposed energy function follows Equation 2.7 [26].

$$E(\psi, u) = \sum_{i} \int_{\Omega} (I(x) - u_{1})^{2} H(\psi) + (I(x) - u_{2})^{2} (1 - H(\psi)) dx + \nu \int_{\omega} |\nabla H(\psi)| dx$$
(2.7)

Where E is the energy and u_1 and u_2 are the mean intensity values for inside and outside the contour. $H(\psi)$ is the Heaviside step function where $H(\psi) = 1$ for $\psi > 0$ and $H(\psi) = 0$ for $\psi < 0$. The edge function $H(\psi)$ forces an evaluation of the function at the edge of the contour solely instead of updating the entire level sets function which would slow down the algorithm and is potentially unnecessary.

The cost function can be minimized using the following Euler-Lagrange equation:

$$\frac{\partial \psi}{\partial t} = -\frac{\partial E}{\partial \psi} = \delta(\psi) \left(\nu \kappa + (I(x) - u_2)^2 - (I(x) - u_1)^2 \right)$$
 (2.8)

Alternative edge functions $(H(\psi))$ have been used in the literature such as by Zhao et al. [27].

$$H_{\eta}(\psi) = \begin{cases} 1 & \text{if } x > \eta \\ 0 & \text{if } x < -\eta \\ \frac{1}{2} \left[1 + \frac{x}{\eta} + \frac{1}{\pi} \sin\left(\frac{\pi x}{\eta}\right) \right] & \text{if } |x| \le \eta \end{cases}$$

$$(2.9)$$

$$\delta_{\eta}(x) = H'_{\eta}(x) = \begin{cases} 0 & \text{if } |x| > \eta \\ \frac{1}{2\eta} \left[1 + \cos\left(\frac{\pi x}{\eta}\right) \right] & \text{if } |x| \le \eta \end{cases}$$
 (2.10)

Where η is a scale factor that scales the smoothness of the edge function. Here, $H'_{\eta}(x)$ represents the spatial derivative of $H_{\eta}(x)$, used as a smoother approximation to the $\delta_{\eta}(x)$ function in 2.8. Chan and Vese utilized an alternative edge function of the following formulation:

$$H_{\eta}(x) = \frac{1}{2} \left(1 + \frac{2}{\pi} arctan(\frac{x}{\eta})\right)$$
 (2.11)

$$\delta_{2,\eta}(x) = H'_{\eta}(x) = \frac{1}{\pi} \frac{\eta}{\eta^2 + x^2}$$
 (2.12)

This allows a smoother updating to the level set function, increasing the probability of finding a global minimum. Updating schemes like these have the risk of making the optimization unstable after a few iterations by introducing sharp gradients into the level set function. This requires a refreshing step where the level set

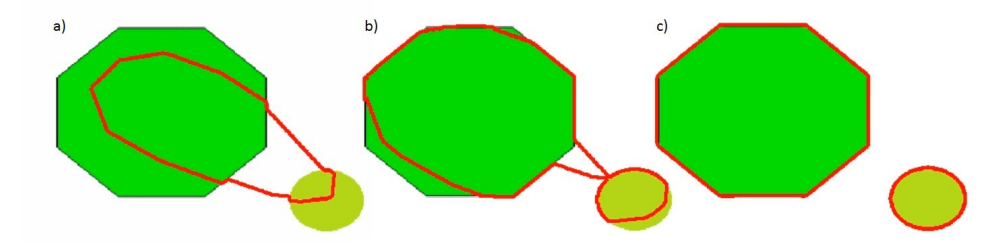


Figure 2–7: An example of the Chan Vese level set algorithm segmenting the same example from Figure 2–5. The procedure is shown after a) 1 iteration, b) 10 iterations and c) 25 iterations where the contour has split into two.

function is reinitialized by a distance function of the current contour boundary every few iterations.

In the case of equation 2.6 the objective function is defined at the distance between distribution means, however this can be replaced by other distance measures such as a probabilistic value infering class identity.

2.3 Registration

Image registration is the act of matching the space of two images through the use of a geometric transformation. Often one image is designated as the moving image (or reference image) while the second remains stationary (the target image). Image registration has been applied widely in the medical field under several strategies. The first of which is temporal image or intra-subject registration where the two images are of the same subject taken at different points in time or under different physical conditions. Some examples of commonly observed anatomical changes that may require registration include changes to tumor size, weight loss, movement of the lungs under free breathing, swallowing, filling/voiding of hollow organs and shifts in

organ position. This is important for studying disease progession, dose tracking or as a surgical aid.

The second category is inter-subject registration in which multiple subjects are registered together. This is often performed during the construction of atlases, which is a way of defining a population-based anatomical model. In essence it is an average of a large number of images of registered subjects. It represents an average model of the human body (or other species). Atlases are commonly used to automate the identification and segmentation of regular anatomy for radiotherapy treatment planning [28, 29], the study of variances in anatomy [30] or using abnormalities from the norm to determine areas of diseased tissue [31].

Multi-modality registration is another area that is commonly required in medical physics when incorporating information from a variety of imaging techniques such as computed tomography, magnetic resonance imaging, positron emission tomography, cone-beam computed tomography or ultrasound to name the more common ones. This is a particular challenge since each modality retrieves vastly different information with different resolving capabilities and contrast. Determining the proper way to measure image similarity is a challenging area that requires the utilization of alternative similarity criteria [32, 33, 34] and deformation constraints[35, 36]. Registering image information from multiple modalities can allow that information to be better utilized such as for improved target definition [37, 38], diagnosis, and prognosis [39, 40]. This is useful since images from multiple modalities often contain complementary information, such as the anatomical and functional information derived from CT and PET, respectively. Multi-modality registration is also commonly used

for intra-subject registration between the planning CT and CBCT during the day of treatment or patient alignment.

The process of registration requires the selection of several components: an objective function or metric, a transformation, an interpolation method, an optimization strategy, and regularization.

2.3.1 Metric

The objective function is the metric of similarity between the two images. Lower degrees of freedom, such as employing sets of points or surfaces to measure similarity are a quick way to evaluate positional alignment. These are best used to define rigid transformations however non-rigid applications are possible [41, 42]. The function defined by Equation 2.13 has been used to correctly match contours in order to register two radiographic images [43, 44].

$$D(X, T(Y)) = \sum_{i=1}^{N} w_i d^2(X, T(\vec{y_i})) = \sum_{i=1}^{N} w_i \left\| x_i' - \vec{T}(\vec{y_i}) \right\|^2$$
 (2.13)

In this metric D is the overall distance measure, X and Y define surfaces contained in the reference and target images. These surfaces can be defined as a series of points x_i and y_i of which there are N. The variable T defines the transformation while w_i represents a weighting factor associated with point i. The function d can be considered the distance function between the two surfaces assuming the point y_i is the closest available point to x_i when performing the summation.

One of the drawbacks of using limited degrees of freedom is how ill-posed the problem is. If the metric is not properly suited to the application such as non-rigid registration, the resulting transformation may be one of a large number of non-unique solutions. To better define the registration problem, intensity based metrics (using the similarity of pixel/voxel values) are more commonly used, in particular for non-rigid deformations. The simplest of these is the sum-of-squares differences (SSD) defined by Equation 2.14.

$$SSD = \sum_{i=1}^{N} (A_i - B_i)^2$$
 (2.14)

In this equation, A and B are the reference and target images, and i represents the index of summation over the N pixels/voxels contained in these images. Other variants of this metric include the sum of absolute differences (SAD), zero-mean sum of absolute differences (ZSAD), locally scaled sum of absolute differences (LSAD), zero-mean sum of squared differences (ZSSD) and the locally scaled sum of squared differences (LSSD). Some of the drawkbacks to using this type of metric is susceptibility to non-Gaussian noise [45] and the inability to consider multiple modalities. This is due to the intensity relationship not necessarily being one-to-one and one may in fact encounter inverse contrast patterns (ie. bone appearing with high attenuation in CT but low signal in MRI).

An alternative to this is to use correlative information metrics such as mutual information or entropy based measures such as those described in Section 2.4. These have been used to great effect to provide a metric for multimodal image registration [46, 33, 34].

2.3.2 Transformation

The choice of transformation is dependent on the type of alignment required by the reference and target images. The simplest transformations are labelled 'rigid' and involve translation and rotation. Additional degrees of freedom are afforded under affine transforms which add the possibility of shear and magnification. All four possible transforms can be defined using a 4x4 transformation matrix which acts on a 3D coordinate [x, y, z, 1]. The definitions for each transform are summarized by Equations 2.15, 2.16, 2.17 and 2.18.

$$T = \begin{bmatrix} 1 & 0 & 0 & d_x \\ 0 & 1 & 0 & d_y \\ 0 & 0 & 1 & d_z \\ 0 & 0 & 0 & 1 \end{bmatrix}$$
 (2.15)

Where T is the translation matrix defined by the three parameters d_x , d_y , and d_z defining the translation in the x, y and z euclidean planes.

The rotation matrices R_x , R_y , and R_z are defined around their respective axis of rotation and the degree of rotation around each is defined by Θ_x , Θ_y , and Θ_z .

$$R_{x}R_{y}R_{z} = \begin{bmatrix} 1 & 0 & 0 & 0 \\ 0 & \cos(\Theta_{x}) & \sin(\Theta_{x}) & 0 \\ 0 & -\sin(\Theta_{x}) & \cos(\Theta_{x}) & 0 \\ 0 & 0 & 0 & 1 \end{bmatrix} \begin{bmatrix} \cos(\Theta_{y} & 0 & \sin(\Theta_{y} & 0) \\ 0 & 1 & 0 & 0 \\ -\sin(\Theta_{y}) & 0 & \cos(\Theta_{y}) & 0 \\ 0 & 0 & 0 & 1 \end{bmatrix} \begin{bmatrix} \cos(\Theta_{z}) & \sin(\Theta_{z}) & 0 & 0 \\ -\sin(\Theta_{z}) & \cos(\Theta_{z}) & 0 & 0 \\ 0 & 0 & 1 & 0 \\ 0 & 0 & 0 & 1 \end{bmatrix}$$

$$(2.16)$$

Shear, unlike rotation is defined using the combination of two planes and the magnitude of shear in each plane is defined by the parameters S_x , S_y and S_z .

$$S_{x,y}S_{x,z}S_{y,z} = \begin{bmatrix} 1 & 0 & S_x & 0 \\ 0 & 1 & S_y & 0 \\ 0 & 0 & 1 & 0 \\ 0 & 0 & 0 & 1 \end{bmatrix} \begin{bmatrix} 1 & S_x & 0 & 0 \\ 0 & 1 & 0 & 0 \\ 0 & S_z & 1 & 0 \\ 0 & 0 & 0 & 1 \end{bmatrix} \begin{bmatrix} 1 & 0 & 0 & 0 \\ S_y & 1 & 0 & 0 \\ S_z & 0 & 1 & 0 \\ 0 & 0 & 0 & 1 \end{bmatrix}$$

(2.17)

Magnification is represented by one simple multiplicative factor for each axis M_x, M_y and M_z .

$$M = \left[egin{array}{cccc} M_x & 0 & 0 & 0 \ 0 & M_y & 0 & 0 \ 0 & 0 & M_z & 0 \ 0 & 0 & 0 & 1 \end{array}
ight]$$

(2.18)

The collection of transformations defined here are considered global transforms (the transform is applied the same over the entire image). Higher degrees of freedom can be implemented into the transformation in order to account for deformation that are local in nature.

Localized transformations such as free-form deformations are defined using a series of points $p_i = [p_{x,i}, p_{y,i}, p_{z,i}]$ referred to as control points that are overlaid on

an image. These points are moved around, defining a field of vectors which define the transformation. There is variability in how these points are applied that offer advantages in efficiency and accuracy. Points can be placed randomly or in irregular locations as is the case with adaptive bases [47] and thin plate splines [48]. A sparse representation involves the regular placement of points in a grid at a much coarser spacing than the voxels of a given image and is a common technique [49] and can also be applied in a pyramidal fashion with increasingly higher point densities [50]. This is an effective way to reduce processing requirements and improve the ability to handle large deformations. A dense representation is one where a control point is placed at the center of every pixel/voxel and has been used very successfully in the case of the Demons registration algorithms variants [51, 52]. The drawback to using dense representations of course is the increased complexity and degrees of freedom of the registration problem and thus efficient ways of computing the deformation vector field are required.

Much of the work in free-form deformations is focused around applying proper deformation constraints centered around biomechanical properties of tissue such as with using Finite Element Analysis [53] or by ensuring diffeomorphism (invertibility) through maximization of cross-correlation [54] using a flexible algorithm called ANTs. This lead to success in the BRATS MICCAI segmentation challenge [55] and and the EMPIRE10 lung registration challenge [56].

2.3.3 Interpolation

The chosen interpolation method determines how the deformation is approximated away from where the vector field is defined. It also determines how gradient calculations are performed and can affect the algorithm complexity. Woods et al. used a linear summation of polynomials [57] to interpolate their values while Friston et al. used the Taylor expansion of a series of non-linear basis functions [58]. A common interpolation technique combined with non-rigid deformable registration is the use of cubic-B-splines (defined by Equation 2.19) [59] which define a surface and provide a smooth interpolation, eliminating discontinuities at boundaries.

$$\mathbf{u}(\mathbf{x}) = \sum_{l=0}^{3} \sum_{m=0}^{3} \sum_{n=0}^{3} B_l(\mu_x) B_m(\mu_y) B_n(\mu_z) \mathbf{d}_{i+l,j+m,k+n}$$
(2.19)

In this formulation, $i = \lfloor x/N_x \rfloor - 1, j = \lfloor y/N_y \rfloor - 1, k = \lfloor z/N_z \rfloor - 1, \mu_x = x/N_x - \lfloor x/N_x \rfloor, \mu_y = y/N_y - \lfloor y/N_y \rfloor$ and $\mu = z/N_z - \lfloor z/N_z \rfloor$ where N_x, N_y and N_z represent the image dimensions. B_l represents the basis functions of the B-spline and \mathbf{d} represents the displacement of the control point around which values are being interpolated. The operators $\lfloor \rfloor$ signify taking the floor of whatever value is inside. While smooth, cubic-B-splines do not prevent meshfolding or insure reversability of the transformation.

Thin plate spline (TPS) transforms are another widely used method that uses a series of radial basis functions (RBFs) to approximate the dense vector field from any number of irregularly spaced control points. TPSs can be defined by the form of Equation 2.20.

$$t(p) = ap + b + \sum_{i=1}^{N} c_i R(p - p_i)$$
 (2.20)

where p defines the coordinate of the point being transformed and thus t(p) defines the forward mapping. In this formulation an affine transformation is incorporated into the coefficients a and b in order to account for global transforms first. The parameters c_i are weighting functions of the RBF R while i is the control point index. A myriad of RBFs are available for use in the TPS [60, 61] so long as they are radially symmetric.

2.3.4 Optimization

In many cases, registration is an optimization problem involving the search for a global minima or maxima of the chosen cost function. To this end there are many techniques for improving the efficiency of the registration procedure by minimizing the number of search steps required. While there are many optimization techniques, here we will touch on a few of the more popular choices.

Gradient descent optimization involves calculating the gradient of the objective function as a result of changes to the parameters defining the transformation. If the objective function is intensity based, this calculation will heavily incorporate the chosen interpolation method into the gradient calculation through the use of the chain rule. The optimizer follows the gradient according to a set step size until a minima/maxima is reached. Gradient descent has a tendency to get stuck in local minima/maxima and requires a significant amount of processing to calculate the gradient.

Evolutionary optimizers randomly choose a number of step directions and sizes and evaluates the objective function with these new randomly perturbed values. The values with the most improved metric value are chosen to replace the previous generation. The one-plus-one evolutionary optimizer is one such example that evaluates one offspring at a time. This method is effective for avoiding local minima/maxima and reducing computation time as it doesn't require a gradient calculation [62].

The simultaneous perturbation stochastic approximation (SPSA) algorithm is a compromise between the gradient descent and evolutionary optimizers. The central idea behind this algorithm is that it evaluates the gradient based on a random perturbation of the deformation parameters. It uses two calculations of the objective function (as opposed to calculating the gradient directly) to approximate the step direction [63]. The finite differences stochastic approximation (FDSA) method is similar in approach but differs in that it estimates the gradient through perturbation of the parameters one at a time rather than all at once. This leads to a larger number of calculations but a better estimate of the gradient.

Another popular stochastic optimization technique is the simulated annealing (SA) algorithm inspired by the behaviour of crystalizing molecules during a drop in temperature and first published by Kirkpatrick, Gelatt and Vecchi in 1983 [64]. The algorithm randomly explores the solutions space in the neighbourhood of the current parameter values and probabilistically accepts solutions that offer a worse cost function value which is influenced by an iteratively decreasing temperature value T according to Equation 2.21.

$$P(J(t)) = \exp\left[-\frac{1}{T(t)}\max(0, J(t+1) - J(t))\right]$$
 (2.21)

Here J is the calculated cost function at step t and P is the probability of accepting a worse solution. For solutions where the cost function increases, the solution is automatically accepted. This ability to accept poorer solutions allows the algorithm to search over a wide area to find the global minima/maxima.

2.3.5 Regularization

The problem of registration is an ill-posed one, in that many possible solutions may exist for a chosen objective function. Additional constraints on the problem are often required in order to ensure specific properties such as smoothness, invertibility and proper biomechanical responses to strain in order to narrow down the number of acceptable solutions.

One way to apply additional constraints to ensure realistic deformations is through the use of parameterization. In this approach regularization is implicitly applied through the reduction in degrees of freedom. The transformation becomes parameterized through the use of basis functions. For examples the use of cubic-B-splines [59] and radial basis functions [60]. The choice of basis functions can ensure smoothness and reduce irregularities since if the basis functions are twice differentiable, so is the transformation.

The second approach is by applying a filter to the deformation field. This often involves the convolution of a kernal such as a Gaussian function [52, 65, 66]. This can be applied in two ways, the first in an elastic manner where the filter is applied to the deformation field, the second is a fluid approach where it is applied to the velocity or update to the deformation field [67]. The latter method allows more extreme deformations to take place. Specialized anisotropic filters that impose

differential filtering rules in order to approximate the expected deformation rigidity of certain regions have also been applied [68]. The advantages to using a filter are simplicity and ease of calculation, the drawback is that by applying it repeatedly, we homogenize the deformation field. While this may be good for eliminating random vectors that might arise in homogenous image regions, it reduces the accuracy of the deformation at the borders of objects or areas of high information content so a balance is required.

The third approach is the usage of Sobolev spaces in which the deformation is defined within a space that is already regularized. Examples of this include Trouve et al. [69] and Chefd'hotel et al. [70] in their application to diffeomorphic image registration, a technique which seeks to ensure invertibility of the transform.

The final group of methods is to apply penalty terms to the registration process. These are additional terms calculated once the vector field velocity has been calculated and include things such as smoothness by penalizing the first and second derivatives of the deformation, incompressibility, rigidity and invertibility. These can be applied as soft constraints where the terms are added to work against the deformation vector field or as a hard constraint [71].

2.4 Information Theory

In this section we will review the background of information theoretics and how divergence measures between distinct distributions are estimated. The goal of this section is an explanation of how the Jensen Rényi divergence and statistical similarity measures in general are calculated, beginning with the estimation of the probability densities, from there the calculation of entropy is followed by its further adoption in calculating mutual information and finally, a similar divergence metric, the Jensen Rényi divergence. We begin with a Gaussian distribution shown in Figure 2–8.

Exact calculation of the population histogram would be computationally expensive depending on the population size, so instead, Parzen windows can be used to approximate the distribution using a subset of samples. This is explained in excellent detail by Viola and Wells when proposing mutual information for image alignment [46] and Duda and Hart [72]. A Parzen window is essentially a convolution of a subset of samples in order to estimate the population histogram. This is defined by Equation 2.22.

$$P_{\Omega}(x) = \frac{1}{N} \sum_{i \in \Omega}^{N} K(x - x_i)$$

$$(2.22)$$

Where $P_i(x)$ is the probability density of a value x occurring, N is the number of subsamples taken and K is the Parzen window function. Ω and i refer to the subset of samples and sample index respectively. x_i in this context then refers to the values of samples contained with the set Ω . K does not have to be Gaussian like in Equation 2.23 but for many applications it allows further simplifications.

$$K(x) = (2\pi)^{-(n/2)} |\psi|^{\frac{-1}{2}} \exp{-\frac{1}{2}x^T \psi^{-1} x}$$
(2.23)

In this context, n is the dimensionality of the distribution space. For example if we were to sample from a color image with RGB channels, the dimensionality would be 3. If the dimensionality if larger than 1, then x becomes an n-dimensional array of samples. T in this context refers to the transpose of the array x, and ψ is the variance x.

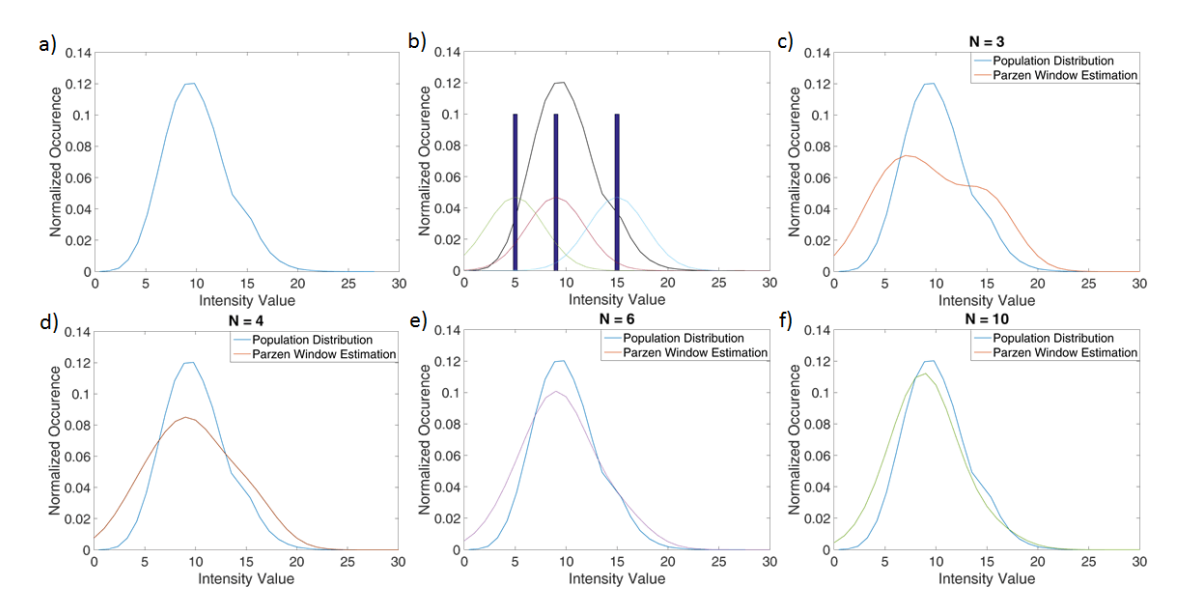


Figure 2–8: Example of the use of a Gaussian Parzen window to estimate an intensity distribution. Part a) shows the population distribution, b) three values sampled from the distribution along with their surrounding Parzen windows. In c) we see the addition of the Parzen windows of all three samples compared to the original distribution, this is further refined with more samples in d)-f).

Returning to our previous example we can see how the Parzen window operates for a subset of samples in Figure 2–8 part b). In Figure 2–8 parts c)-f) we can see how quickly the subsampled probability distribution approaches the population distribution. To this end, once the probability distribution can be estimated, it is relatively straight forward to calculate the entropy of sample set x which in this thesis exclusively refers to a series of intensity values sampled from an image or image region. The formula for entropy in this context is shown in Equation 2.24.

$$H(x) = -\int P_{\Omega}(x) \ln \left(P_{\Omega}(x)\right) dx \tag{2.24}$$

In this case, the integral is over the range of possible values that x can take on. For the purposes of registration, it is convenient to think of entropy as a measure of information contained within an image. Similarly, joint entropy is a measure of the information contained in a superposition of two distributions - e.g. two images - and is defined by equation 2.25.

$$H(x,y) = -\int P_{\Omega}(x,y) \ln \left(P_{\Omega}(x,y)\right) dxdy \qquad (2.25)$$

Where the probability density is now two dimensional and x in Equation 2.23 is now replaced with the 2D array [x, y] in Equation 2.25. The key to understanding how these relate is knowing that there will be similarities between the two distributions, P(x) and P(y), with larger similarities reducing the total information/uncertainty content or the joint entropy. If we think of the two distributions as a Venn diagram as shown in Figure 2–9, with two circles representing H(x) and H(y) for the two distributions, H(x, y) would be the union of the two.

If we wish to measure the information redundancy (or the overlapping region of the venn diagram) we can calculate a measure known as Mutual Information (MI). The formulation is fairly intuitive using the given analogy, it is shown in Equation 2.26

$$MI(x,y) = H(x) + H(y) - H(x,y)$$
 (2.26)

Mutual information is one example of a statistical divergence measure, meant to quantify the similarity between two distributions. This is particularly useful for medical imaging applications when comparing images from two modalities such as

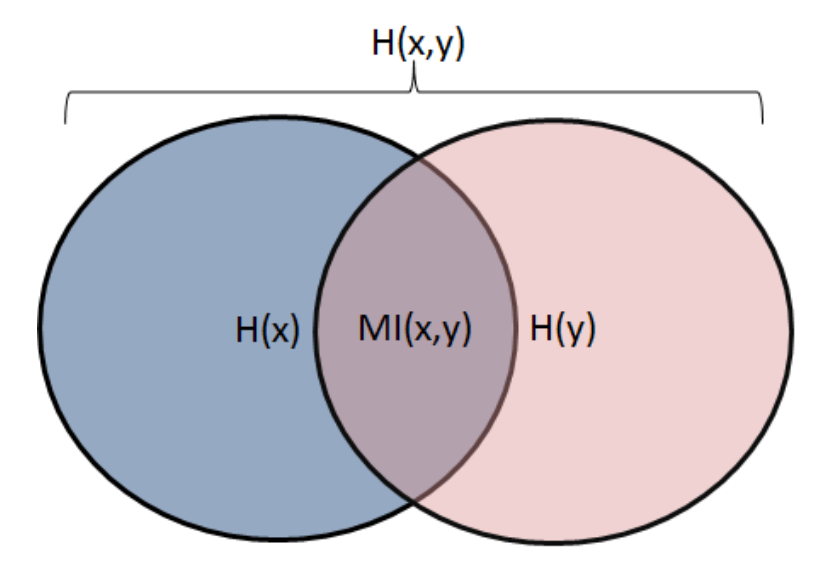


Figure 2–9: A Venn diagram explanation of mutual information, represented as the overlap symbolizing the redundant information described by two populations or in our context intensity values taken from two images or image regions. Each circle represents the entropy/image information from each of these populations. The joint entropy is effectively the union of these two circles/entropies.

MRI and CT where the intensity values will contain similarities but do not have a one-to-one relationship.

Another entropy measure that can be used is the Rényi entropy

$$R_{\alpha}(x) = \frac{1}{1-\alpha} \log \left(\sum_{i=1}^{N} P(x)^{\alpha} \right)$$
 (2.27)

Where α is a new parameter controlling the weighting of frequently versus infrequently occurring intensity values defined by x in this case. The logarithm in this case is of base 2. The Rényi entropy is a generalized entropy metric that can be formulated as other entropy values with the choice of α . For example an α of 1 produces the Shannon entropy used in mutual information. In this context the Rényi entropy does not provide a new antropy measure but allows us a method of switching between a large range of measures using the free parameter α . There is additional freedom in being able to use it a continuous parameter in this way. The parameter α plays a large role in how incoherent noise is handled when using this information metric as values with lower probability density can be minimized in their influence. As α increases, the influence of highly probable values increases. This will not affect how coherent image artifacts are handled since that could significantly shift the mean value of the intensity distribution. In other words, the image artifact would result in highly frequent intensity values which this entropy measure would be susceptible to.

Similar to before, the similarity or divergence measure that we extract from multiple images is summarized in Equation 2.28.

$$JR_{\alpha}(x,y) = \frac{1}{1-\alpha} \left[\log \left(\sum_{i=1}^{N} \left(w_1 P_1(x) + w_2 P_2(y) \right)^{\alpha} \right) - \log \left(\sum_{i=1}^{N} P_1(x)^{\alpha} \right) - \log \left(\sum_{i=1}^{N} P_2(y)^{\alpha} \right) \right]$$
(2.28)

Where w_1 and w_2 are weights for probability densities 1 and 2. The divergence measure, termed the Jensen Rényi divergence is named after mathematicians Johan Jensen and Alfréd Rényi [73]. Further details about the measure are covered in Chapter 3.

CHAPTER 3

Novel multimodality Segmentation Using Level Sets and the Jensen-Rényi Divergence

This chapter represents a print of "D. Markel, H. Zaidi, and I. El Naqa, Novel multimodality segmentation using level sets and jensen-rényi divergence, Medical Physics 40, 121908 (2013)". In it we describe the application of the Jensen Rényi divergence as a cost function/metric in optimizing the surface contour for defining tumor boundaries and the boundaries of image objects in general. Experiments are performed in order to discern the advantages of using this metric for object segmentation, particularly in the presence of random noise. Phantom and human examples are used to test the algorithm.

3.1 Abstract

Purpose: Positron emission tomography (PET) is playing an increasing role in radiotherapy treatment planning. However, despite progress, robust algorithms for PET and multimodal image segmentation are still lacking, especially if the algorithm were extended to image-guided and adaptive radiotherapy (IGART). This work presents a novel multimodality segmentation algorithm using the Jensen-Rényi divergence (JRD) to evolve the geometric level set contour. The algorithm offers improved noise tolerance which is particularly applicable to segmentation of regions found in PET and cone-beam computed tomography.

Materials and Methods: A steepest gradient ascent optimization method is used

in conjunction with the JRD and a level set active contour to iteratively evolve a contour to partition an image based on statistical divergence of the intensity histograms. The algorithm is evaluated using PET scans of pharyngolaryngeal squamous cell carcinoma with the corresponding histological reference. The multimodality extension of the algorithm is evaluated using 22 PET/CT scans of patients with lung carcinoma and a physical phantom scanned under varying image quality conditions.

Results: The average concordance index (CI) of the JRD segmentation of the PET images was 0.56 with an average classification error of 65%. The segmentation of the lung carcinoma images had a maximum diameter relative error of 63%, 19.5% and 14.8% when using CT, PET and combined PET/CT images, respectively. The estimated maximal diameters of the gross tumor volume (GTV) showed a high correlation with the macroscopically determined maximal diameters, with an R^2 value of 0.85 and 0.88 using the PET and PET/CT images, respectively. Results from the physical phantom show that the JRD is more robust to image noise compared to mutual information and region growing.

Conclusions: The JRD has shown improved noise tolerance compared to mutual information for the purpose of PET image segmentation. Presented is a flexible framework for multimodal image segmentation that can incorporate a large number of inputs efficiently for IGART.

3.2 Introduction

Radiotherapy is an important modality for treating patients with cancer. About 60-70% of all cancer patients receive irradiation as part of their treatment [74] and

this remains the main option for advanced stages of disease. However, geometric and dosimetric uncertainties during fractionated radiotherapy can accumulate daily from tumor regression, soft-tissue deformations and organ motion. Traditionally, computed tomography (CT) has been the principal modality used for radiotherapy treatment planning. However, several studies have shown inter- and intra-observer variability in manual gross tumor volume (GTV) delineation as high as 700% [75, 76, 9] and 80% [77] using CT alone, respectively. The inclusion of PET into the treatment planning process has provided improved contrast and increased sensitivity to metabolically active regions of the tumor versus normal background tissue. However, PET suffers from relatively low spatial resolution, variable uptake patterns and quantum image noise. These properties can drastically influence the intended treatment target.

Even assuming perfect initial target definition, a patient's anatomy as well as the target itself may change drastically during the course of treatment. Tumor regression in the lung on the order of 1.2% of the volume per day was observed in a study by Kupelian et al.[78] using megavoltage CT images. In a study by Barker et al. an average volume change of 1.8% per day was observed in the head and neck [79]. In the same study average weight loss of 7.1% of the body mass was observed over the course of treatment. The feasibility of image-guided adaptive radiotherapy (IGART) relies on fast and accurate algorithms that can reduce treatment planning time[80]. Often cone-beam computed tomography (CBCT) or mega-voltage computed tomography (MVCT) is used to check the anatomical context of the patient. These modalities

tend to suffer from a reduction in contrast and increase in image noise, thus making it difficult to redefine the target boundary accurately.

A large number of automated and semi-automated methods have emerged in the literature attempting to provide consistent interpretation of the tumor boundary. These have included a large number of soft threshold values ranging within 15-50% of the maximum Standardized Uptake Value (SUV) [81, 82, 83, 84, 85], and a hard value of 2.5 SUV [86]. Further work has produced regression formulas to predict the most appropriate threshold value based on either mean SUV [87], lesion volume [88] or signal to background ratio (SBR) [89]. However, a few studies have noted that no appropriate threshold value exists that consistently and accurately determines the GTV boundary [88, 90]. This is partially due to inconsistent FDG-PET uptake from patient to patient as well as heterogeneous uptake patterns that are often seen within the tumor regions themselves. More advanced methods such as those using fuzzy hidden Markov chains [91] or Markov random fields [92] have been proposed which make use of stochastic modelling to fit Gaussian functions to the intensity distributions, using each voxel's class probability and agreement with surrounding voxels to randomly shuffle it around into other data classes. This process eventually converges, and finally classifies the voxels in the image into a number of hard classes. The information from surrounding voxels is often used to reduce errors produced by image noise. More recently, clustering methods have been receiving considerable attention due to the fact that they are able to approximate the intensity distributions of the segment and background without any knowledge about the shape of the distributions [93, 94, 95]. Another popular method that has often seen commercial implementation is the atlas-based approach that uses the coregistration of a large database of patient scans to produce a probabilistic map of expected uptake values for healthy patients and then uses deviations from this map to determine where abnormal regions lie [96][97]. While there has been a plethora of work regarding proper PET segmentation, the problem remains a challenging one that has not been satisfactorily resolved using single modality methods. A more thorough review of PET segmentation algorithms can be found in surveys by Zaidi and El Naga [98] and Sheperd et al. [99].

We have adapted an active contour approach due to its ability to define the contour using a continuous function which can intuitively adapt to topological changes such as splitting and merging of multiple regions, as encountered in a heterogenous tumor and to achieve sub-pixel accuracy. Active contours are a class of methods by which an initialized segment is evolved over time to maximize a chosen energy function. Internal forces specific to the shape of the contour along with external forces from the image itself are both used in this evolutionary process which follows the gradient field of the function. The active contour can be defined explicitly as is the case with snakes [100] where the contour is given by the positions of a set of points, or implicitly as with level sets [24, 101], where it is represented by the zero level of a scalar function.

Another important facet of our work regards the consideration of complementary information from different modalities to delineate the so called "biophysical" target [101]. A study by Milker-Zabel *et al.* [102] showed that with the inclusion of PET, CT and MRI modalities into the treatment planning process for stereotactic

radiotherapy resulted in changes to the target definitions 73\% of the time. The challenge with multi-modality treatment planning stems from registering patient images that often do not include a high degree of correlating details. The inclusion of hybrid PET/CT imaging devices over the past ten years has greatly aided in reducing interobserver variability in target definition [103, 104] by providing physically registered datasets. The interpretation of visual information from multiple images is another source of variability that may be aided by computer automation. A number of algorithms addressing the issue of multimodality segmentation, particularly with regards to PET/CT segmentation have been recently published [105, 106, 107, 101, 108]. These include a simple region growing method where the user places a seed within the area to be segmented which then begins to absorb surrounding voxels that fall within a given intensity range, growing until it fills the entire connected region. This method has been applied in the context of the lung [105] using PET/CT images but found to produce systematic overestimation of the tumor boundary. Probabilistic classification using a number of textural filters and machine learning techniques trained on a set of previously observed cases has been shown to produce accurate results in the head and neck area [106]. Within the same area of the body, a semiautomated graph-based method has been tested that uses Markov Random Fields to produce globally optimal solutions [107]. Within our own group, we have applied an active contour to the task of PET/CT segmentation with the development of the multivalued level sets segmentation method [101]. This method employed an energy metric based on differences between voxel intensity and the mean intensity values found inside and outside the segment. This approach however, does not account for the spread and shape of individual image intensity distribution reducing each to a single weighting parameter in the algorithm.

The Jensen-Rényi divergence (JRD) is a relatively new generalized information divergence measure whose curvature can change based on a chosen parameter (α) . Our implementation relies on a non-parametric approach that makes no assumptions about the underlying distribution. Some studies have observed that the JRD is more robust to image noise than mutual information when applied to registration as long as the weighting parameters are chosen appropriately [73][109]. Mutual information is a common objective function for registration tasks, and while it is not commonly used for segmentation, it is based on entropy terms which a number of authors have investigated for use in segmentation[110, 111, 112, 113]. The use of entropy based on intensity value histograms (in particular using non-parametric density estimates) is an effective objective for statistically based segmentation. Using the metric, it is possible to partition regions with subtle differences in their intensity distribution that may be too difficult to detect with simple average intensity methods or the naked eye. Mutual information also has a similar mathematical formulation to the JRD and hence is used for comparison in this paper. To date the JRD has not been applied as a metric for segmentation using a level set active contour framework. The goals of this work are threefold. First we show that the JRD can improve noise tolerance when applied to the task of segmentation using PET and CT scans of an in-house phantom. Second, we evaluate the JRD based level sets method with regards to PET segmentation using PET scans of patients with pharyngolaryngeal squamous cell carcinoma. Third, we demonstrate its application to segmentation of multimodality PET/CT scans of patients with lung carcinoma.

3.3 Materials and Methods

The implementation and validation of the proposed method is developed in this section starting with a theoretical background of the energy term used in level sets method. Here we present the derived solution to the level sets differential equation using the JRD. The materials and methods for collecting the validation data along with an explanation of the validation metrics is then provided followed by hardware and software specifications of our implementation.

3.3.1 Theory

Level Sets

A level set function $\phi(u, v, w)$ is used to implicitly define a contour within our image where x = (u, v, w) defines a set of 3D cartesian coordinates within the image volume. ϕ is a scalar function that defines the contour edge by its zero level $(\phi(u, v, w) = 0)$.

Let E be a function of a level set. The successive iterations of the minimization/maximization of E using a steepest descent/ascent approach corresponds to a specific evolution of the level set, and hence of its zero level.

$$E(\phi) = \int_{\Omega} (JRD(\phi(x)) + \mu |\nabla H(\phi(x))| - \nu) dx$$
 (3.1)

Where $JRD(\phi)$ is the Jensen Rényi divergence, ν is a scalar velocity term, dx is an infinitesimally small volume at point x (which is defined by the image resolution), Ω is the set of sampled voxels in the image, $|\nabla H(\phi)|$ is the magnitude of the gradient of

the Heaviside function (which forces a smooth boundary) and is defined by equation 3.3.1, μ is a weighting factor. Following curve evolution theory, evolving the energy function over time is equivalent to finding the derivative over the contour.

$$\frac{\partial \phi}{\partial t} = \frac{\partial E(C)}{\partial C} \tag{3.2}$$

Where C is the contour at the current iteration defined by the zero level ($\phi(C)$ = 0) of the level set function.

$$H(\phi) = \begin{cases} 1 & \text{if } \phi \ge 0 \\ 0 & \text{if } \phi < 0 \end{cases}$$
 (3.3)

The Jensen Rényi divergence

For estimation of the JRD, we start by defining a set of samples from either outside or inside a contour by x_i , i = 1, 2, ...n where n is the sample size and i is the sample index. If we let $P = (P(J(x_1), \Omega), P(J(x_2), \Omega)...P(J(x_n), \Omega))$ be the probability density distribution where $J(x_i)$ is the intensity value of sample x_i then we can define the Jensen Rényi entropy using equation 3.4.

$$R_{\alpha}(P) = \frac{1}{1-\alpha} \log \sum_{i=1}^{n} P(J(x_i), \Omega)^{\alpha}$$
(3.4)

Where J(x) is the feature vector at point x made up of the intensity values of the input images and α defines the curvature of the function. For $\alpha \in (0,1)$ the function is concave, whereas it is neither convex nor concave for $\alpha > 1$. Choosing an α value of 1 gives back the Shannon entropy. The JRD criterion is defined by the following conditional expectation:

$$JRD(\phi) = R_{\alpha} \left(\sum_{k=1}^{d} w_k P_k \right) - \sum_{k=1}^{d} w_k R_{\alpha}(P_k)$$

(3.6)

$$= \frac{1}{1-\alpha} [\log \int_{\Re} (w_1 P_1(J, \Omega_-) + w_2 P_2(J, \Omega_+))^{\alpha} dJ -$$

$$w_1 \log \int_{\Re} (P_1(J, \Omega_-))^{\alpha} dJ - w_2 \log \int_{\Re} (P_2(J, \Omega_+))^{\alpha} dJ]$$

where w_1, w_2 are the weighting parameters for the probability distribution functions P_1 and P_2 . P_1 and P_2 in this context are defined by the intensity distributions inside and outside the evolving level set, respectively. d is the number of regions/distributions and \Re is the domain of feature values represented by J. The set of samples defining these regions is referred to by Ω_- for inside the segment and Ω_+ for outside the segment.

The divergence measure changes with the parameter α . For example, when alpha is equal to 0.5, the divergence is proportional to the log of the Bhattacharyya coefficient. When α is chosen to be 1, Rényi entropy reduces to the Shannon entropy (SE in equation 3.8) and the measure becomes the Jensen-Shannon divergence. This becomes equivalent to mutual information when the weighting parameters w_1 and w_2 are chosen equal to $P_1(J, \Omega_-)$ and $P_2(J, \Omega_+)$ for each sample[73]. The weighting parameters determine the importance of probability distributions P_1 and P_2 which in this case represent the foreground and background. For this work the weighting

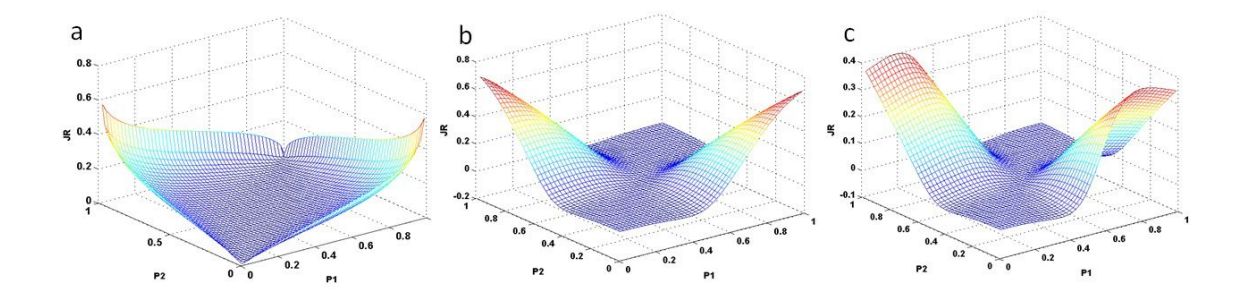


Figure 3–1: Mesh plots of the JRD energy space using Bernoulli distributions for P_1 and P_2 . In this context $P_k = (p_k, 1 - p_k)$ replaces $P(J(x_i), \Omega)$ in equations 3.4 and 3.8. In a) alpha is chosen equal to 1 with equal weights. b) shows the function with $\alpha = 5$ and equal weights. c) shows the function with $\alpha = 5$, $w_1 = 0.75$ and $w_2 = 0.25$. The segmentation algorithm would maximize the JRD, these are the spots in the energy space where there is the largest difference between P_1 and P_2 if the weighting values are equal. Changing the weighting parameters affects where these maxima occur.

parameters were chosen to be 0.5 each. On a continuous basis, α can be seen to change the curvature of the divergence measure as shown in figure 3–1. Here \Re covers the domain of possible intensity values. For our implementation, volumes were discretized to 40 levels in order to reduce processing time requirements.

$$SE(P) = -\sum_{i=1}^{n} P(J(x_i), \Omega) log(P(J(x_i), \Omega))$$
(3.8)

The probability distribution functions are defined as follows:

$$P(J,\Omega) = \frac{1}{n} \sum_{i=1}^{n} K_{\psi} (J - J(x_i)), \qquad (3.9)$$

where

$$K_{\psi}(J - J(x_i)) = (2\pi)^{-t/2} |\psi|^{-1/2} \times exp\left(-\frac{1}{2} (J - J(x_i))^T \psi^{-1} (J - J(x_i))\right). (3.10)$$

Where K_{ψ} is the Gaussian kernal used for the Parzen window estimation of the probability density[114]. Here ψ represents the covariance matrix of the feature vector J. This can be calculated directly from the vector J, however this makes the assumption that the data is best represented by two unimodal distributions. Since we want to make no assumptions about the shape of the distributions, every covariance matrix was set to a $t \times t$ matrix with every diagonal element equal to 8 which was determined heuristically. Here t is the dimensionality of the feature vector J.

$$\frac{\partial \phi}{\partial t} = \delta(\phi) \left(\left(\frac{\nabla \phi}{|\nabla \phi|} \right) + \frac{1}{1 - \alpha} \frac{\int_{\Re} \alpha \left(w_1 P_1(J, \Omega_-) + w_2 P_2(J, \Omega_+) \right)^{\alpha - 1} \left(w_1 \frac{\partial P_1}{\partial C} + w_2 \frac{\partial P_2}{\partial C} \right) dJ}{\int_{\Re} \left(w_1 P_1(J, \Omega_-) + w_2 P_2(J, \Omega_+) \right)^{\alpha} dJ} - \frac{1}{1 - \alpha} w_1 \frac{\int_{\Re} \alpha P_1(J, \Omega_-)^{\alpha - 1} \frac{\partial P_1}{\partial C} dJ}{\int_{\Re} P_1(J, \Omega_-)^{\alpha} dJ} - \frac{1}{1 - \alpha} w_2 \frac{\int_{\Re} \alpha P_2(J, \Omega_+)^{\alpha - 1} \frac{\partial P_2}{\partial C} dJ}{\int_{\Re} P_2(J, \Omega_+)^{\alpha} dJ} - \nu \right)$$
(3.11)

Where $\delta(\phi)$ (the dirac delta function) is approximated by the following

$$\delta(\phi) = \frac{1}{\pi\epsilon \left(1 + (\phi/\epsilon)^2\right)} \tag{3.12}$$

Where ϵ is a small number arbitrarily chosen to be 10^{-7} . The partial derivatives of the probability densities are

$$\frac{\partial P_1}{\partial C} = \frac{\partial P_1(J,\Omega_-)}{\partial C} =$$

$$\frac{1}{|\Omega_-|} \left(-K_{\psi_1}(J(C) - J) - P_1(J,\Omega_-) \right)$$
(3.13)

$$\frac{\partial P_2}{\partial C} = \frac{\partial P_2(J, \Omega_+)}{\partial C} =$$

$$\frac{1}{|\Omega_+|} \left(P_2(J, \Omega_+) - K_{\psi_2}(J(C) - J) \right)$$
(3.14)

When using p multiple inputs, or in our case multiple images, the vector of intensity values, J simply becomes a $p \times n$ vector where each data point is sampled from the same spatial location in the domain of the images. A maximum sample size of 1600 voxels or the total number of voxels in a sample region (whichever is smaller) is used to estimate the probability distribution functions for inside and outside the segment. The samples are randomly taken from the inside of the segment and an equally sized area surrounding it which is created using a distance transform of the contour edge and masking the values within the appropriate distance.

A similar derivation can be performed on the mutual information metric using Equation 3.15.

$$\frac{\partial MI(\phi)}{\partial C} = -\int_{\Omega} \left(\frac{(x)}{\partial C} log(P(x)) - \frac{\partial P(x)}{\partial C} \right) dx$$

$$-\int_{\Omega} \left(\frac{(y)}{\partial C} log(P(y)) - \frac{\partial P(y)}{\partial C} \right) dy$$

$$+\int_{\Omega} \left(\frac{\partial P(x,y)}{\partial C} log(P(x,y)) - \frac{\partial P(x,y)}{\partial C} \right) dy$$
(3.15)

Where x and y in this context integrate over the intensity value ranges from images 1 and 2 over the entire image space (assuming a multi-modal segmentation). For monomodal images, the image was input twice. The inside and outside image regions are defined by splitting the integral for the inside and outside regions, Ω_{-} and Ω_{+} .

$$\frac{\partial H(x)}{\partial C} = \int_{\Omega_{-}} \left(\frac{\partial P(x)}{\partial C} \ln P(x) - \frac{\partial P(x)}{\partial C} \right) - \int_{\Omega_{+}} \left(\frac{\partial P(x)}{\partial C} \ln P(x) - \frac{\partial P(x)}{\partial C} \right)$$
(3.16)

This is used for attaining the results in Figures 3–8.

3.3.2 Datasets and Validation

Experimental Phantom Studies

A physical phantom was constructed in order to evaluate the performance of the algorithm under varying conditions of image quality. This was done by placing a small glass jar with a 64 mm inner diameter with 4 mm thick walls wrapped in a 3 mm thick bolus sheet inside a larger glass jar with an outer diameter of 111 mm and 7 mm thick walls which is shown in figure 3–2. Thread seal tape was used to make the larger jar water tight. The phantom was filled with a solution of approximately 950 ml of water with 8.7875 MBq of ¹⁸F-FDG radiotracer for a concentration of 9250 Bq/ml. The inner jar is not sealed allowing the solution to mix inside the phantom producing a 1:1 concentration between the inside and outside of the inner jar. The purpose of this phantom was to have the semi-automated algorithm attempt to segment the boundary of the inner jar without spilling into the surrounding region. The phantom was scanned using a GE Discovery-ST PET/CT

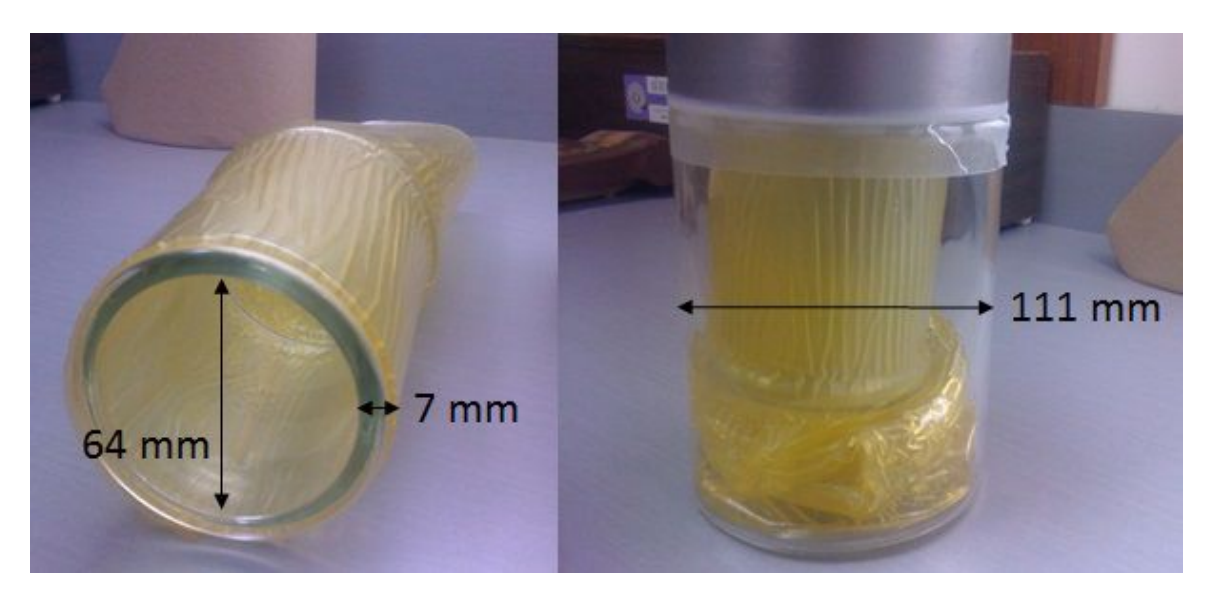


Figure 3–2: The inner jar wrapped in the bolus sheet (left) and the two containers, one inside the other (right).

scanner (GE Healthcare) and reconstructed into a series of 128x128 voxel images with a resolution of 5.4688 mm in the transverse plane and a slice thickness of 3.27 mm using the ordered subset expectation maximization (OSEM) algorithm.

In order to achieve a variety of SNR values, 6 scan times of 4, 6, 9, 15, 62 and 246 seconds were chosen to produce 6 volumes. The measured SNRs from these scans were 9.1, 9.2, 10.9, 12.6, 17.8 and 26.0 dB using the definition of SNR given by equation 3.17. Where μ_{sig} and σ_{bkg} are the mean and standard deviation of the signal and background. The signal in this case is the water within the inner jar since it contained the FDG where as the wall of the inner jar and the bolus emitted no signal and was thus considered background. Since the wall and the bolus occupied very little area, the region over the entire volume was used to provide a more accurate calculation of standard deviation. For the CT, μ_{sig} and σ_{bkg} are the

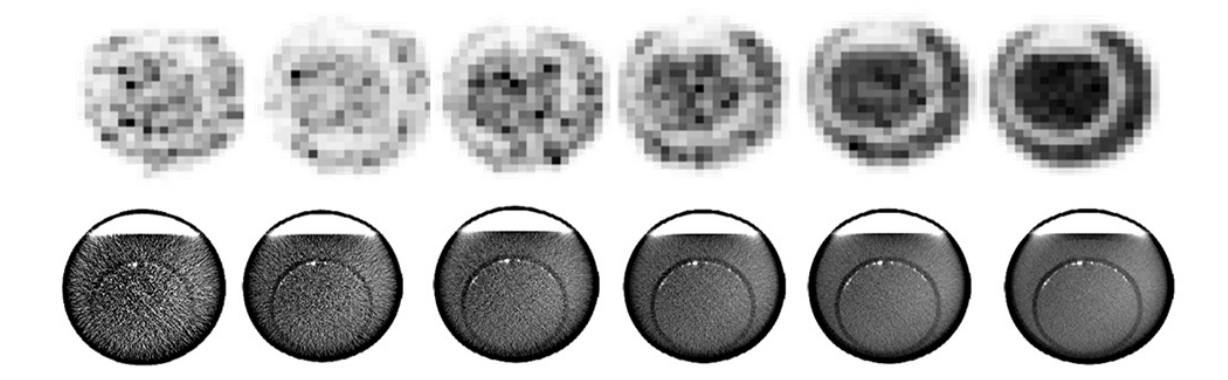


Figure 3–3: Transverse slices of phantom PET scan for scan times of 4, 6, 9, 15, 62, and 246 seconds (from left to right in the top row). Slices of the phantom taken with the CBCT are shown in the bottom row with increasing SNR from left to right

mean and standard deviation of the intensity values found in the inner jar wall and using the inner region of water as the background. Transverse slices from these 6 scans are shown in figure 3–3

$$SNR = 20 \cdot log_{10} \left(\frac{\mu_{sig}}{\sigma_{bkg}} \right) \tag{3.17}$$

Similarly the phantom was scanned using on-board cone beam computed to-mography (CBCT). The images were all scanned using a voltage of 100 kV but with varying current and pulse width. CBCT scans were evaluated due to their poor contrast and low SNR. The applied scanning parameters along with the resulting SNRs are summarized in table 3–1.

Approximately 310 ml of Omnipaque 300 (65% iohexol, GE Healthcare Canada, Mississauga ON) was diluted in 640 ml of water for the CBCT scan and the bolus sheet removed. It was observed that the scan contained beam hardening artifacts and

Table 3–1: Scanning parameters for the CBCT.

| Scan | Current (mA) | Pulse Width (ms) | SNR (dB) |
|------|--------------|------------------|----------|
| 1 | 10 | 10 | 25.3 |
| 2 | 20 | 10 | 29.2 |
| 3 | 40 | 10 | 31.8 |
| 4 | 40 | 20 | 33.9 |
| 5 | 80 | 20 | 35.3 |
| 6 | 80 | 32 | 35.7 |

an asymmetric distribution of contrast agent. In order to correct for these heterogeneities, the regions of the phantom walls and the space in between were delineated with circles matching the dimensions of the phantom. A quasi-ideal version of the phantom was generated by uniformly filling these areas with the mean value found in the original scan. A third volume was generated using the voxel-by-voxel ratio of the quasi-ideal phantom to the original scan. This third volume was smoothed using a 3D bilateral filter and then used to rescale the phantom images to remove the inhomogeneity. This is shown in figure 3-4. In order to compare the performance of the Jensen Rényi divergence versus using mutual information, two segmentation methods using an active contour but each driven by one of the two divergence measures was used to segment the region surrounded by the inner jar. Additionally a region growing algorithm were also used to segment the inner jar for comparison. The region growing algorithm was given an intensity difference threshold of half the intensity difference between the water and jar wall values. This was found to produce favourable results in the highest SNR images for both modalities. This was done two-dimensionally over 19 slices from each volume for both PET and CBCT modalities. The performance of each method was measured by the average concordance index comparing the final segmentation to the known boundary of the inner jar.

3.3.3 Clinical Studies

Louvain Database

In addition to phantom studies, we included clinical validation datasets with a known reference from previous studies so that our results could easily be compared to other results reported in the literature [3]. PET scans of a subset of 7 patients with T-III to T-IV pharyngolaryngeal squamous cell carcinoma taken from the Louvain database were used for performance evaluation [115]. Patients were imaged on average 5 days prior to treatment which entailed a total laryngectomy. A 60 min dynamic 3-D PET scan using an injection of 185-370 MBq of ¹⁸F-FDG was performed on the selected patients while immobilized with a thermoplastic mask. This was done with an ECAT EXACT HR camera (CTI Siemens, Knoxville, TN) and reconstructed using a 3-D Attenuation-weighted Ordered Subsets Expectation Minimization (AW-OSEM) algorithm into images of 128x128 voxels at a resolution of 2.1656 x 2.1656 mm in the transverse plane with a slice thickness of 3.125 mm. Following the laryngectomy, resected tissue was placed in a polystyrene cast that was filled with a 16% gelatin solution and cooled to -20°C for 48 hours and -80°C for a minimum of 72 hours. Specimens were cut transversely into 1.7-2 mm slices that were then digitally scanned on both faces using a flatbed scanner. A reference segment of the perceived gross tumor volume (GTV) was manually delineated using the digital scans of the macroscopic specimens and coregistered to the PET volume

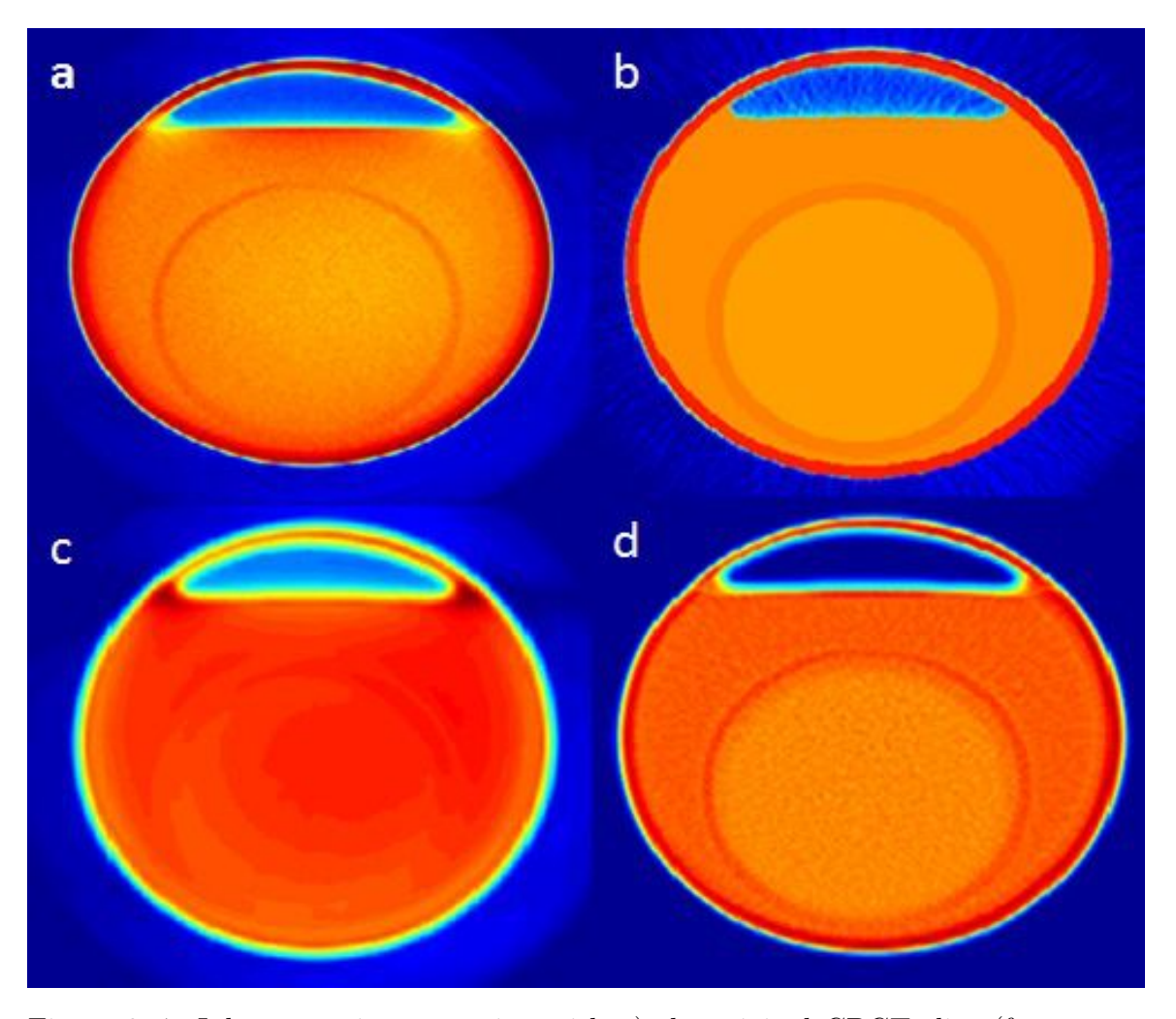


Figure 3–4: Inhomogeneity correction with a) the original CBCT slice (from scan #6). b)The ideal phantom whose values are equal to the mean within the 4 regions found in a). c) The ratio of b) to a) following a bilateral filter smoothing, using $\sigma_1 = 13$, $\sigma_2 = 18$ and a tolerance of 0.02, and finally d) the corrected image.

using a semi-automated rigid transformation using segmented structures as described by Daisne et al. [116].

The PET images were segmented following a denoising procedure which consisted of smoothing using a bilateral 3D filter followed by deconvolution using the Landweber algorithm. For the JRD algorithm, segments were initialized using an anisotropic sphere that approximated the size of the GTV and ran for 100 iterations. The following parameters were used in all studies when evaluating the algorithm for the JRD (v = 0.013, $\alpha = 1.8$, $\mu = 0.1$).

MAASTRO Database

In order to evaluate the performance with regard to multimodal data, this study included a set of 33 patients with stage Ib-IIIb non-small cell lung carcinoma (NSCLC) treated at the Maastro clinic in Maastricht, The Netherlands. Each has received a whole-body PET/CT scan using a Biograph SOMATOM Sensation 16 with an ECAT ACCEL PET scanner (Siemens, Erlangen Germany). Patients were injected with an ¹⁸F-FDG tracer following a 6 hour fast. The dosage was determined using (weight×4 + 20 MBq). A spiral CT with contrast was performed. The patient was then scanned in 5 min intervals covering 7 sections, beginning 45 minutes post-injection. The CT scan was used for attenuation correction and the PET data reconstructed using OSEM with 8 subsets and 4 iterations. Of these 33 patients, 22 of which underwent surgical resection of the lung tumor, the maximal diameters of the tumor were measured macroscopically. This was used for comparison against the maximal tumor diameters produced by the JRD segmentation algorithm. The data collection is discussed in more detail in Van Baardwijk et al., [89].

Validation Metrics

With regards to the Louvain dataset, contours drawn from the images of the macroscopic specimens were used as a reference and validation was determined by two frequently used similarity metrics; concordance index (CI) and classification error (CE):

$$CI = \frac{A \cap B}{A \cup B} \tag{3.18}$$

$$CE = \frac{PCE + NCE}{Vol} \times 100\% \tag{3.19}$$

Here positive CEs (PCE) is the volume identified as background that is actually part of the tumor and negative CEs (NCE) is the volume identified as tumor that is actually background. *Vol* is the volume of the histologically derived contours. When defining CI, A and B are defined as the segmented volume and macroscopically derived volume, respectively.

The MAASTRO data was evaluated using the percent error of the maximal tumor diameter defined by equation 3.20:

$$\%error = \frac{|maxD_{seg} - maxD_{macro}|}{maxD_{macro}}$$
(3.20)

This was done due to the fact that the binary tumor masks were unavailable, only maximal tumor diameter was used in the original study.

Hardware and Implementation

The JRD based level sets method was implemented in Matlab on a laptop with an Intel Core i7-2630QM @2GHz using 16GB of RAM and an NVIDIA GEFORCE GTX 560M with 3 GB of integrated RAM. Each iteration was calculated on the GPU requiring 0.2-0.4 seconds per iteration using a single modality and 0.4-0.6 seconds per iteration when using two modalities.

3.4 Results

3.4.1 Phantom Studies

Using a slice from each scan that showed the inner jar wall surrounded by the outer jar, binary masks of circles of radii varying from 29 to 36 mm were used to measure the mutual information and Jensen Rényi divergence. Figures 3–5 and 3–6 show the mutual information and Jensen Rényi divergence for the different radii using the CBCT and PET scans. The minima for both functions occurs at the wall of the inner jar. The profiles for both divergences are shown for the lowest SNR scan and the highest. The profiles show a distinct difference between the two scans, the minima of the mutual information becomes severely distorted by the decrease in image SNR. This is reflected in the performance of the two algorithms when measured using the average concordance index as shown in figures 3–8 and 3–9 when applied to the CBCT and PET modalities, respectively. The region growing method showed a drastic decrease in performance for both modalities as noise in the image increase. Profiles of the JRD are affected by the choice of alpha value as shown in figure 3–7. Higher alpha values produce a sharper curve upon approaching the inner jar wall. The tail of the profiles are also increased with increasing alpha, these tails exist due

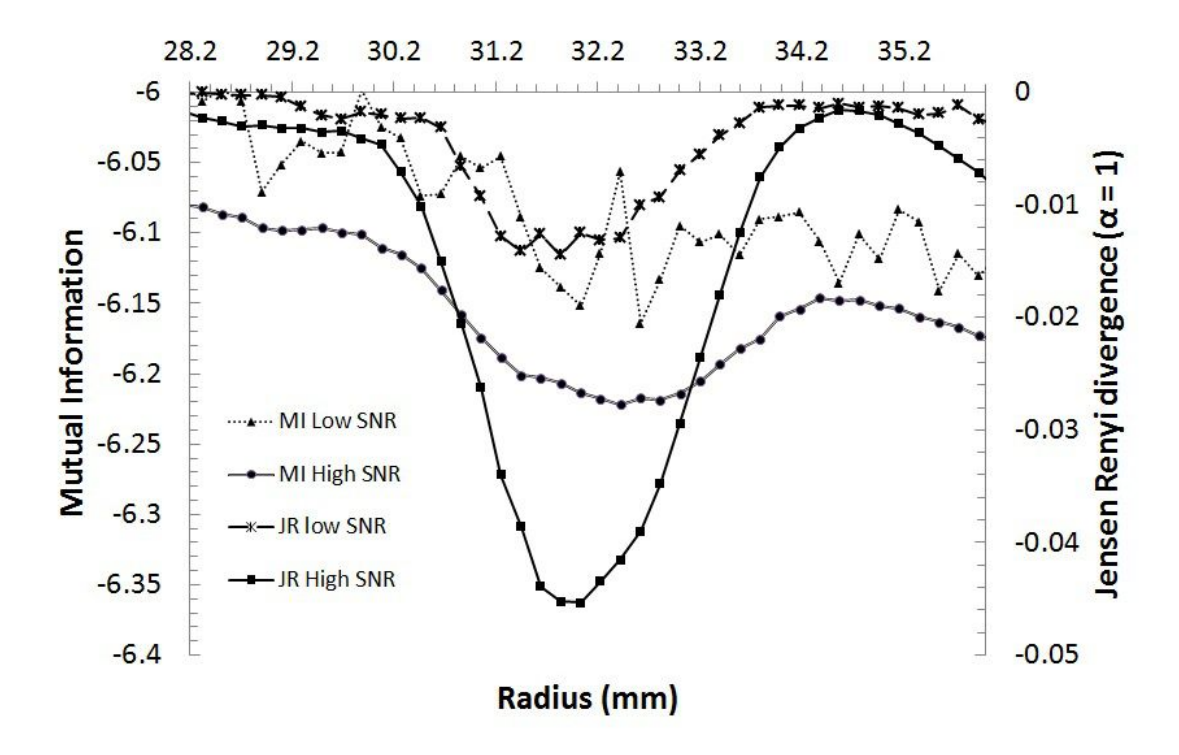


Figure 3–5: JRD and mutual information measured for circles of growing radius centered at the inner jar using the CBCT images. The low SNR scan had an SNR value of 32 and the high SNR scan had a value of 36. The peak is clearly preserved using the JRD when applied to the lower SNR image set.

to detection of the outer wall which lies partially adjacent to the bottom of the inner wall as shown in figure 3–4.

3.4.2 Clinical PET Evaluation: Louvain Database

The results from segmenting the PET images from the Louvain dataset are compared against those presented by Zaidi et al. [3], where a comparison of 9 algorithms is performed. The results are shown in terms of Classification error and concordance index in figures 3–10 and 3–11. The JRD algorithm showed an average concordance

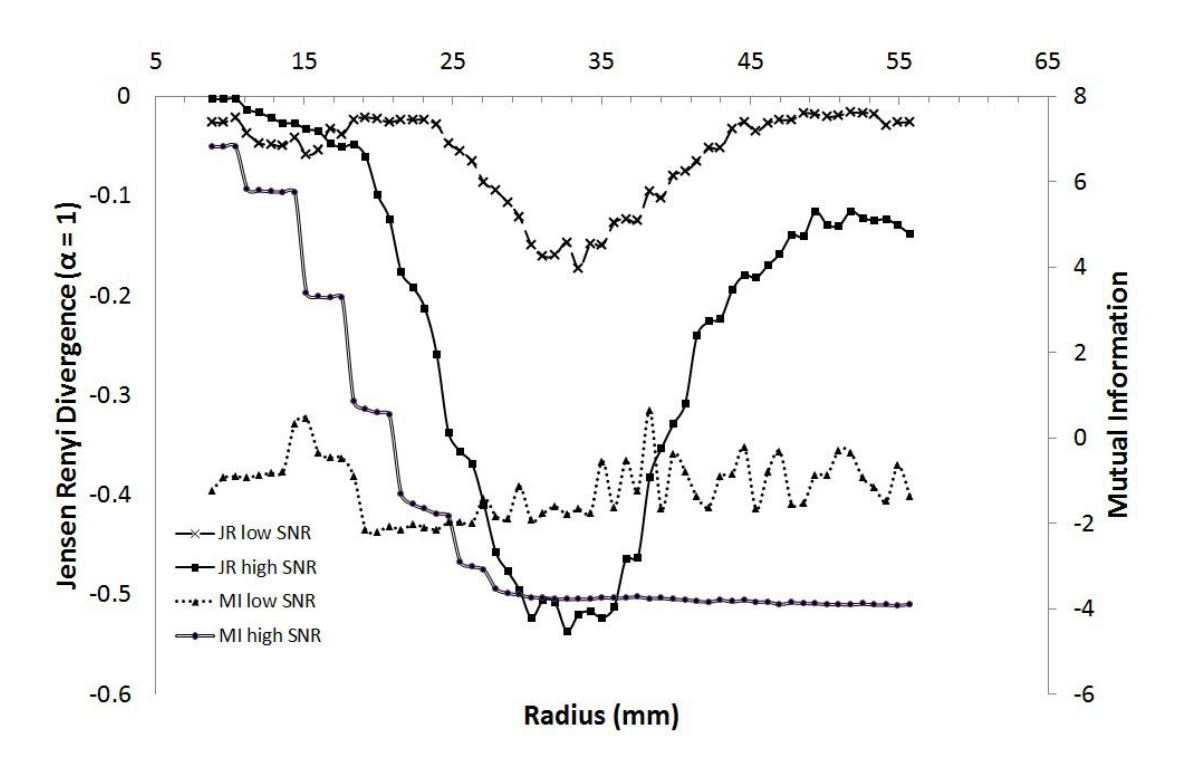


Figure 3–6: JRD and mutual information measured for circles of growing radius centered at the inner jar using the PET images. The low SNR scan had an SNR value of 9.2 and the high SNR scan had a value of 26.

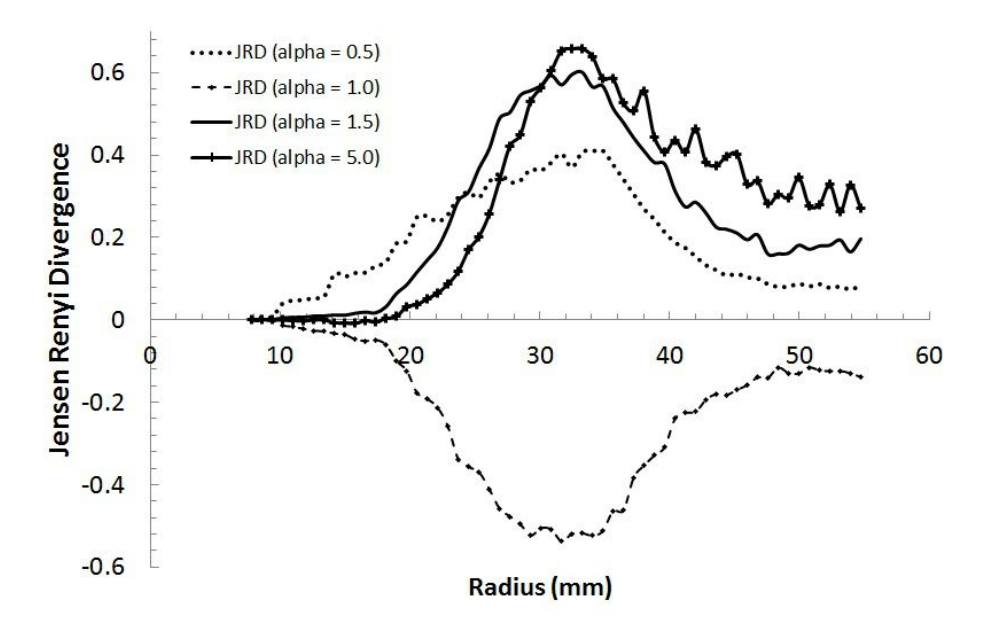


Figure 3–7: The Jensen Rényi divergence measured for the PET scan of the noise phantom with circles of increasing radii. The profiles are shown with varying choices of parameter α . When α is equal to 1, the values become negative since the Rényi entropy reduces to the Shannon entropy as shown in equation 3.8.

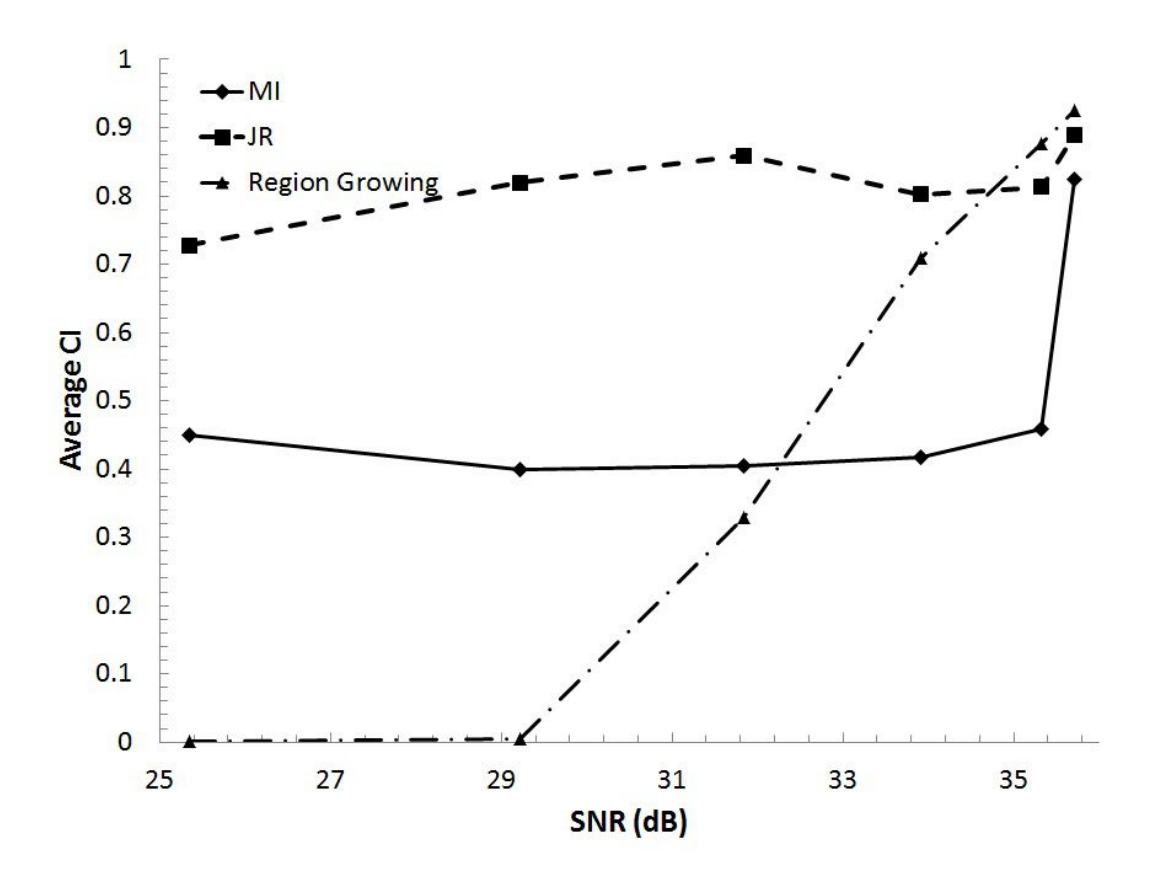


Figure 3–8: The average concordance index of the active contour based on mutual information and the Jensen Rényi divergence for varying CBCT SNR values. The JRD shows a linear response to noise whereas the mutual information shows a somewhat exponential decrease in performance.

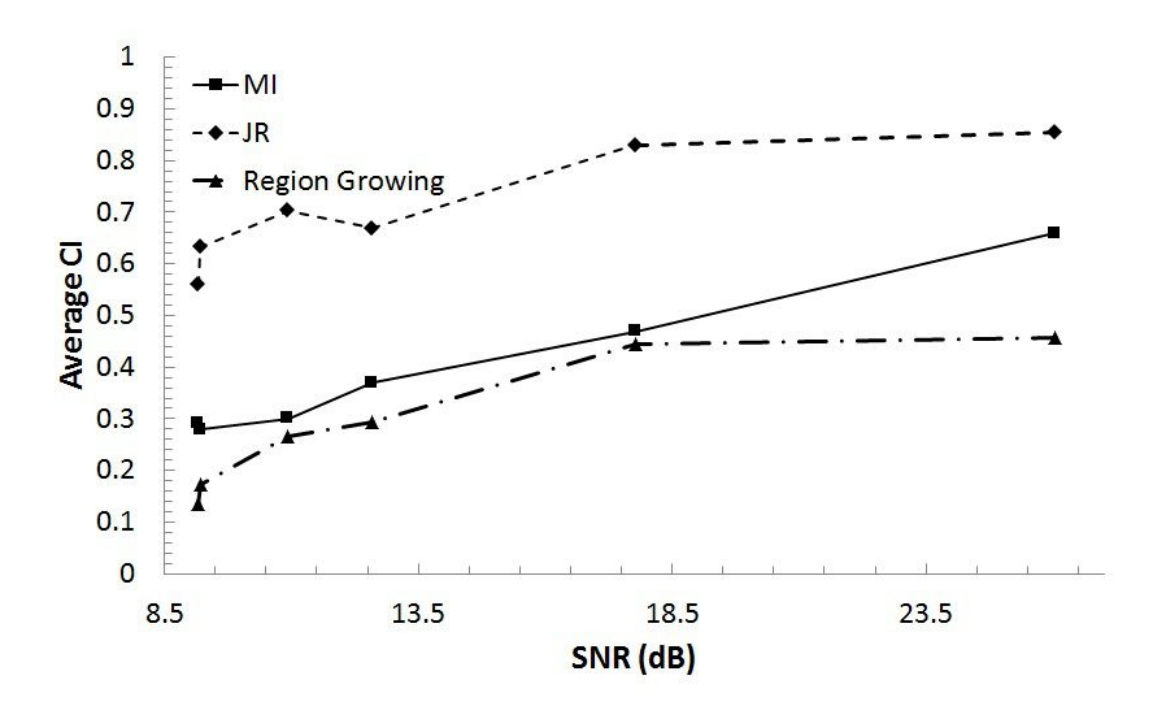


Figure 3–9: The average concordance index of the active contour based on mutual information and the Jensern Rényi divergence for varying PET SNR values, controlled by the scan time.

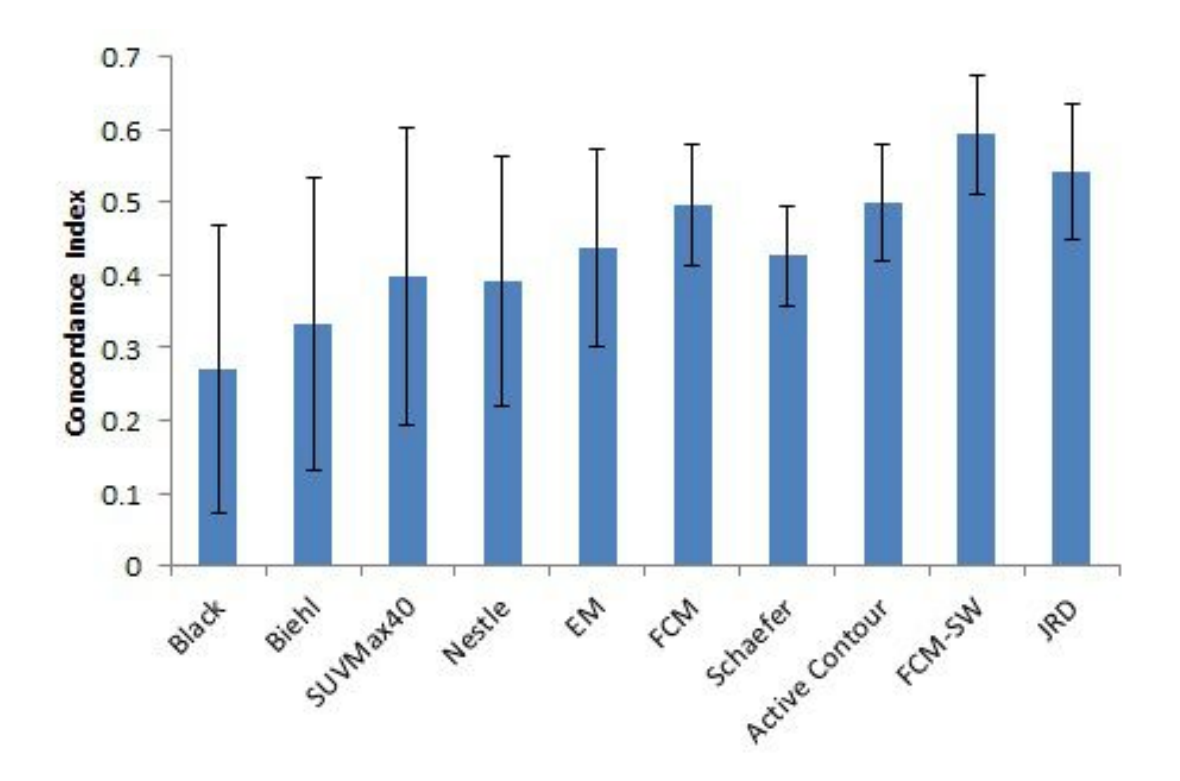


Figure 3–10: The average concordance index of the JRD based active contour compared to 9 other PET segmentation algorithms evaluated using the same data from Zaidi et al. [3]. Using only the PET intensity, the JRD based segmentation had an average CI of 0.55 versus 0.59 for the FCM-SW. The error bars represent one standard deviation.

index of 0.55 with a standard deviation of 0.12. This was second to the fuzzy clustering method incorporating spatial information and the á trous wavelet transform (FCM-SW) which has a average CI of 0.59 with a somewhat smaller standard deviation of 0.08. Similar results are reflected with regards to the average classification error where the JRD method had an average CE of 65% second to 55% for the FCM-SW.

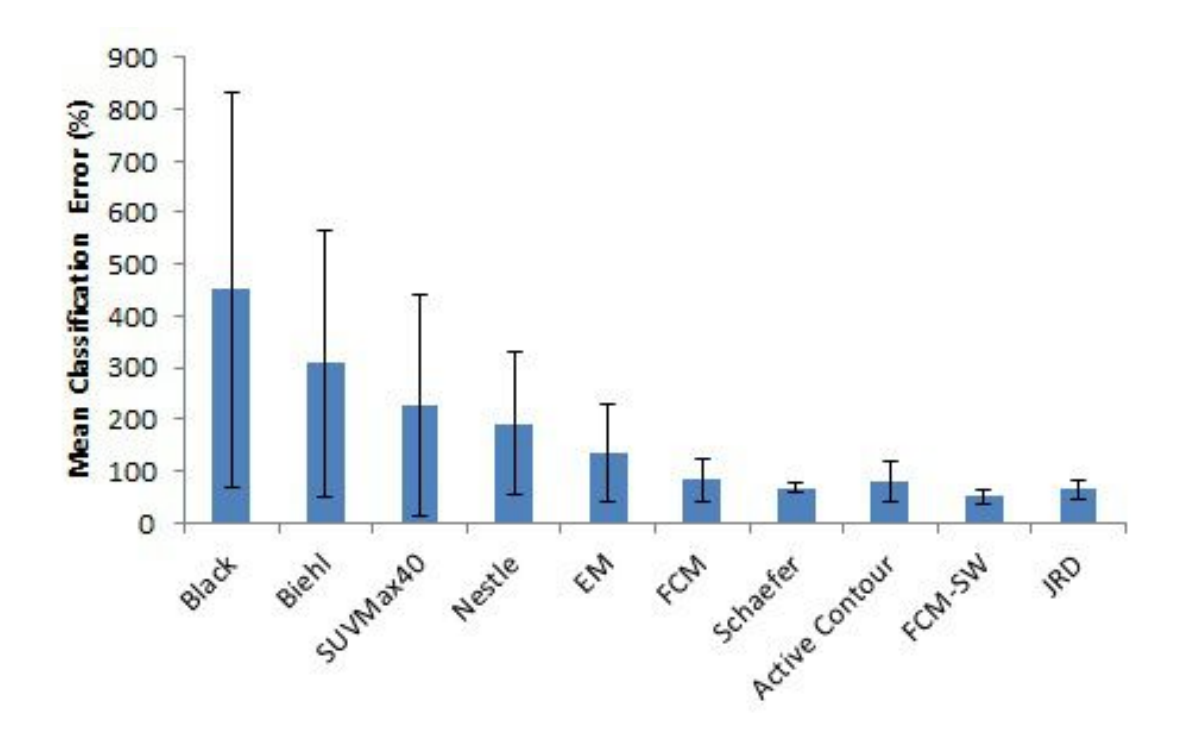


Figure 3–11: The average classification error of the JRD based active contour compared to 9 other PET segmentation algorithms evaluated using the same data from Zaidi et al. [3]. The JRD based segmentation had an average CE of 65% versus 50% for the FCM-SW. The error bars represent one standard deviation.

3.4.3 Clinical PET/CT Evaluation: MAASTRO Database

Figure 3–12 shows the percentage error of the maximum GTV diameter estimation for the JRD-based active contour when using PET, CT and PET-CT together. The error is shown for each patient and shows a general trend of having the highest error when using CT alone and the lowest when using both modalities in conjunction. The correlation between maximal diameter estimate by the SBR method published by Baardwijk et al. in 2007 [89] showed an R² value of 0.82. The same comparison using the results from the JRD based method using the PET image alone is shown in Figure 3–13 and using the PET-CT together in Figure 3–14. The estimated maximum diameter by the JRD method shows a higher correlation with the macroscopically determined diameter than the SBR technique when using only PET. This correlation is further improved when using the PET and CT information together which is not surprising considering the results shown in figure 3–12.

3.5 Discussion

Hybrid imaging is becoming increasingly prevalent within radiotherapy clinics with the commercial introduction of PET/CT scanners over 15 years ago and more recently with the advent of PET/MRI scanners. Consequently, radiation oncologists are required to consider multiple pieces of visual information when determining treatment targets yet the large majority of commercially available automated and semi-automated segmentation algorithms do not consider more than one modality at a time. Presented in this work is a novel multimodality segmentation algorithm based on the level set active contour method that relies on maximizing the Jensen

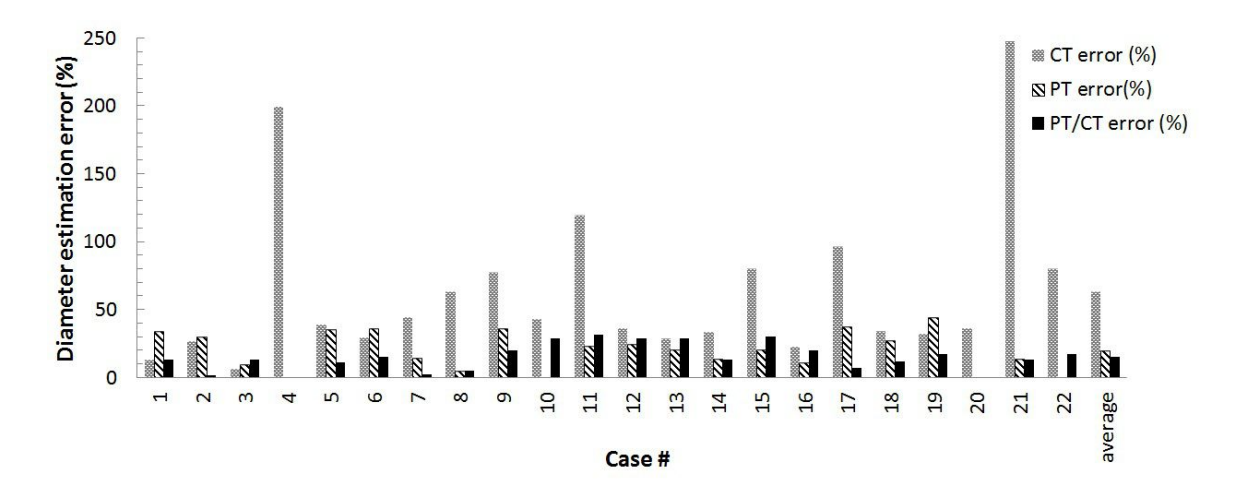


Figure 3–12: The estimation error for the JRD based segmentation method of the GTV compared to the macroscopically determined maximum diameter. The average error was 63%, 19.5% and 14.8% for the segmentations using CT only, PET only and PET/CT. Particularly, high errors for cases 4 and 21 were seen when using CT alone due to the small size of the lesions and their proximity to the chest wall causing contour leakage.

Rényi divergence between the inside and outside domain of the contour. The advantage of using this divergence measure is two-fold. The first is that when compared to mutual information, the JRD offers an improved robustness to sample variability and hence image noise. This is demonstrated using the phantom scans where not only is the difference in the energy space seen between the two measures, but the effect that this has on the performance for both PET and CT images is demonstrated in figures 3–8 and 3–9. The second advantage is that changing the alpha value can alter the energy space of the function and thus its tolerance to noise and the sensitivity of the final solution to subtle changes in intensity distribution.

The algorithm was tested using clinical single and multiple image modalities when performing segmentations. Considering the improved noise tolerance of the

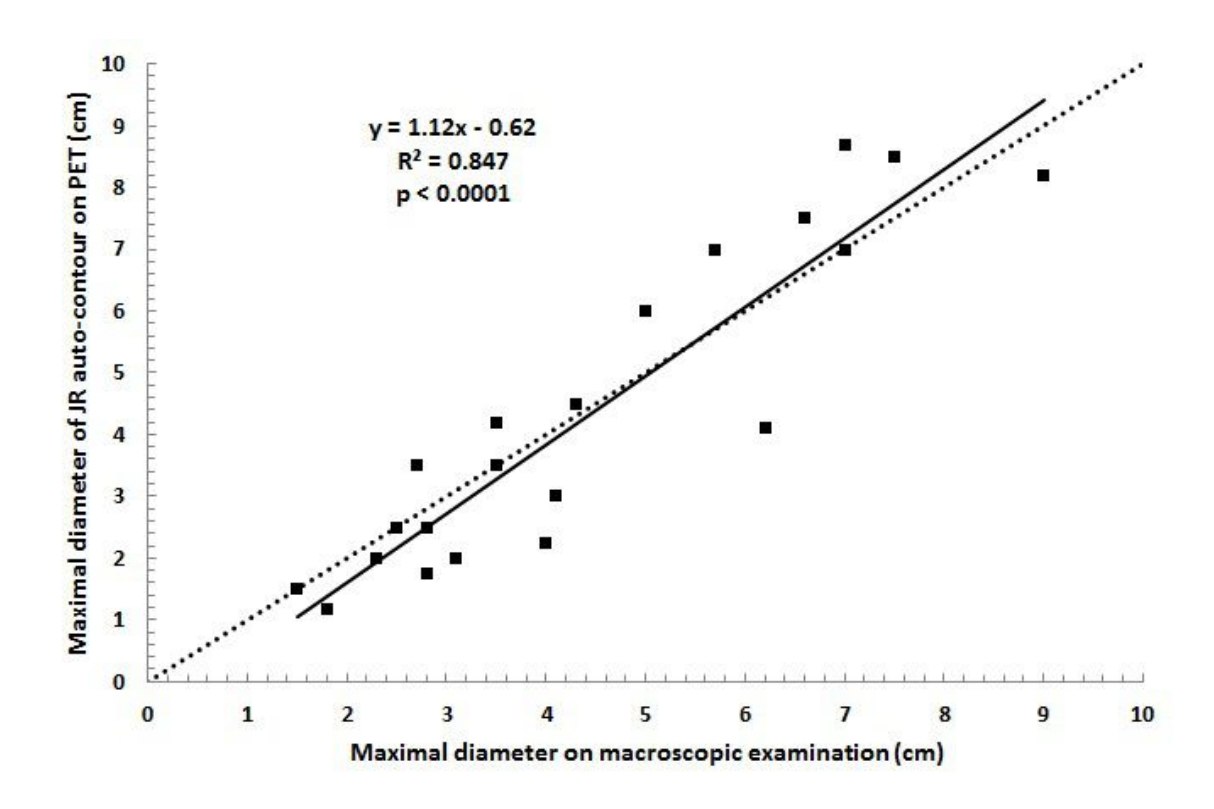


Figure 3–13: The correlation of the JRD estimated maximum diameters versus the macroscopically determined maximum GTV diameters using only the PET image. The solid line shows the linear fit to the data while the dotted line represents the ideal 1 to 1 linear relationship. The JRD based method shows a higher correlation compared to the SBR technique with an \mathbb{R}^2 value of 0.85 versus 0.82.

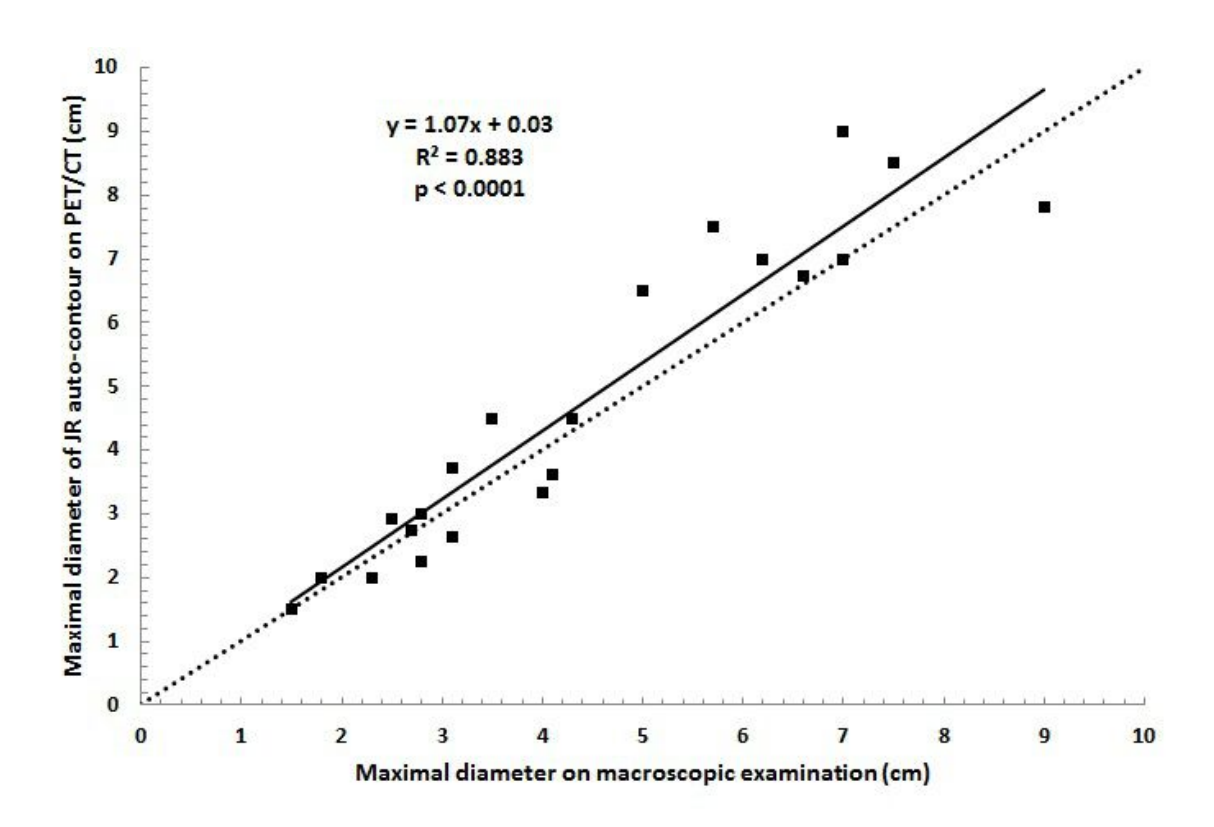


Figure 3–14: The correlation of the JRD estimated maximum diameters versus the macroscopically determined maximum GTV diameters using both the PET and CT. The incorporation of both modalities shows an improved correlation versus using PET alone.

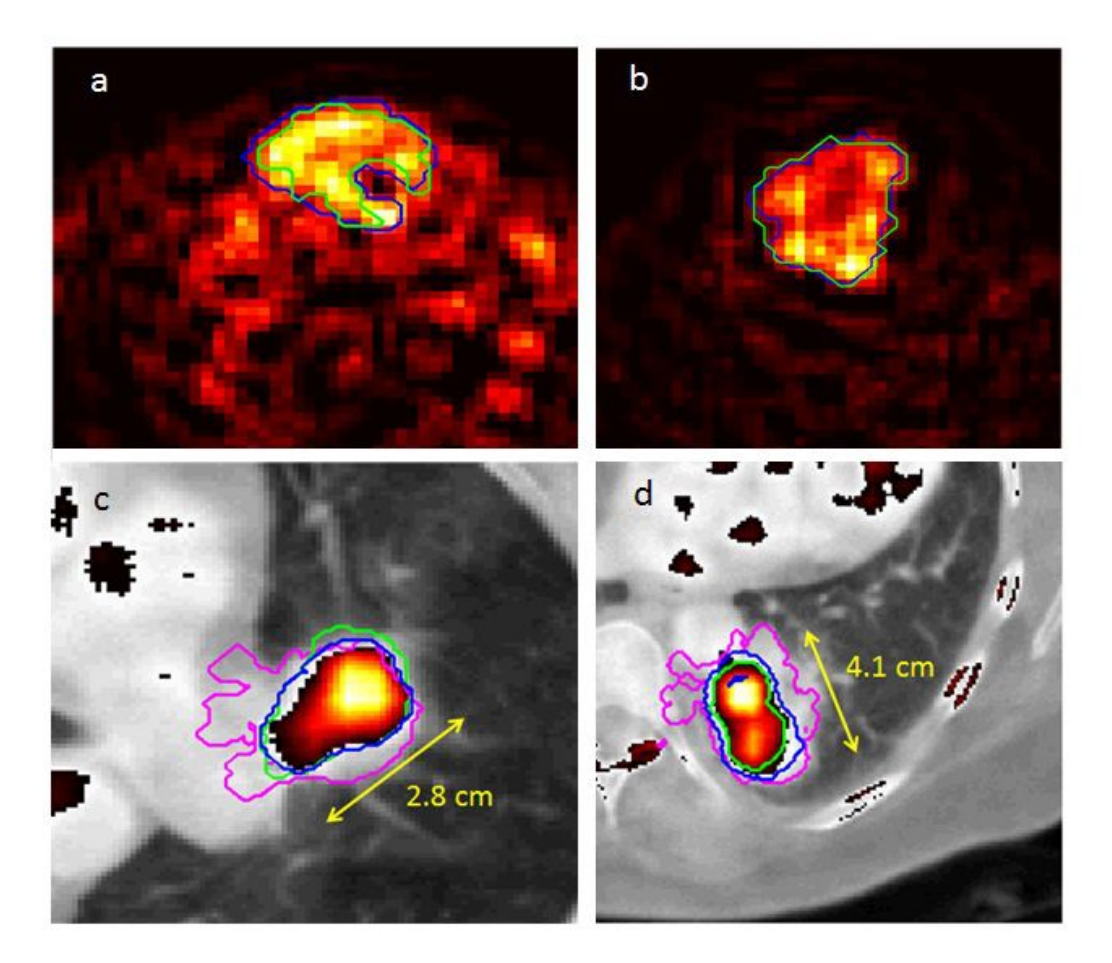


Figure 3–15: A comparison of the JRD method applied to the Louvain (a and b) and MAASTRO (c and d) datasets with their respective references. In a and b, the JRD method is shown in blue compared to the macroscopically determined contour in green. For c and d, the JRD method using the CT only is drawn in magenta, using PET only in green and using combined PET and CT together in blue. It is compared to the maximum diameter shown with the yellow arrow.

JRD and the fact that PET is a modality presenting with a large degree of inherent noise, it was appropriate to compare the segmentation method using PET alone versus other PET segmentation methods. This was done using the results from Zaidi et al. [3] that used data from the Louvain database. The JRD based method did not perform as well as the FCM-SW in regards to both average classification error and average concordance index (figures 3–10 and 3–11) however this difference was not found to be statistically significant (p = 0.52 for CI and p = 0.16 for CE). It should also be noted that the FCM-SW algorithm utilizes both an anisotropic diffusion filter as well as the á trous wavelet transform as additional pre-processing steps whereas the results for the JRD method as implemented incorporated only the PET intensity values. It may be possible to improve the JRD segmentation results by using the filters adopted by the the FCM-SW algorithm since the JRD method can incorporate multiple inputs.

The MAASTRO data shows that the JRD method can estimate maximum GTV diameter with a better correlation to the macroscopically determined diameters than using the SBR method which relies on fitting the most appropriate threshold to the lesion volume. The segmentation results show that using the PET information results in a higher accuracy than using the CT alone. This result has been observed previously [106, 9] and can be qualitatively seen on the contours shown in figure 3–15 (c and d), where the CT contours had little contrast to follow when the GTV was connected to the mediastinum or chest wall. This led to leaking and overestimation of the boundary which was the reason for the large errors seen for cases 4, 11 and 21 in the MAASTRO data shown in figure 3–12. By comparing the trends shown in

figures 3–13 and 3–14 we see an increase in the adherence to a linear fit from the R-square value but also closer 1:1 linear relationship between the estimated maximum diameters using both PET and CT than with PET alone. This is seen from the slope of the trend lines. The combination of both PET and CT provides the most accurate segmentation, and the highest correlation to the reference, a result that has been previously observed [106]. Results from a 2011 study using the FCM-SW algorithm[95] to estimate maximum tumor diameter using the MAASTRO dataset showed an R-square value of 0.942, much higher than using the JRD with either PET or PET/CT. The R-squared value of the FCM-S algorithm evaluated in the same study was only 0.81 emphasizing again the improvement made by including the á trous wavelet transform.

The JRD is a convenient objective function in that it can also be applied to the task of registration as investigated by a number of reports [109, 73, 117]. This may facilitate future work involving the simultaneous segmentation and registration of multimodality images using this metric in order to reduce computation time and improve accuracy of both processes. Such an algorithm would have great application towards IGART where previous plan contours provide a good approximation for initialization.

3.6 Conclusions

This work has presented a novel multimodality segmentation algorithm using the Jensen-Rényi divergence with a level set contour. Using phantom CBCT and PET scans taken at various image quality levels, we demonstrate the improved noise robustness of the proposed objective compared to a traditional information-theoretic similarity measure (mutual information). The solution to the level set differential equation is presented along with clinical data validation using PET scans of 7 patients from the Louvain database with pharyngolaryngeal squamous cell carcinoma and 22 PET/CT scans from patients with lung carcinoma taken from the MAASTRO database. The JRD based approach has shown competitive performance compared to existing methods without much added pre- and post-processing. More importantly, the approach allows for easy application to simultaneous multimodality segmentation as demonstrated in the phantom and clinical results.

3.7 Acknowledgements

We would like to acknowledge Greg Twork for his assistance in collecting the CBCT data and John Kildea for assisting with data collection. We also thank Dr Dekker and Dr De Ruysscher (MAASTRO clinic, Maastricht, The Netherlands) and Dr Lee (Université Catholique de Louvain, Brussels, Belgium) for providing the clinical PET datasets. Funding was provided by the Natural Sciences and Engineering Research Council of Canada (NSERC-RGPIN 397711-11) and the Research Institute of the McGill University Health Centre. Dr Zaidi is also supported by the Swiss National Science Foundation under grant SNSF 31003A-135576 and Geneva Cancer League.

3.8 Conflict of Interest

The authors of this paper have no direct financial connection to the any commercial identities mentioned in the article and no competing interests to disclose.

3.9 Appendix

The integrals of equation 3.11 can be simplified using the following property of convolution theory regarding the integral of two Gaussian functions.

$$\int g_p(x;a,A)g_p(x;b,B)dx$$

$$= \int \frac{1}{(2\pi)^{p/2}|A|^{1/2}} e^{-\frac{1}{2}(x-a)'A^{-1}(x-a)} \frac{1}{(2\pi)^{p/2}|B|^{1/2}} e^{-\frac{1}{2}(x-b)'B^{-1}(x-b)} dx$$

$$= \frac{1}{(2\pi)^{p/2}|A+B|^{1/2}} e^{-\frac{1}{2}(a-b)'(A+B)^{-1}(a-b)}$$
(3.21)

Where a and b are offsets, or other data points in the distribution if we are referring to how we will apply this. A and B are the covariance matrices of their respective Gaussian probability functions (G_p) . If one chooses an alpha value of 2, this conveniently allows us to take advantage of this property, for example if we can define

$$P_{12} = P_{21} =$$

$$\int_{\Re} P_1(J,\Omega_-) P_2(J,\Omega_+) dJ =$$

$$\frac{1}{n_1 n_2} \sum_{i=1}^{n_1} \sum_{j=1}^{n_2} \int_{\Re} K_{\psi_1} \left(J - J(x_i) \right) \times K_{\psi_2} \left(J - J(x_j) \right) dJ \tag{3.22}$$

$$= \frac{1}{n_1 n_2} \sum_{i=1}^{n_1} \sum_{j=1}^{n_2} (2\pi)^{-p/2} |\psi_1 + \psi_2|^{-1/2} \times$$

$$exp\left(-\frac{1}{2}\left(J(x_i) - J(x_j)\right)^T \left[\psi_1 + \psi_2\right]^{-1} \left(J(x_i) - J(x_j)\right)\right)$$

and similarly

$$P_{11} = \frac{1}{n_1 n_1} \sum_{i=1}^{n_1} \sum_{i'=1}^{n_1} K_{2\psi_1} \left(J(x_i) - J(x_{i'}) \right)$$
 (3.23)

We can also define

$$\hat{P}_{12}(J,\Omega) = \int_{\Re} P_1(J,\Omega) K_{\psi_2}(J(C) - J) dJ$$

$$= \frac{1}{n_1} \sum_{i=1}^{n_1} (2\pi)^{-p/2} |\psi_1 + \psi_2|^{-1/2} \times$$
(3.24)

$$exp\left(-\frac{1}{2}(J(x_i)-J(C))^T [\psi_1+\psi_2]^{-1}(J(x_i)-J(C))\right)$$

and using these definitions we can rewrite equation 3.11 as

$$\partial \phi(x)/\partial C =$$

$$-\frac{2w_1^2(\hat{P}_{12}-P_{11})+2w_1w_2(P_{12}-\hat{P}_{12}+\hat{P}_{21}-P_{21})+2w_2^2(P_{22}-\hat{P}_{22})}{(w_1^2P_{11}+w_2w_2(P_{12}+P_{21})+w_2^2P_{22})}+\frac{2w_1(\hat{P}_{11}-P_{11})}{P_{11}}+\frac{2w_2(P_{22}-\hat{P}_{22})}{P_{22}}$$
(3.25)

This simplification means the processing time of the algorithm increases as $O(pn^{\alpha})$ where p is the number of input images and n is the number of samples used to estimate P_1 and P_2 . This is opposed to an increase of $O(n^p)$ which allows the consideration of a larger number of image features/modalities when segmenting. In the general case that alpha is an integer greater than 2, the property of equation 3.22 can be applied recursively, for example in the case of the integral of the product of n Gaussian functions

$$\left(\prod_{i=1}^{n} \sum_{k=1}^{s}\right) \int_{\Re} \prod_{i=1}^{n} \frac{1}{|\Omega_{i}|} K_{\sigma_{i}} \left(J - J(x_{k^{i}})\right) \\
= \left(\prod_{i=1}^{n} \sum_{k=1}^{s}\right) \frac{1}{(2\pi)^{p/2} \left(\prod_{i=1}^{n} |\psi_{i}|^{1/2}\right) \left|\left(\sum_{i=1}^{n} \psi_{i}^{-1}\right)\right|^{1/2}} \times exp\left(-\frac{1}{2} \sum_{i=1}^{n-1} (d_{i} - x_{k^{i}})^{T} D_{i} (d_{i} - J(x_{k^{i}}))\right) \\
where D_{i} = \left(\sum_{j=1}^{i+1} \psi_{k^{j}}^{-1}\right)^{-1} \text{ and } d_{i} = \frac{\sum_{j=1}^{i} \psi_{j} x_{k^{j}}}{\sum_{j=1}^{i} \psi_{j}}, \tag{3.26}$$

where s is the total number of samples taken from inside and outside the segment and k^i is the k^{th} sample of the i^{th} summation. To similarly reduce the number of integrals let us define the following terms

$$\check{P}_{11} = \alpha \int_{\Re} \left(w_1 P_1 \left(J, \Omega_- \right) + w_2 P_2 \left(J, \Omega_+ \right) \right)^{\alpha - 1} \times \left(w_1 \left(k_{\sigma_1} \left(J(C) - J \right) \right) \right) dJ$$

$$= \alpha \int_{\Re} \sum_{l=0}^{\alpha-1} {\alpha-1 \choose l} (w_1 P_1(J, \Omega_-))^{\alpha-1-l} \times (w_2 P_2(J, \Omega_+))^l w_1(k_{\sigma_1}(J(C) - J)) dJ$$

$$= \alpha \sum_{l=0}^{\alpha-1} {\alpha-1 \choose l} \hat{\beta}_{11} w_1^{\alpha-l} w_2^l \frac{1}{(2\pi)^{p/2} (|\psi_1|^{\alpha-l} |\psi_2|^l |((\alpha-l)\psi_1^{-1} + l\psi_2^{-1})|)^{1/2}} exp \left(-\frac{1}{2} \sum_{j=1}^{\alpha} (d_j - x_{k^j})^T D_j (d_j - x_{k^j}) \right)$$

where
$$x_{k^j} \in \Omega_-$$
 for $j = 1, 2...\alpha - l$
 $\mathbf{x}_{k^j} \in \Omega_+$ for $j = \alpha - l + 1, ...\alpha - 1$
 $\mathbf{x}_{k^j} = J(C)$ iff $j = \alpha$

and
$$\hat{\beta}_{11} = \frac{1}{n_1^{\alpha-l}} \left(\sum_{k^0=1}^{n_1} \sum_{k^1=1}^{n_1} \dots \sum_{k^{\alpha-l}=1}^{n_1} \right) \times \frac{1}{n_2^l} \left(\sum_{k^{0'}=1}^{n_2} \sum_{k^{1'}=1}^{n_2} \dots \sum_{k^{l'}=1}^{n_2} \right)$$
(3.27)

$$\overline{P}_{11} = \alpha \int_{\Re} \left(\sum_{l=0}^{\alpha-1} {\alpha-1 \choose l} \right) \left(w_1 P_1 \left(J, \Omega_- \right) \right)^{\alpha-l} \left(w_2 P_2 \left(J, \Omega_+ \right) \right)^l dJ$$

$$= -\alpha \sum_{l=0}^{\alpha-1} \binom{\alpha-1}{l} \beta_{11} w_1^{\alpha-l} w_2^l \frac{1}{(2\pi)^{p/2} \left(|\psi_1|^{\alpha-l} |\psi_2|^l \left| \left((\alpha-l) \psi_1^{-1} + l \psi_2^{-1} \right) \right| \right)^{1/2}} \times \\$$

$$exp\left(-\frac{1}{2}\sum_{j=1}^{\alpha}(d_j - x_{k^j})^T D_j(d_j - x_{k^j})\right)$$
(3.28)

where
$$x_{k^j} \in \Omega_- for j = 1, 2...\alpha - l + 1$$

 $\mathbf{x}_{k^j} \in \Omega_+ \text{ for } j = \alpha - l + 2, ...\alpha$

and
$$\beta_{11} = \frac{1}{n_1^{\alpha - l + 1}} \left(\sum_{k^0 = 1}^{n_1} \sum_{k^1 = 1}^{n_1} \dots \sum_{k^{\alpha - l + 1} = 1}^{n_1} \right) \times \frac{1}{n_2^l} \left(\sum_{k^{0'} = 1}^{n_2} \sum_{k^{1'} = 1}^{n_2} \dots \sum_{k^{l'} = 1}^{n_2} \right)$$

Here the summations with a k^n and $k^{n'}$ refer to summations of the sample sets from inside and outside the segment. For completeness,

$$\check{P}_{22} = \alpha \int_{\Re} \left(w_1 P_1 \left(J, \Omega_- \right) + w_2 P_2 \left(J, \Omega_+ \right) \right)^{\alpha - 1} w_2 k_{\sigma_2} \left(J(C) - J \right) dJ$$

$$= \alpha \int_{\Re} \sum_{l=0}^{\alpha-1} {\alpha-1 \choose l} (w_1 P_1(J, \Omega_-))^{\alpha-1-l} \times (w_2 P_2(J, \Omega_+))^l w_2(k_{\sigma_2}(J(C) - J)) dJ$$

$$=\alpha\sum_{l=0}^{\alpha-1}\binom{\alpha-1}{l}\hat{\beta}_{22}w_1^{\alpha-1-l}w_2^{l+1}\frac{1}{(2\pi)^{p/2}\left(|\psi_1|^{\alpha-1-l}|\psi_2|^{l+1}\left|\left((\alpha-1-l)\psi_1^{-1}+(l+1)\psi_2^{-1}\right)\right|\right)^{1/2}}\times$$

$$exp\left(-\frac{1}{2}\sum_{j=1}^{\alpha}(d_j - x_{k^j})^T D_j(d_j - x_{k^j})\right)$$

$$where \ \mathbf{x}_{k^j} \in \Omega_- \text{ for } j = 1, 2...\alpha - 1 - l$$

$$\mathbf{x}_{k^j} \in \Omega_+ \text{ for } j = \alpha - l, ...\alpha - 1$$

$$\mathbf{x}_{k^j} = J(C) \text{ iff } j = \alpha$$

and
$$\hat{\beta}_{22} = \frac{1}{n_1^{\alpha - 1 - l}} \left(\sum_{k^0 = 1}^{n_1} \sum_{k^1 = 1}^{n_1} \dots \sum_{k^{\alpha - l - 1} = 1}^{n_1} \right) \times \frac{1}{n_2^l} \left(\sum_{k^{0'} = 1}^{n_2} \sum_{k^{1'} = 1}^{n_2} \dots \sum_{k^{l'} = 1}^{n_2} \right)$$

$$(3.29)$$

$$\overline{P}_{22} = \alpha \int_{\Re} \left(\sum_{l=0}^{\alpha-1} {\alpha-1 \choose l} \right) \left(w_1 P_1 \left(J, \Omega_- \right) \right)^{\alpha-1-l} \left(w_2 P_2 \left(J, \Omega_+ \right) \right)^{l+1} dJ$$

$$= -\alpha \sum_{l=0}^{\alpha-1} {\binom{\alpha-1}{l}} \beta_{22} w_1^{\alpha-1-l} w_2^{l+1} \times$$

$$\frac{1}{(2\pi)^{p/2} \left(|\psi_1|^{\alpha-1-l} |\psi_2|^{l+1} \left| \left((\alpha-1-l)\psi_1^{-1} + (l+1)\psi_2^{-1} \right) \right| \right)^{1/2}} \times \\$$

(3.30)

 $exp\left(-\frac{1}{2}\sum_{j=1}^{\alpha}(d_{j}-x_{k^{j}})^{T}D_{j}(d_{j}-x_{k^{j}})\right)$

where
$$x_{k^j} \in \Omega_-$$
 for $j = 1, 2...\alpha - l$
 $\mathbf{x}_{k^j} \in \Omega_+$ for $j = \alpha - l + 1, ...\alpha$

and
$$\beta_{22} = \frac{1}{n_1^{\alpha - l}} \left(\sum_{k^0 = 1}^{n_1} \sum_{k^1 = 1}^{n_1} \dots \sum_{k^{\alpha - l} = 1}^{n_1} \right) \times \frac{1}{n_2^{l+1}} \left(\sum_{k^{0'} = 1}^{n_2} \sum_{k^{1'} = 1}^{n_2} \dots \sum_{k^{(l+1)'} = 1}^{n_2} \right)$$

$$\overline{P}_{312} = \int_{\Re} \left(w_1 P_1 \left(J, \Omega_- \right) + w_2 P_2 \left(J, \Omega_+ \right) \right)^{\alpha} dJ$$

$$= \sum_{l=0}^{\alpha} {\alpha \choose l} \beta_3 w_1^{\alpha-l} w_2^l \frac{1}{(2\pi)^{p/2} (|\psi_1|^{\alpha-l} |\psi_2|^l |((\alpha-l)\psi_1^{-1} + (l)\psi_2^{-1})|)^{1/2}} exp \left(-\frac{1}{2} \sum_{j=1}^{\alpha} (d_j - x_{k^j})^T D_j (d_j - x_{k^j}) \right)$$

where
$$x_{k^j} \in \Omega_-$$
 for $j = 1, 2...\alpha - l$
 $\mathbf{x}_{k^j} \in \Omega_+$ for $j = \alpha - l + 1, ...\alpha$

and
$$\beta_3 = \frac{1}{n_1^{\alpha - l}} \left(\sum_{k^0 = 1}^{n_1} \sum_{k^1 = 1}^{n_1} \dots \sum_{k^{\alpha - l} = 1}^{n_1} \right) \times \frac{1}{n_2^l} \left(\sum_{k^{0'} = 1}^{n_2} \sum_{k^{1'} = 1}^{n_2} \dots \sum_{k^{l'} = 1}^{n_2} \right)$$

$$(3.31)$$

$$\check{P}_{31} = \int_{\Re} P_1 \left(J, \Omega \right)^{\alpha - 1} k_{\sigma_1} \left(J(C) - J \right) dJ$$

$$= \frac{1}{n_1^{\alpha-1}} \left(\sum_{k=1}^{n_1} \sum_{k=1}^{n_1} \dots \sum_{k=1}^{n_1} \frac{1}{(2\pi)^{p/2} (\alpha|\psi_1|)^{1/2}} \times exp \left(-\frac{1}{2} \sum_{j=1}^{\alpha} (d_j - x_{k^j})^T D_j (d_j - x_{k^j}) \right) \right)$$

where
$$x_{k^j} \in \Omega_-$$
 for $j = 1, 2...\alpha - 1$
$$\mathbf{x}_{k^j} = J(C) \text{ iff } j = \alpha$$
 (3.32)

$$\check{P}_1 = \int_{\Re} P_1 \left(J(x), \Omega \right)^{\alpha} dx$$

$$= \frac{1}{n_1^{\alpha}} \left(\sum_{k=1}^{n_1} \sum_{k=1}^{n_1} \dots \sum_{k=1}^{n_1} \right) \frac{1}{(2\pi)^{p/2} (\alpha|\psi_1|)^{1/2}} \times exp \left(-\frac{1}{2} \sum_{j=1}^{\alpha} (d_j - x_{k^j})^T D_j (d_j - x_{k^j}) \right)$$

where
$$x_{k^j} \in \Omega_-$$
 for all j (3.33)

 \check{P}_2 and \check{P}_{32} are equivalent to \check{P}_1 and \check{P}_{31} , under the condition that P_2 , n_2 and Ω_+ are substituted for P_1 , n_1 and Ω_- .

Considering these definitions, equation 3.11 can be rewritten as

$$\frac{\partial E(\phi)}{\partial t} = \frac{1}{1-\alpha} \frac{\check{P}_{11} + \overline{P}_{11} + \check{P}_{22} + \overline{P}_{22}}{\overline{P}_{312}} + \frac{\alpha}{1-\alpha} w_1 \frac{\check{P}_{31} + \check{P}_1}{\check{P}_1} - \frac{\alpha}{1-\alpha} w_2 \frac{\check{P}_2 - \check{P}_{32}}{\check{P}_2}$$

$$(3.34)$$

CHAPTER 4 A 4D Biomechanical Lung Phantom for Joint Segmentation/Registration Evaluation

This represents a print of "D. Markel, I. Levesque, J. Larkin, P. Léger and I. El Naqa, A 4D Biomechanical Lung Phantom for Joint Segmentation/Registration Evaluation, Accepted in Physics in Medicine and Biology (2016)"

4.1 Abstract

At present, there exist few openly available methods for evaluation of simultaneous segmentation and registration algorithms. These methods allow combination of both techniques to track the tumor in complex settings such as adaptive radio-therapy. We have produced a quality assurance platform for evaluating this specific subset of algorithms using a preserved porcine lung in such that it is multi-modality compatible: Positron Emission Tomography (PET), Computer Tomography (CT) and Magnetic Resonance Imaging (MRI). A computer controlled respirator was constructed to pneumatically manipulate the lungs in order to replicate human breathing traces. A registration ground truth was provided using an in-house bifurcation tracking pipeline. Segmentation ground truth was provided by synthetic multicompartment lesions to simulate biologically active tumor, background tissue and a necrotic core. The bifurcation tracking pipeline results were compared to digital deformations and used to evaluate three registration algorithms, Diffeomorphic demons, Fast-Symmetric Forces Demons and MiMVista's deformable registration tool. Three

segmentation algorithms the Chan Vese level sets method, a Hybrid technique and the Multi-Valued level sets algorithm. The respirator was able to replicate three seperate breathing traces with a mean accuracy of 2-2.2%. Bifurcation tracking error was found to be sub-voxel when using human CT data for displacements up to 6.5 cm and approximately 1.5 voxel widths for displacements up to 3.5 cm for the porcine lungs. For the Fast-Symmetric, Diffeomorphic and MiMvista registration algorithms, mean geometric errors were found to be 0.430 ± 0.001 , 0.416 ± 0.001 and 0.605 ± 0.002 voxels widths respectively using the vector field differences and 0.4 ± 0.2 , 0.4 ± 0.2 and 0.6 ± 0.2 voxel widths using the bifurcation tracking pipeline. The proposed phantom was found sufficient for accurate evaluation of registration and segmentation algorithms. The use of automatically generated anatomical landmarks proposed can eliminate the time and potential innacuracy of manual landmark selection using expert observers.

4.2 Introduction

The introduction of hybrid PET/CT and more recently PET/MRI scanners [118] has provided physically registered multi-modal datasets for diagnostic purposes and radiotherapy planning. This provides a large opportunity for multi-modal segmentation algorithms to improve target definition accuracy particularly for cancerous tumors where the shape, location, intensity distribution and texture is widely variable [119]. For many centers that do not have access to hybrid scanners or when considering images from multiple fractions or gated scans taken during free breathing, multi-modal segmentation accuracy relies heavily on the quality of the registration process used to bring the datasets of images into alignment.

Segmentation and registration, two common image processing algorithms used often in the process of adaptive radiotherapy have increasingly been used in a simultaneous fashion [120, 121, 122, 123, 124, 125, 126]. For multi-modal segmentation this improves the alignment of the input volumes while the additional boundary information can aid in the registration process. In many cases the registration is used solely to aid in the segmentation process as with Atlas-based algorithms or contour templates. Numerous benchmarks have been developed for evaluating each method independently [127, 128, 129, 130, 131]. Kerdok et al. developed a silicone rubber phantom called truthcube to evaluate soft tissue deformation using implanted Teflon beads. Compared to a simulation using Finite Element Method (FEM) software they found discrepancies on the order of 3.5 mm for displacements of 1.5 cm. This was attributed to lack of refinement of the FEM model and a 2 mm estimated uncertainty of the bead locations. Serban et al, developed a cylindrical phantom comprised of natural sea sponges interlaced with nylon wires, lucite beads and round dermasol tumors. The sponge is actuated by an industrial motor in order to simulate breathing phases. Ground truth uncertainty was dominated by the uncertainty in manual selection of these landmarks, the 2.5 mm diameter of the lucite beads and scan resolution (0.7x0.7x1.25 mm³ at its highest). Liu et al. used foam inserts within a custom made polymer shell and plastic 1x5 mm seeds as markers. Their positional uncertainty was dominated by the slice thickness of their scan and estimated at 1.7 mm. Additionally they used an NCAT virtual phantom for evaluation using estimated deformation vectors from a series of patient breathing scans. Numerical models and virtual phantoms such as NCAT [132], XCAT [133], VIP-man [134], CNMAN [135] among many have been regarded as a pseudo gold standard for registration benchmarking due to the fact that the final location of any point in the phantom is accurately known. The short-comings of such phantoms lay in the difficulty of recreating the complex features observed on clinical scans such as anatomical details, texture, geometric and temporal deformation patterns as well as image quality degradations such as artifacts and noise. As such the realism of such phantoms with regard to these properties is difficult to determine [136].

Physical phantoms can offer additional geometric realism along with realistic imaging characteristics at the cost of introducing some ground truth uncertainty. Yang et al. utilized a preserved swine lung in order to improve anatomical realism and allow MRI compatibility by placing the pneumatic actuator outside the scanning room [137]. In this case bifurcations of the lung are used as markers for evaluation but still rely on proper selection. Simultaneous registration and segmentation and the evaluation of both in the same setting remains a challenge and there is currently no gold standard.

Several factors are addressed with the proposed phantom which attempts to balance the trade-off of realism to ground truth knowledge. The goal of this work is developing hardware and software tools to provide a well known ground truth for evaluating both segmentation and registration in the same setting while maintaining realism through the use of a set of preserved swine lungs and a custom made computer controlled respirator that can precisely mimic real human breathing traces. The phantom is compatible with multiple modalities including PET, CT and MRI.

Tracking of bifurcations in the lung airways is used for evaluating registration accuracy along with synthetic lesions for evaluating segmentation accuracy.

4.3 Materials and Methods

4.3.1 Lung Tissue

An educational kit consisting of porcine lungs contained within a preservative solution (74% water, 25% propylene glycol, 0.3% formaldehyde and traces of phenol) was used to simulate a set of human lungs due to similarities in anatomy and capacity. The swine lungs are advertised with a vital capacity of approximately 4.6 L compared to 3-5 L for humans [138]. The samples are meant to last 6 months but can last longer with proper storage.

4.3.2 Computer Controlled Airflow System

Shown in figure 4–1 is the airflow system used to inflate the lungs. Air pressure within the lungs is regulated by a set of bellows actuated by a 186 watt Baldor industrial motor. An 8 meter long vinyl tube with a 1.27 cm diameter connects the bellows to the lungs. A second 6.35 mm port is used to supply air from an aquarium pump into the bellows to account for any leaks in the sample. Ideally, the port is replaced with a plug in the case of a closed system. In order to attain constant torque while varying the speed of the motor, a driver circuit was designed to provide pulse width modulation of the driving voltage. This is controlled by a National Instrument data acquisition module connected to a laptop running LabVIEW 2013 (32-bit) (National Instruments, Austin, TX). The direction of the motor is controlled by changing its polarity with a relay. A 2500 point resolution optical encoder was used to provide feedback to the data acquisition card. The control software relies on a

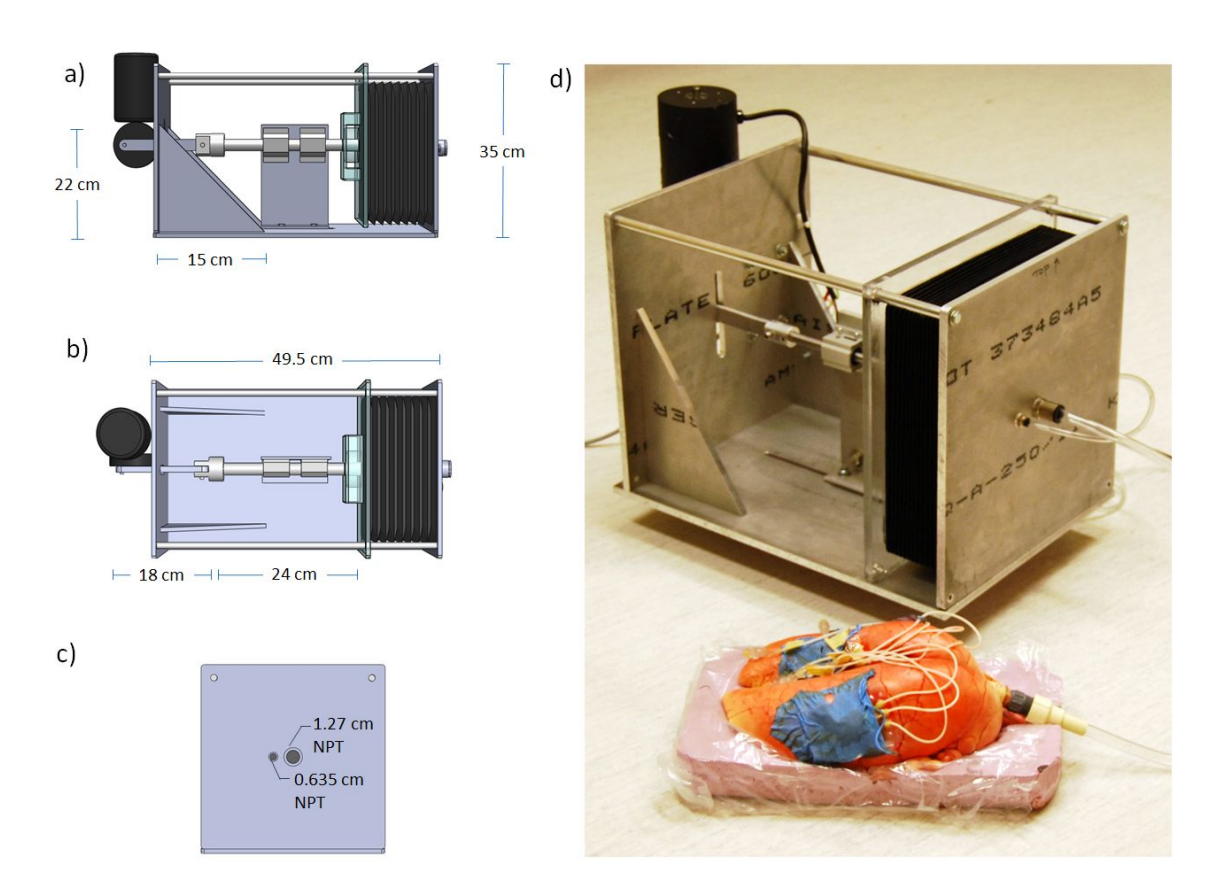


Figure 4–1: The computer controlled airflow system model shown from the a)side, b)top, c)front and d)photographed connected to the swine lungs. The main piston has a 4 cm range of motion and is held horizontal by a pair of pillow block bearings attached to a mounting plate.

proportional-integral-derivative (PID) controller, using the position of the breathing trace every 40 ms as a new set point. PID controllers are feedback systems commonly used in industrial automation. Their function is governed by Equation 4.1.

$$u(t) = K_p e(t) + K_i \int_0^t e(\tau) d\tau + k_d \frac{de(t)}{dt}$$

$$\tag{4.1}$$

Where u(t) is the update to the controlled variable based on the error e(t) between the current variable value and set point. t in this notation is the time and τ is a variable of integration the ranges from 0 to t. In this case the controlled variable is the linear position of the respirator piston and the set point is the scaled breathing trace. K_p , K_i and K_d and the proportional gain, integral time and derivative time. The proportional gain drived the variable value towards the set point in order to minimize the error between the two. Since the proportional term is linearly dependant on the error, the correction to the controlled variable shrinks as it approaches the set point, never quite reaching it. The integral term attempts to equalize the time spent above and below the set point and works towards ensuring the controlled variable reaches the set point instead of approaching it asymptotically. Often the interplay between the first two terms can lead to unwanted behaviour such as ringing about the set point. The derivative time, or third term, acts to smooth the transition to the set point, reducing ringing. In practice, the relationships between the three terms can be much more complex and optimization of the three variables K_P, K_i and K_d can be very difficult. Thus the proportional gain, integral time and derivative time were optimized using the Ziegler Nichols method [139] $(K_p=1.82,$

 K_i =0.11, K_d =0.03). Reversal of the motor direction was limited to switching between the inhale and exhale phases of breathing. Changing the motor direction due to an overshoot was prohibited in the control software in order to prevent the relay from switching too quickly and burning out its contacts. In these cases, the motor was turned off temporarily to allow the breathing trace to catch up with current position of the motor.

4.3.3 Synthetic Targets

Figure 2 shows the segmentation targets constructed from natural sea sponges. Each sponge was vacuum-sealed in order to reduce the presence of air bubbles and increase their rigidity, preserving their shape during the scan and subsequent handling. The synthetic targets consisted of two sealed sponges, one placed inside the other with the inner sponge approximating a biologically active tumor region and the outer, typical surrounding healthy tissue. Two synthetic lesions with this configuration were attached to the lungs within neoprene pouches while a third designed with three compartments was also included. This design was meant to mimic a heterogenous tumor with a necrotic core. Figure 4–2 shows scans of the three synthetic targets using CT, MRI and PET.

For each synthetic tumor, two medical injection ports (three for the heterogenous tumor) were attached to allow injection of fluorodeoxyglucose ([18F] FDG) radiotracer. In order to determine the compartment boundaries, a 65% iohexol CT contrast agent (diluted to 323.5 mg/mL) mixed with 18-FDG radiotracer at a final activity concentration of 60 kBq/ml was injected into the inner compartment. The outer compartment was injected with a mixture of Gadovist gadolinium-based MRI

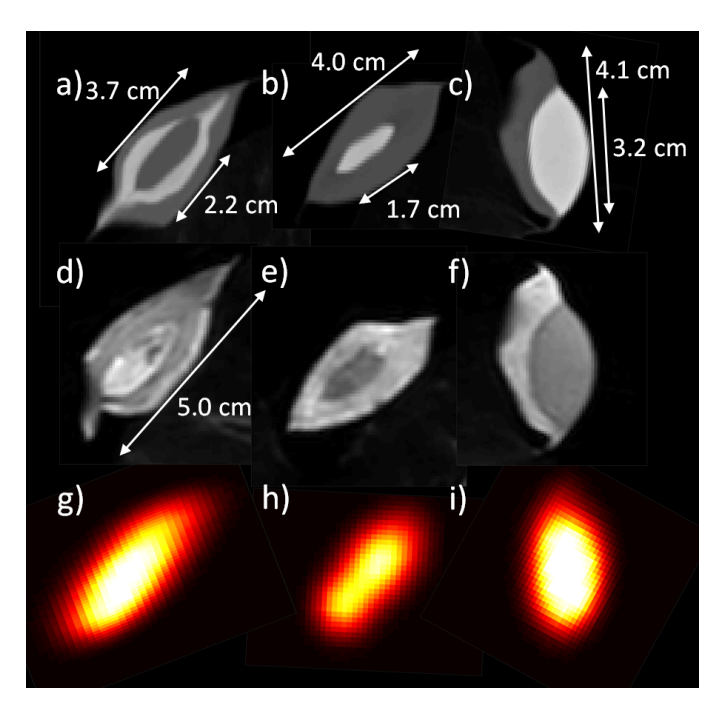


Figure 4–2: Transverse views of the synthetic targets scanned with CT (a)-c)), MRI (d)-f)) and PET (g)-i)). The targets 1-3 are organized from left to right. Target 1 consists of compartments 1.2, 13.9 and 20.2 cm³ in volume from the inside to the outside. Target 2 is made up of compartments with volumes of 0.85 and 21.9 cm³. Likewise, target 3 has compartments of 10.8 and 13.9 cm³ in volume. Maximal diameters for each compartment are shown in white. Image scaling for each target may not match.

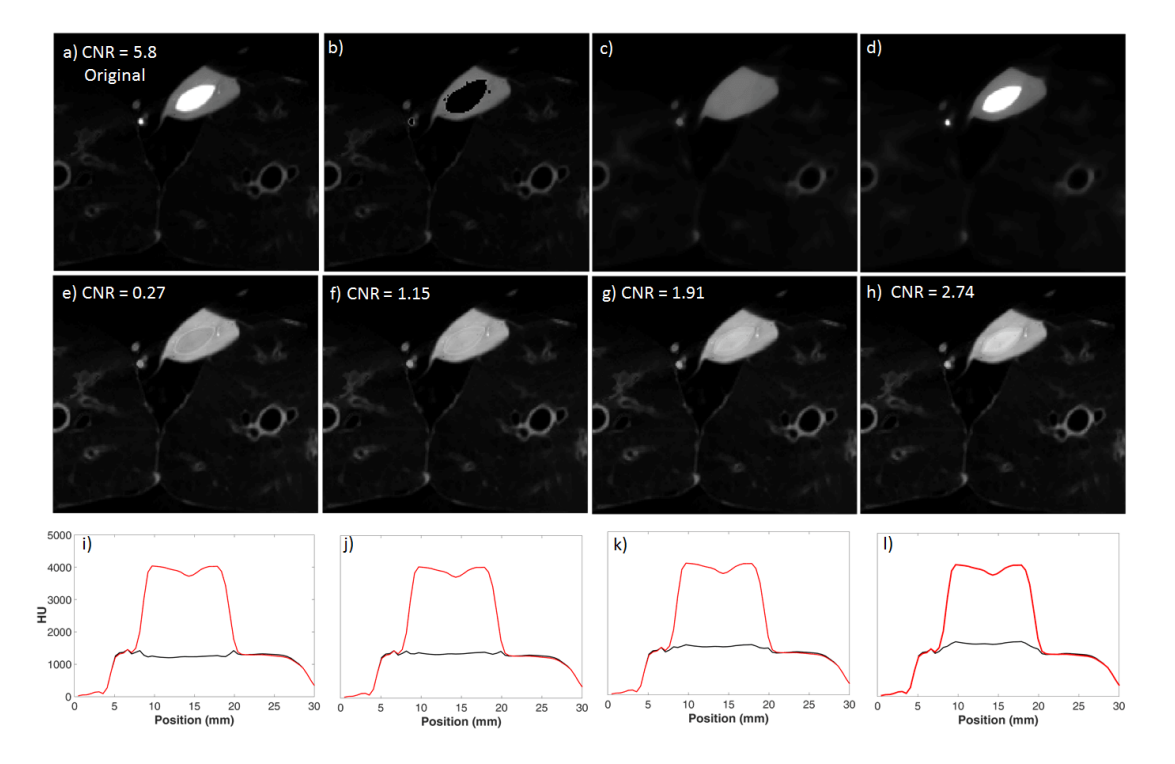


Figure 4–3: The compartment obfuscating procedure with a) the original image, b) the image after the compartment has been replaced with NaN values, c) the image following inpainting and smoothing and d) the original image smoothed using the same filter. e)-h) show a range of contrast values by varying λ in Equation 4.2 from 0.9 to 1.05 in 0.05 increments. These same values were used to evaluate the three segmentation methods shown in Figure 4–9. A horizontal profile of the synthetic tumor taken from e)-h) is shown below in i)-l).

contrast agent (diluted to 3.6 mg/ml) and 18-FDG at a final activity concentration of 30 kBq/ml. Using the contrast provided by the iohexol and Gadovist contrast agents, the boundaries of the active compartments were discerned by thresholding the volumes using values of 376 HU, 500 HU for the CT and CBCT images respectively. The MR images were thresholded using a window between 10-60% of the

maximum signal in the neighbourhood of the synthetic tumors. Any errors resulting from this were then corrected manually using the open source software 3D slicer.

The contrast agents were used as a means to easily determine the boundaries of the compartments meant to mimic biologically active tumors. However, this contrast would also have the effect of compromising the ability to compare the performance of different segmentation algorithms since the boundary is easily discernable. To remedy this, the intensity distribution of the active compartment was digitally altered in order to reduce the contrast and obfuscate the compartment boundary according to Equation 4.2. First an estimate of the background compartments was made using a HU window of 924-1400 HU. The upper range of this threshold was purposefully overestimated. To get a more precise estimate of the appropriate upper boundary on the threshold range, the histogram of the background compartment is taken and upper leading edge (defined as the first local minima past the peak) was used. This new threshold range is then used to define the active compartment in such a way that it includes any partial volume effects around the border. In painting is then performed on this region using inverse distance weighting with a power value of 11. A diffusion filter presented by Weickert et al. [140] was used to smooth the region inside the compartment without blurring the borders significantly (# of Iterations $=15,\tau=0.7$, kernal size = 1, threshold = 0.7). This was also used on the original image to produce two images A (for the smoothed original) and B for the smoothed background image, to determine the ratio by which the original image must be multiplied to reduce the contrast. Smoothed versions are used to retain texture and noise information as much as possible when altering the original image according to Equation 4.2.

$$I'(x) = I(x) - \lambda \left(I(x) - I(x) \frac{B}{A} \right)$$
(4.2)

Where I and I' are the unaltered and altered images, x is the subset of voxels within the synthetic target. A and B are the smoothed background and original images. λ is a parameter to control the contrast of the active compartment.

$$CNR = \frac{\mu_{fg} - \mu_{bkg}}{\sigma_{bkq}} \tag{4.3}$$

The contrast-to-noise ratio (CNR) is calculated from Equation 4.3 where μ_{fg} , μ_{bkg} and σ_{bkg} are the active compartment mean, background compartment mean and background standard deviation respectively. A range of CNR values are shown in Figure 4–3.

4.3.4 Bifurcation Tracking Pipeline

In order to discern a ground truth for registration evaluation, bifurcations of the bronchi were used as fiducial points of comparison between scans. The bifurcation tracking pipeline, outlined in Figure 4–4 begins with a segmentation of the lung bronchi by using a region growing algorithm in the space surrounding the bronchi and inverting this binary image. A 3D skeletonization procedure is performed on the segmented bronchi to reduce them to their medial axis based on the work by Lee and Kashyap [141]. The bifurcations of this skeleton are detected in a fashion similar to that used by Nallaperumal et al. [142] extended to the 3-dimensional case using neighbourhood templates. In order to reduce the search neighbourhood, only

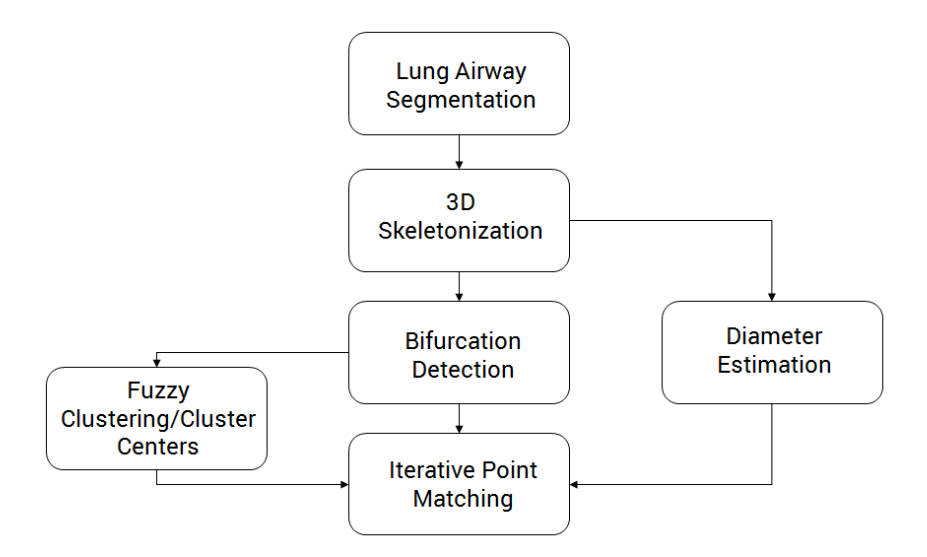


Figure 4–4: The bifurcation tracking pipeline. This consisted of an initial region growing of the air in the lungs, followed by morphological hole filling and subtraction from the original mask to segment the lung airways. A 3D skeletonization procedure determines the medial axis of the airways which are then compared against a bank of automatically generated 3D templates to detect bifurcations. The detected bifurcations from two lung volumes are then matched using the estimated diameter of the bronchi and an initial rigid alignment using cluster centers.

333 voxel neighborhoods in the skeleton mask with exactly 4 voxels belonging to the skeleton are compared to a lookup table of neighbourhoods that would represent a bifurcation in the medial axis.

The neighbourhoods of the lookup table were automatically generated by iteratively considering every voxel in a 3x3x3 neighbourhood and assigning a value of 1 to 4 of them. Here the center is always given a value of 1. Every other voxel is considered for the second voxel and the third and fourth are likewise iterively selected from the remaining set under the condition that they cannot be directly touching another voxel with a value of 1. In total 9480 templates were automatically generated.

After detection of the bifurcation points from two volumes they are matched by first estimating a rigid transformation. A fuzzy clustering algorithm is used to determine the cluster centers of the bifurcation points of each lung. The difference in centers between the two data sets is used to initialize the transformation. A second non-rigid transformation using the thin-plate-spline robust point matching (TPS RPM) algorithm published by Yang [41] in 2011 was used to match landmarks between both point clouds. The algorithm was chosen for its ability to match point clouds where some of the points don't have a corresponding match in the second cloud by enforcing a smooth transformation. The energy function of the registration included the euclidean distance between point pairs and the difference in bronchial radii, summarized in Equation 4.4. This was estimated from the segmentation mask of the bronchi. First principle component analysis was performed on a 21x21x21 voxel neighbourhood surrounding any detected bifurcation. The first eigenvector estimates the medial axis of the bronchi and the normal of the plane that perpendicularly cuts through the bronchi. The radius can be estimated by assuming a circular cross section and inverting the formula for the area of a circle. The formula for the energy function was given by simple addition

$$E(i,j) = |\vec{x_i} - \vec{x_j}| + \beta |r_i - r_j| \tag{4.4}$$

Where $\vec{x_i}$ and $\vec{x_j}$ are the euclidean coordinates of bifurcation points i and j and r_i and r_j are the radii of their respective bronchi. β was determined through trial and error to be 40 by maximizing the true positive rate of the point pair candidates. Finally a GUI, shown in Figure 4–5, was written to show the candidate point pairs

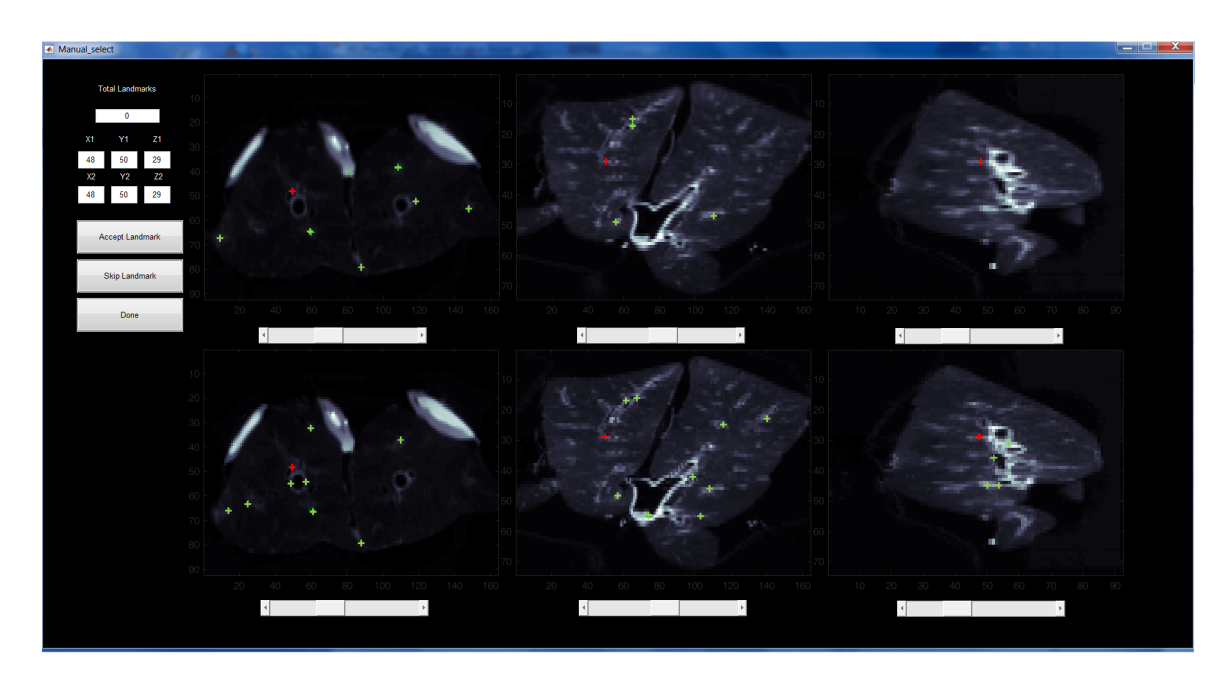


Figure 4–5: Graphical User Interface written for quality control of matched bifurcation points. Red croses show the point pair selected by the iterative point matching algorithm. Green crosses represent detected bifurcations in each volume. The GUI shows a CT scan of the lungs from three planes, transverse, coronal and sagittal (ordered left to right).

to the user for a final confirmation, rejection or potential reselection of the matching point. In the event of a mismatch, alternative bifurcations can be selected if they are found to be the appropriate matching landmark. The pipeline accuracy was evaluated by applying a known virtual deformation to a CT scan of a patient and the porcine lung itself. The detected bifurcation locations were compared to the known final locations.

4.3.5 Scanning Parameters

PET and CT scans were acquired using a GE Discovery 690 hybrid PET/CT scanner at the PERFORM institute, Concordia University. Four-dimensional (3D+t) PET scans of the lungs were taken during free-breathing and discretized into 6 bins/phases. The scans were acquired over the course of an hour and reconstructed with the VUE point HD (VPHD) algorithm using several time periods (first 25 s, 20 min, 30 min and 60 min) in order to vary the resulting quality of the scan. CT images were taken in CINE mode using a voltage of 140 kVp and currents of 10, 55 and 140 mA. The position of the lungs was tracked using the Real-time Position Management (RPM) System which relied on a reflective marker placed on top of the lungs. This was imaged using an infrared illumator and CCD camera in the scan room. The 6 bins were centered at 8%,25%,42%,58%,75% and 92% of the breathing cycle. MRI scans were acquired at the Cedars Cancer Center using a Philips (Amsterdam, The Netherlands) 3.0 T Ingenia. The lungs were scanned using a T1-weighted fast field echo (FFE) sequence (FA = $90\deg$, TE = $9 \operatorname{ms}$, TR = $520 \operatorname{ms}$) and with water fat shift coefficients of 0.45 and 0.99. Due to the lack of commercial sequences for 4D MRI imaging of the lungs, the respirator was used to hold the lungs at 6 specific breathing phases for the duration of a series of 3D scans in order to match the data sets acquired using the 4D PET/CT scans. The image volumes were reconstructed with resolutions of 3.64x3.64x3.27 mm³, 1.7x1.7x5 mm³ and 0.61x0.61x3 mm³ for the PET, CT and MRI scans, respectively.

CBCT scans were performed using the on-board imager of a Varian Truebeam linear accelerator (Varian Medical Systems, Palo Alto, CA) using a potential of 80 kVp and a current of 50 mAs with a spatial resolution of 0.51x0.51x2 mm³.

4.3.6 Human Breathing Reproduction

Three female patients undergoing radiotherapy treatment, all presenting with carcinoma in either the small intestines or the liver, were chosen to attain a sample of varied human breathing patterns. Breathing traces were measured using a Philips (Amsterdam, The Netherlands) respiratory bellows belt. The three profiles were anonymized and imported to the control software for replication. This was accomplished by setting the breathing trace as a set point that changed every 40 ms. Reserve and tidal volume of the swine lungs are set by the user, determining the offset and magnitude of the rescaled breathing trace. Profiles were also smoothed using a box filter with a 100 ms width in order to eliminate noise in the traces.

4.4 Comparable Methods

As a proof of concept three level-sets segmentation methods were used to segment the radiologically active portions of the artificial lesions on all four modalities in which images were acquired. The Chan-Vese model [143], a Hybrid techique published by Zhang et al. [144] and the multi-valued level set method [101] were chosen as example algorithms. The Chan Vese method is a level sets implementation that

attempts to optimize the Equation 4.5.

$$F(c_{1}, c_{2}, \phi) = \mu \int_{\Omega} \delta(\phi(x, y)) |\nabla \phi(x, y)| dxdy + \nu \int_{\Omega} H(\phi(x, y)) dxdy + \lambda_{1} \int_{Omega} |u_{0}(x, y) - c_{1}|^{2} H(\phi(x, y)) dxdy + \lambda_{2} \int_{\Omega} |u_{0}(x, y) - c_{2}|^{2} (1 - H(\phi(x, y))) dxdy$$
(4.5)

The level set implementation relies on an implicit mapping through the function $\phi(x,y)$ (in 2D) where the contour is defined at the zero-level crossing ($\phi(x,y) = 0$). The first regularizes the roundness of the segmentation contour while the second term is a retarding velocity parameter which works to limit the expansion or contraction of the contour. The third and fourth term are the expansion and contraction forces driving the evolution of the contour, controlled by the weighting parameters λ_1 and λ_2 . In our implimentation λ_1 and λ_2 are equal to the image weight (IW) whereas ν is set to zero and μ set to 1. H is the regularized Heaviside function, that ensures that changes to the level set function occur in the proximity of the contour.

The Second method being evaluated is a hybrid technique built off the Chan-Vese formulation that proposes the energy function shown in Equation 4.6.

$$F(\phi) = -\alpha \int_{\Omega} (I - \mu) H(\phi) d\Omega + \beta \int_{\Omega} g |\nabla H(\phi)| d\Omega$$
 (4.6)

In Equation 4.6 g is a boundary feature map which is a function of the gradient of the image intensity I. The variable μ in this context takes on the role of the lower bound of the gray-level of the intended target. As the algorithm is built to enclose a region with higher values than μ this acts as a threshold value. The values α and

 β represent the propogation weight (PW) and geodesic active contour (GAC) terms respectively. The Multi-Valued Level Set Method was designed to incorporate coregistered multi-modality information with weights used to enforce the importance of each modality in the energy function summarized in Equation 4.7.

$$inf_C J(C, c^+, c^-) \propto \mu length(C) + \frac{1}{N} \sum_i \lambda_i^+ \int_{\Omega} |I_i - c_i^+|^2 H(\phi) dx + \lambda_i^- \times \int_{\Omega} |I_i - c_i^-|^2 (1 - H(\phi)) dx + \frac{1}{N} \sum_i \gamma_i (c_i^+ - c_i^-)^2$$
 (4.7)

Here C represents the contour, c^+ and c^- represent the regions outside and inside the contour. Image i is sampled N times and λ_i^+ , λ_i^+ and γ_i represent the weights outside and inside the contour and the spring force for image i. Similar the Chan-Vese and Hybrid formulism, μ controls the roundess, or smoothness of the contour.

All three techniques were identically intialized using a sphere with a radius of 4 voxels and allowed to evolve until a convergence criteria was met. In this case we chose a termination criteria based on the change in volume dropping below 1%. The smooth weight μ for the Chan Vese method was set to 1 and not varied since the results were found to be relatively insensitive to it.

4.5 Results

4.5.1 Bifurcation Tracking Evaluation

In order to evaluate the bifurcation tracking results, a digital deformation was applied to a CT scan of the porcine lungs in addition to a human CT dataset acquired at the MAASTRO clinic (Maastricht, The Netherlands) of a patient with stage-I non-small cell lung carcinoma. The scan was acquired using a Biograph SOMATOM Sensation 16 scanner (Siemens, Erlangen Germany). The patient was scanned with

a spiral CT with contrast at a resolution of 0.98x0.98x5 mm. This data set was previously acquired in a study by Baardwijk et al.[89]. The deformations were defined globally using Equations 4.8, 4.9 and 4.10.

$$dx = -A\sin\left(\frac{(X - origin_x) \times \pi}{dim_x/2}\right) \tag{4.8}$$

$$dy = -A\sin\left(\frac{\left(Y - origin_y\right) \times \pi}{dim_y/2}\right) \tag{4.9}$$

$$dz = -A\cos\left(\sqrt{\left[\left(X - origin_x\right)\pi/dim_x\right]^2 + \left[\left(Y - origin_y\right)\pi/dim_y\right]^2}\right) \quad (4.10)$$

Where X, Y and Z are the cartesian coordinates of the voxels in each volume, $origin_i$ represents the coordinates of the center of the volume, dim_i represents the dimensions of the volume and A is a free parameter representing amplitude. The amplitude was varied from 16 to 83 mm in order to discern the relationship to tracking error which is shown in Figure 4–6. Bifurcation points were detected and matched in both the deformed and undeformed volumes and compared to the known deformed coordinates.

4.5.2 Breathing Reproducibility

After optimizing the PID controller coefficients, the breathing traces were compared to the optical encoder feedback for the length of the profiles. A visual comparison is shown in Figure 4–7 for the three chosen profiles. Table 4–1 summarizes the errors of the traces compared to the feedback from the optical encoder.

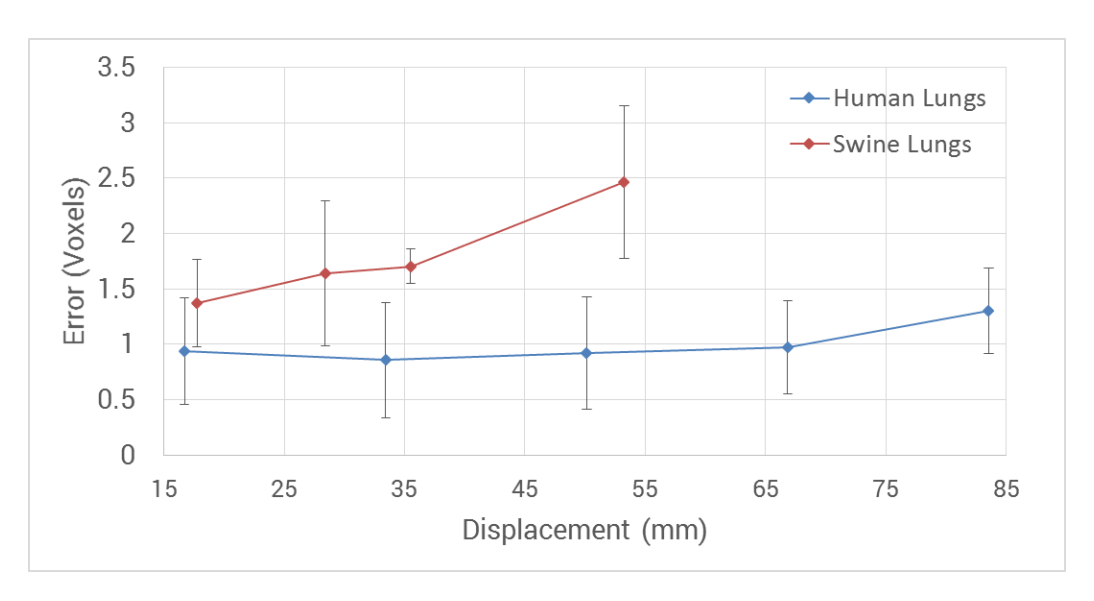


Figure 4–6: Bifurcation tracking error as a function of deformation magnitude for human and phantom lungs

Table 4–1: Summary of the reproduction error for the three profiles.

| Profile # | Mean Error (%) | Standard Deviation (%) |
|-----------|----------------|------------------------|
| 1 | 2.2 | 2.1 |
| 2 | 2.0 | 1.5 |
| 3 | 2.2 | 1.6 |

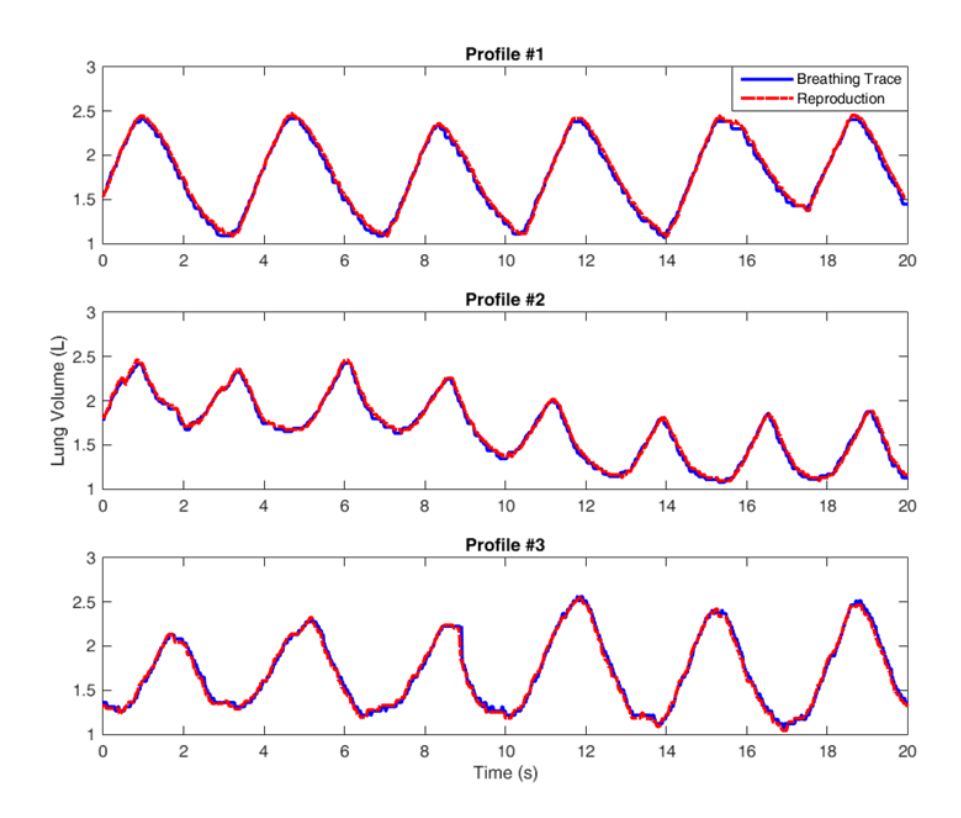


Figure 4–7: The three profiles tested using the computer controlled respirator. The measured breathing trace using the respiratory bellows belt is shown in blue with the feedback from the optical encoder showing the piston position is plotted in red.

| Modality | Target | Chan Vese-IW | Hybrid-PW | Hybrid-GAC | $MVLS-\lambda_{1,2,3}$ |
|--------------------------|--------|--------------|-----------|------------|-----------------------------------|
| $\overline{\mathrm{CT}}$ | 1 | 1e-4 | 1.42e-3 | 1e-7 | [4,4;4,4;2,2] |
| | 2 | 1e-4 | 1.2e-4 | 1e-7 | [4,4;4,4;3,3] |
| | 3 | 1e-4 | 5.4e-4 | 1e-7 | [4,4;4,4;1,1] |
| CBCT | 1 | 4.6e-5 | 4e-4 | 0.02 | [10,10;10,10;3,3] |
| | 2 | 4.6e-5 | 1e-4 | 0.02 | [10, 10; 10, 10; 2, 2] |
| | 3 | 4.6e-5 | 1e-4 | 0.02 | [10,10;10,10;2,2] |
| MRI | 1 | 12 | -1e-5 | 1e-6 | $[60,\!60;\!60,\!60;\!0.5,\!0.5]$ |
| | 2 | 24 | -1e-5 | 1e-6 | [6,6;6,6;0.5,0.5] |
| | 3 | 9 | -1e-5 | 1e-6 | [4,4;4,4;0.5,0.5] |
| PET | 1 | 5e-7 | -2e-6 | 1e-7 | [4,4;4,4;1,1] |
| | 2 | 2e-7 | -2e-6 | 1e-7 | [1.5, 1.5; 1.5, 1.5; 1, 1] |
| | 3 | 2.5e-7 | -2e-6 | 1e-7 | [3,3;3,3;1,1] |

Table 4–2: Optimal parameters for segmenting the targets of the lung phantom. The $\lambda_{1,2,3}$ array is shown such that λ^+,λ^- are represented in the columns with i shown along the rows

4.5.3 Segmentation Evaluation

The parameters of each segmentation algorithm were optimized through brute force evaluation of a large range until a maxima was determined for each target. This was done in order to use the best possible results from each algorithm. The optimal parameters are summarized in Table 4–2.

The resulting segmentation was compared to the target ground truths for each modality. Figure 4–8 summarizes the results of the segmentation algorithms for each of the four modalities.

The active compartment volumes were 13.87, 0.85 and 10.8 cm³s for synthetic lesions 1,2 and 3 respectively. The Cone-Beam CT images were altered using Equation 4.2 in order to evaluate the effect of contrast on the segmentation performance

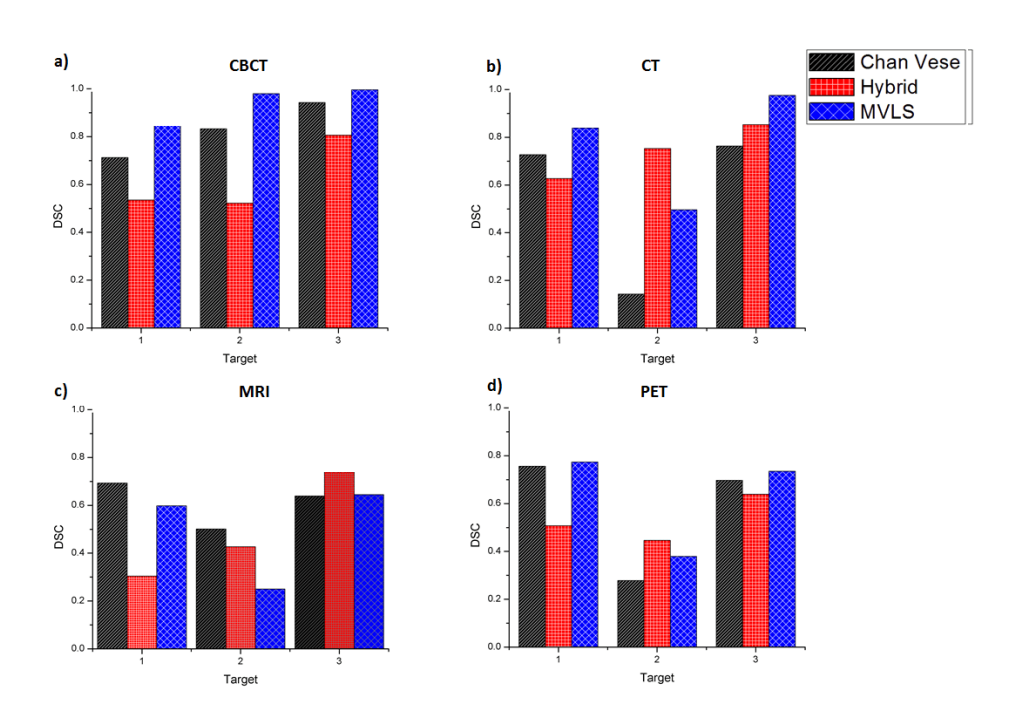


Figure 4–8: A summary of the segmentation results for the three algorithms (Chan-Vese, Hybrid and MVLS) using three synthetic lesions for a) CBCT, b) CT, c) MRI and d) PET.

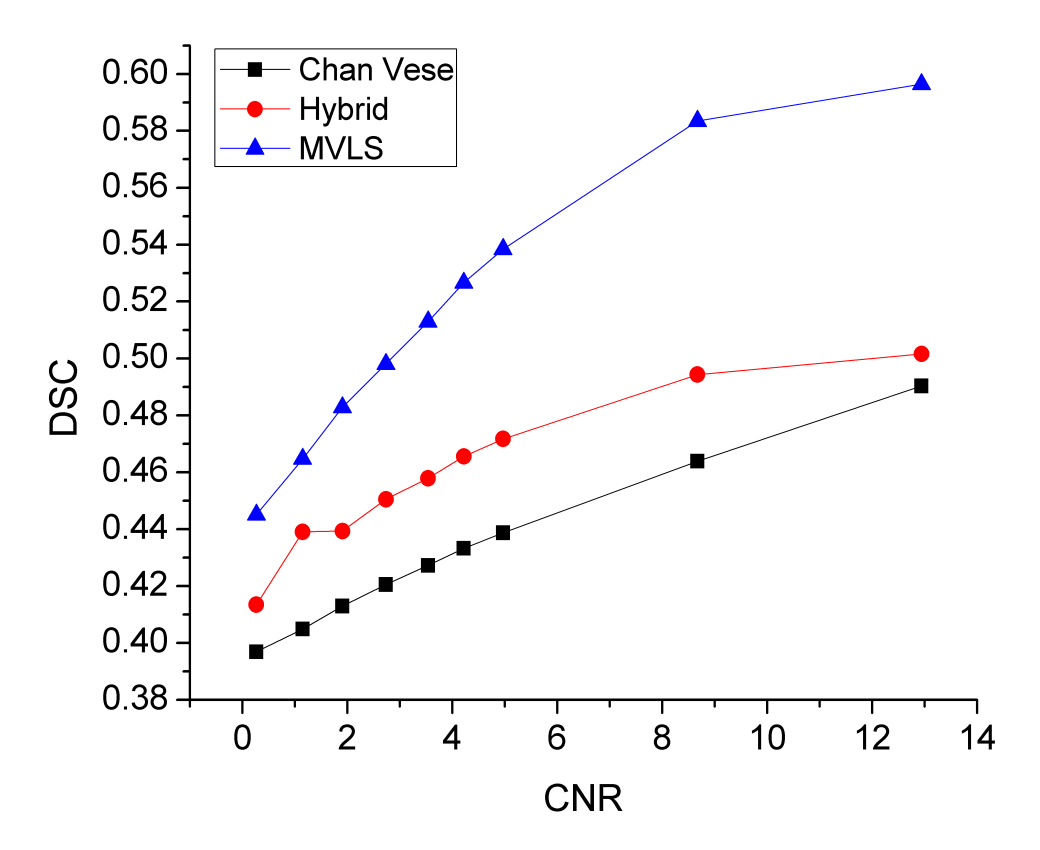


Figure 4–9: The Dice coefficient of the three segmentation methods evaluated using the lungs for varying CNR values of the active compartments of synthetic lesion 1

of the three algorithms. For CBCT the MVLS algorithm has the highest consistent Dice coefficient for each of the three targets. For the remaining modalities the results show a lower Dice coefficient for target 2, the smallest of the three, however the Hybrid algorithm outperforms the other two methods with regard to this target with the exception of when applied to CBCT. Figure 4–9 summarizes the results of the three algorithms for varying CNR values where CNR is calculated using the form in Equation 4.3

From Figure 4–9 we can see that while the MVLS is the most affected by loss in target contrast, it still performs with the highest DSC when compared with the

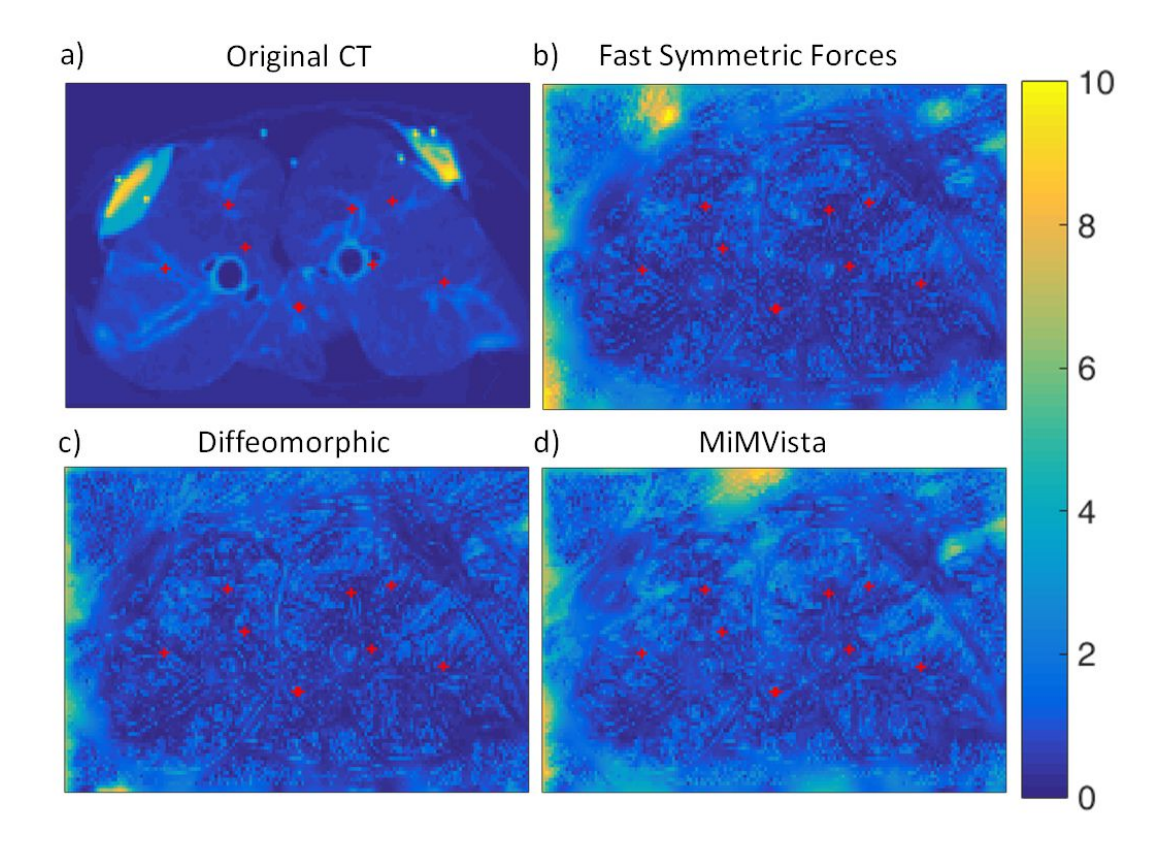


Figure 4–10: Error maps using the vector field differences of the original Demons algorithm with b) The fast Symmetric Forces registration b)Diffeomorphic demons and c)MiMVista's deformable registration algorithm. The side bar represents the error in voxel widths. The red crosses mark detected bifurcation points within the current slice and adjoining 3 slices.

ground truth across all CNRs tested. At a CNR of 1.2 it performs almost equivalently with the Hybrid technique.

4.5.4 Registration Evaluation

Three registration algorithms were chosen for evaluation using the swine lung, these include the fast-symmetric forces Demons[145], Diffeomorphic demons[145] and MiMVista's deformable registration engine[146].

| Method | Vector Field TRE | Bifurcation | Equivalent Vec- |
|----------------|--------------------------------|-------------------------|-------------------------|
| | (Voxels[mm]) | Tracking TRE | tor Field TRE |
| | | (Voxels[mm]) | (Voxels[mm]) |
| Fast Symmetric | $0.430[0.73] \pm 0.001[0.003]$ | $0.4[0.7]\pm0.2[0.4]$ | $0.5[1.0]\pm0.1[0.2]$ |
| Forces | | | |
| Diffeomorphic | $0.416[0.74]\pm0.001[0.003]$ | $0.4[0.6]\pm0.2[0.4]$ | $0.4[0.7]\pm0.2[0.1]$ |
| MiMVista | $0.605[1.07] \pm 0.002[0.004]$ | $0.6[0.8] \pm 0.2[0.3]$ | $0.5[0.8] \pm 0.1[0.2]$ |

Table 4–3: Registration error metrics for the three registration algorithms. 1) The mean error comparing the vector field of the method to the reference vector field, 2) The maximum error of the vector field comparison, 3) The mean bifurcation landmark error and 4) the mean vector field error evaluated only at those landmark coordinates. The uncertainties stated here are the 95% confidence intervals calculated using Equation 4.11.

The algorithms were evaluated using their vector field differences with the reference field (calculated with the regular Demons algorithm) as shown in Figure 4–10. These results are summarized in Table 4–3 using three figures of merit. The first was a voxel by voxel comparison with a seperate vector field calculated using the regular demons registration algorithm included in 3D slicer. The warped reference image using this vector field was used as the target image in the other three registration procedures to account for any registration errors associated with the regular demons results. Since information outside the lungs consists of little more than noise and is of little interest, only the vectors within a mask of the lungs and the synthetic lesions was used during the evaluation. The second figure of merit consists of the average target registration error (TRE) of 35 tracked bifurcation points. Target registration error is simply the euclidean distance between landmarks as defined by Equation 4.11.

$$TRE(i) = \sqrt{(x_{i,1} - x_{i,2})^2 + (y_{i,1} - y_{i,2})^2 + (z_{i,1} - z_{i,2})^2}$$
(4.11)

Where $(x_{i,1}, y_{i,1}z_{i,1})$ and $(x_{i,2}, y_{i,2}z_{i,2})$ represent the euclidean coordinates for the *i*th pair of matching landmarks. The third figure of merit is the average of the vector field errors taken at the location of the tracked bifurcation points in order to observe an potential bias in using anatomical landmarks to evaluate registration accuracy since they are by definition areas of high information content. The 95% confidence interval as discussed by Castillo et al. [147] is the distance representative of the registration error distribution defined by Equation 4.12.

$$d_{95\%CI} = \frac{2s}{\sqrt{N}} \tag{4.12}$$

Where s is the pooled standard deviation of the set of error measurements associated with one algorithm (in this case we are only relying on our own measurements) and N is the number of measurements taken. This is calculated for both the error map and bifurcation tracking distributions.

4.6 Discussion

We have demonstrated the design, construction and application of a joint registration/segmentation evaluation phantom hardware and software tools using preserved porcine lung tissue, synthetic tumors and a bifurcation tracking pipeline. The construction of a computer controlled respirator allows reproduction of human breathing traces using the porcine lungs. The results of the bifurcation tracking evaluation show that the tracking algorithm is optimally used in human lungs where the mean error is sub-voxel for displacements up to 6.5 cm. This analysis used digitally

defined deformations in order to evaluate the tracing error with a high degree of precision however the drawback in using this approach is the potential loss of detail from interpolation, meaning that the results included in this paper should be considered upper limits on the error. The phantom was evaluated using known registration and segmentation algorithms The comparison of the three registration algorithms shows that the MiMVista algorithm demonstrated the highest average target registration error in all three metrics used although this difference was only 0.2 mm. While the comparison of multiple registration algorithms is a useful exercise, it has been performed using larger numbers of methods and more rigorously than presented here [147, 53, 148]. Our purpose of our comparison is to contrast our method with a known ground truth for evaluation of the algorithms. We can see that by comparing the bifurcation tracking results to the equivalent euclidean vector field differences in Table 4–3 that the average values fall well within the other's 95% confidence interval. This suggests the bifurcation tracking algorithm is capable of measuring the same mean error values then when the point correspondence is known explicitly for every voxel. It is well known that registration error in regions of low image detail and information tend to be higher than the average registration error [149] which suggests that using bifurcation points could contain some bias as they are often areas of high detail. When comparing the mean vector field error to the equivalent bifurcation point error we see the equivalent error is consistantly lower but not with any statiscal significance with p-values of 0.06, 0.32, 0.87 for the fast symmetric, diffeomorphic and MiMVista algorithms respectively. The only differences worth remarking upon are those for the results using MiMVistas' algorithm. This may stem from the differences in control point density where the demons algorithm used a dense control point scheme (effectively 1.7x1.7x5 mm³), MiMVista relied on a sparser grid (3x3x5 mm³) in the transverse plane resulting in a coarser deformation. For these three evaluations, we were able to discern the accuracy with narrow confidence intervals of 0.18-0.39 mm using only 35 landmarks. Algorithms with higher error variability would require larger point sets to accurately evaluate, which one can infer by Equation 4.11 assuming we desire an equivalent confidence interval. The number of landmarks available for comparison is determined by the performance of the tracking algorithm. The main bottleneck in selecting more points is the size of the bronchi being considered and the accuracy and sensitivity of the method used to segment the airways. Our segmentation approach is relatively rudimentary and thus our future efforts would be well spent in improving this aspect of the tracking pipline. Improved segmentation of finer structures in the lung would not only provide a larger number of bifurcations but reduce confusion with points not associated with the bronchial tree which is currently only excluded through manual intervention with the acceptance GUI. We found that compromised quality of the swine lungs and lack of even inflation led to false positives of bifurcations. This meant larger airways were relied upon for biurcation tracking in the swine lungs, explaining the differences in performance between human and swine point tracking. This is due to the fact that there is higher uncertainty in determining the medial axis for larger airways. Considering the differences in performance between the human and swine lungs, the use of lungs from another species of similar size might solve this issue due to differences in the

morphology of the lung. Additional improvements to the point-to-point registration and the GUI for checking the point pairs would reduce the time necessary to acquire larger sets of data making the platform more feasible for use beyond research.

Segmentation evaluation showed significantly degraded accuracy with respect to the smaller lesion for all modalities, a result that is consistent with previous studies [150, 151]. The hybrid and Chan Vese segmention methods appear to have difficulty segmenting the first lesion compared to the MVLS for the CBCT and CT modalities. This may be explained by the hetergeneous configuration of the first lesion as it was built with three compartments, one of which simulated a necrotic core. This seems to have a presented a challenge as the algorithms tended to neglect the core, segmenting the outer boundary of the active tumor region and even the background in some cases instead. Using CBCT images of the phantom with digitally altered contrast of the active tumor compartments we can see the effect on the performance of three segmentation algorithms we tested. The effect is more drastic on the MVLS algorithm, although this was simply due to the other two algorithms failing with higher CNR values.

An obvious addition to the phantom would be the inclusion of a flexible out shell for the lungs that resembled the appearance of a human torso as this would have a significant effect on registration and segmentation performance. We acknowledge that while the computer controlled respirator is a good step towards kinetic realism, the relation between movement of the lung and volume is more complex than the linear relationship that we have assumed here. The movement of the lungs is 3D and influenced by the diaphram, intercostal muscles and interaction with the pleural cavity among other biomechanical factors. The system presented here inflates and deflates freely and even with an outer shell can only be considered an approximation to a clinical case.

Another observation is that the synthetic tumors would mimic clinical conditions more closely if placed inside the lungs, a feat that was not attempted due to the risk of compromising the preserved lungs. We further plan to use the phantom in the future to assess motion prediction algorithms based on custom breathing traces.

4.7 Conclusions

The work presents the development of a multi-modal simultaneous segmentation and registration platform utilizing a biomechanical lung phantom. The phantom uses synthetic lesions constructed from vacuum sealed sea sponges and an in-house bifurcation tracking pipeline for segmentation and registration evaluation. We found using a PID controller that the airflow to the lungs could be controlled with 2.1% mean error of the input breathing profile. Bifurcation tracking error was measured to be sub-voxel for human lungs for displacements up to 6.5 cm and within the 95% confidence interval when evaluating registration error compared to using the error of the full vector field. The phantom was used to evaluate three segmentation algorithms (Chan Vese, A hybrid approach and the MVLS methods) on four separate modalities (CBCT,CT,PET and MRI).

4.8 Conflict of Interest

The authors of this paper have no direct financial connection to the any commercial identities mentioned in the article and no competing interests to disclose.

4.9 Acknowledgements

We would like to acknowledge and thank John Miller and Jen Dietrich from Modus Medical Devices Inc. (London, Ontario) for their technical assistance in constructing the respirator, Chantel Beausoliel and Chantal Morin for their assistance in PET scanning initial versions of the phantom and Dan Eyde from St Cloud Mining (Tucson, Arizona) for donating zeolite samples for an earlier version of the phantom. Funding was provided by the Natural Sciences and Engineering Research Council of Canada (NSERC-RGPIN 397711-11), the Research Institute of the McGill University Health Centre Studentship Award and McGill University through the Chalk Rowles Fellowship. Partial support to D.M. for this work came from the Natural Sciences and Engineering Research Council (NSERC) Medical Physics Research Training Network CREATE grant # 432290

CHAPTER 5

Simultaneous Registration/Segmentation using the Jensen Rényi Divergence

This represents a print of "D. Markel and I. El Naqa, Simultaneous Registration/Segmentation using the Jensen Rényi Divergence, Submitted June to Medical Physics (2016)"

5.1 Abstract

Registration and segmentation are two commonly used processes in radiotherapy treatment planning which place a considerable burden on time and processing resources. With respect to adaptive radiotherapy this can be prohibitive to the practicality of plan re-optimization. Presented is a simultaneous coupling of the two methods, termed regmentation, using an information theoretic technique called the Jensen Rényi divergence as an objective function. The Jensen Rényi covers a number of mathematical forms very similar to well known statistical similarity measures such as the Kullback Leibler divergence or the Bhattacharyya coefficient depending on the selection of a parameter α . The coupled regmentation method relies on a level sets approach along with a non-rigid deformable registration technique using an adaptive meshing selection of control points for the segmentation and registration procedures, respectively. An in-house built 4D biomechanical lung phantom with synthetic lesions was used to evaluate this specific type of algorithm's performance. We investigate the optimal use of regmentation parameters within this work. An

improvement in segmentation accuracy and registration accuracy within the local region of the segmentation targets was found using a coupling coefficient of 0.55. Values of $\alpha_1 = 0.7$ and $\alpha_2 = 0.5$ were determined to be optimal for the registration and segmentation tasks, respectively. Additionally, the regmentation algorithm was also compared to a Lucas-Kinade optical flow and Demons registration algorithm using a variety of signal-to-noise (SNR) values which were created using artificially produced computed tomography (CT) noise. A reduction in target registration error (TRE) of 4% between 36 and 6.8 dB was observed for the regmentation algorithm compared to 24% and 30% for the optical flow and Demons algorithm. Our work has shown improvement in registration and segmentation accuracy attained through the coupling of the two methods and have demonstrated a robustness to noise compared to alternative deformable registration algorithms.

5.2 Introduction

The practice of adaptive radiotherapy (ART) attempts to take into account anatomical changes that occur during the course of fractionated radiotherapy. These may include, but not limited to, tumor size and shape, weight gain or loss, the filling or voiding of hollow organs such as the bladder or even movement during the treatment itself. Many of the tools ART employs include use of resegmentation, registration and re-optimization. In the last 20 years, partial implimentation of ART practices into the clinic have been aided through the advancement of computing power, in-room imaging devices and treatment planning techniques [80, 152, 153]. The practicality of ART is dependant upon the efficiency of the replanning process. Automated and semi-automated segmentation and registration software has been

demonstrated to significantly reduce replanning time and observer variability [154, 155, 156].

Regmentation is the process of simultaneously combining segmentation with registration with the intent of improving the accuracy and efficiency of both processes [157, 101]. With regards to adaptive radiotherapy (when the target is found within the lung) and in particular when leveraging multimodal imaging for plan adjustment several challenges are present.

- Proper re-segmentation of the target boundary in the presence of noise and weak boundaries
- Registration of data sets with low image quality, particularly for MRI images of the lung or using cone-beam CT.
- Segmentation of unregistered data from multiple modalities.

Many commercial applications incorporate an atlas to aid in segmentation of OARs and treatment targets [154]. This technique requires the registration of an atlas volume to the applied image to segment desired structures but often does so sequentially. Several experimental methods have applied the two in a joint fashion [120, 121, 122], however, the registration component only serves in the final production of a contour. An integrated segmentation and registration framework was first proposed by Bensal et al. [123] where a 2D portal image was rigidly registered to a 3D CT volume using an entropy based objective function. Yezzi in 2001 [124] using a variational segmentation method along with a rigid registration of the level set functions in order to couple the two processes. Since then several more advanced joint algorithms have been published [125][126].

Gooya et al. [122] used an estimation maximization algorithm to simultaneously register and segment skull stripped MR images with a brain atlas. Xue et al. [125] used a 4-D elastic deformable registration in step with a custom temporal clustering algorithm to perform regmentation of 4-D CT images. Ayvaci et al. [126] combined registration into the segmentation of CT images using a template combined with a graph cuts method. A watershed filter was used to simplify the graph-cuts segmentation by only considering discrete homogenous regions.

The proposed algorithm derives from previous work using the Jensen Rényi divergence as an optimization criteria for a level sets segmentation technique [158]. The Jensen Rényi objective function showed an improved robustness to noise compared to a similar technique using mutual information. The proposed implementation combines registration with segmentation through the use of a coupling term that seeks to optimize the energy function of the segmentation through movement of the control points, aligning the reference image in the proximity of the contour boundary. Additionally the flexibility of this theoretical framework allows the inclusion of any number of volumes and thus can be used to perform temporal multimodal joint registration/segmention.

5.3 Materials and Methods

5.3.1 Theoretical Background

The Jensen Rényi Divergence

Let us define a set of samples from either outside or inside a contour by x_i , i = 1, 2, ...n where n is the sample size and i is the sample index. Using these samples to

define the probabilistic intensity distributions inside and outside, the JR divergence criterion is defined by the following conditional expectation:

$$E(\theta) = \frac{1}{1-\alpha} \left(\log \int_{\Re} (w_1 P_1(J(x), \Omega) + w_2 P_2(J(x), \Omega))^{\alpha} dx - w_1 \log \int_{\Re} (P_1(J(x), \Omega))^{\alpha} dx - w_2 \log \int_{\Re} (P_2(J(x), \Omega))^{\alpha} dx \right)$$
(5.1)

where w_1, w_2 are the weighting parameters for the probability distribution functions P_1 and P_2 . P_1 and P_2 in this context are defined by the intensity distributions inside and outside the evolving level set, respectively. The symbol \Re covers the domain of possible intensity values. For our implementation, volumes were discretized to 55 levels in order to reduce processing requirements. A higher number of levels was found to be too memory intensive for the hardware the algorithm was run on, which included 3GB of GPU ram on an nVidia GeForce GTX 560M. The geometric space Ω varies depending on the task. For segmentation Ω_- and Ω_+ define the sample space inside and outside the contour boundary respectively. For registration Ω defines the volumes enclosed within the tetrahedra connected to the control point in question. The curvature of the energy function is determined by the choice of parameter α which determines the weighting of infrequently versus frequently occurring intensity values. This has been shown to be an effective method for dealing with noise where the noise contributes to values outside the expected distribution [73]. When is equal to 0.5, the divergence is proportional to the log of the Bhattacharyya

coefficient. When α is chosen to be 1 the measure becomes the Jensen-Shannon divergence, which is equivalent to mutual information when the weighting parameters are chosen equal to P_1 and P_2 .

The probability distributions are defined using Gaussian kernels.

$$P(J(x), \Omega) = \frac{1}{n} \sum_{i=1}^{n} K_{\psi} (J(x) - J(x_i))$$
 (5.2)

$$K_{\psi}(z) = (2\pi)^{-p/2} |\psi|^{-1/2} \exp\left(-\frac{1}{2} (z)^{T} \psi^{-1}(z)\right)$$
(5.3)

Here n defines the number of samples, z the input vector and p represents the dimensionality of the inputs for the probability density. For example when performing registration the dimensionality p is 2 since the inputs are defined by the reference and target image. Additionally, K_{ψ} is the Gaussian kernal used for the Parzen window estimation of the probability density. Here ψ represents the covariance matrix of the feature vector J. This can be calculated be directly from the vector J, however this makes the assumption that the data is best represented by two unimodal distributions. Since we want to make no assumptions about the shape of the distributions, every covariance matrix was set as a $p \times p$ matrix with every diagonal element set to 8.

A flow chart is shown in Figure 5–1 outlining the steps of the overall algorithm.

Segmentation Using Level Sets

The application of the Jensen Rényi divergence as an energy function for use in level sets segmentation and non-rigid deformable registration is outlined here. Both

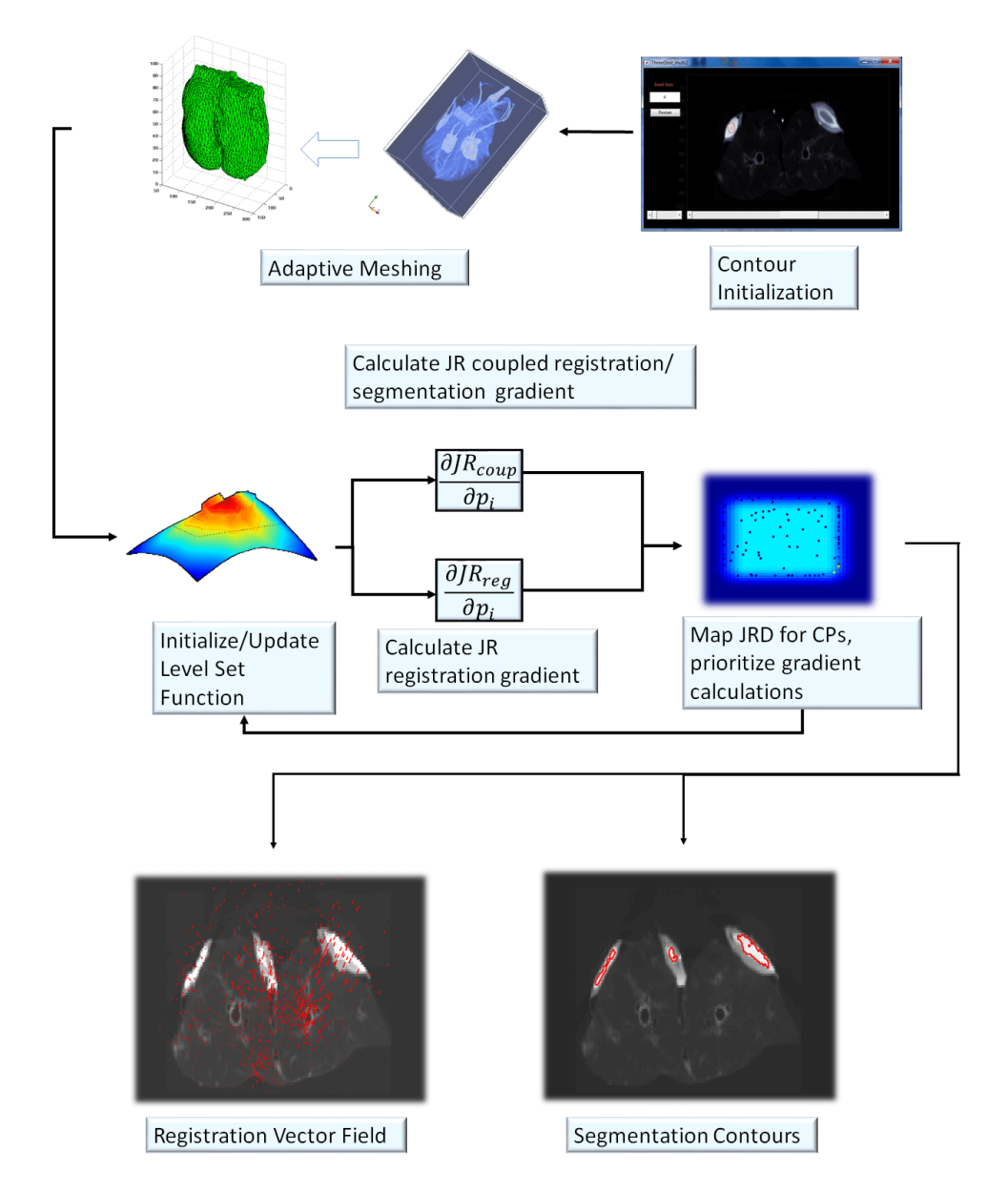


Figure 5–1: An outline of the algorithm highlighting the adaptive mesh generation using a 3D Floyd-Steinberg dithering filter and the iso2mesh package for mesh creation. The level set segmentation function is updated by calculating the gradient of the JR divergence with respect to raising or lowering the level set function. The iterative update to the deformation vectors is calculated from the regular registration gradient and a coupling term which applies deformation vectors in order to better align the image in the local region surrounding the segmentation target.

processes are optimized using a gradient descent technique. This is outlined for calculating the update to a level set function for segmentation, the position of the registration control points and similarly the control points that belong to elements that overlap with the contour when calculating the coupling term. The level set function is an implicit contour representation that use a scalar function, $\phi(x, y, z)$ overlayed on the image space where the contour is defined by the zero crossing $(\phi(x, y, z) = 0)$. As defined in our previous work [158] the energy function is of the form in Equation 5.4.

$$E(\phi) = \int_{\Omega} (JRD(\phi(x)) + \mu |\nabla H(\phi(x))| - \nu) dx$$
 (5.4)

Where $JRD(\phi)$ is the Jensen Rényi divergence, ν is a scalar velocity term, dx is a euclidean voxel coordinate represented by x, Ω is the set of sampled voxels in the image, $|\nabla H(\phi)|$ is the magnitude of the gradient of the Heaviside function (which forces a smooth boundary) and μ is a weighting factor controlling the roundness of the contour. Growth and shrinkage of the contour is controlled through raising and lower of the level set function and is inhibited by the velocity term ν .

The level set function of the segmentation algorithm is evolved by the following derivation

$$\frac{\partial E(J(x), \theta)}{\partial C} = \frac{1}{1 - \alpha} \left(\frac{\int_{\Re} \alpha \left(w_1 P_1 + w_2 P_2 \right)^{\alpha - 1} \left(w_1 \frac{\partial P_1}{\partial C} + w_2 \frac{\partial P_2}{\partial C} \right) dx}{\int_{\Re} \left(w_1 P_1 + w_2 P_2 \right)^{\alpha} dx} - w_1 \frac{\int_{\Re} \alpha P_1^{\alpha - 1} \frac{\partial P_1}{\partial C} dx}{\int_{\Re} P_1^{\alpha} dx} - w_2 \frac{\int_{\Re} \alpha P_2^{\alpha - 1} \frac{\partial P_2}{\partial C} dx}{\int_{\Re} P_2^{\alpha} dx} \right)$$
(5.5)

Where P_1 and P_2 is a simplified notation of $P_1(J(x), \Omega_-)$ and $P_2(J(x), \Omega_+)$. The partial derivatives of the probability densities are

$$\frac{\partial P_1}{\partial C} = \frac{1}{|\Omega_-|} \left(-K_{\psi_1}(J(C) - J(x)) - P_1(J(x), \Omega_-) \right)$$
 (5.6)

$$\frac{\partial P_2}{\partial C} = \frac{1}{|\Omega_+|} \left(P_2(J(x), \Omega_+) - K_{\psi_2}(J(C) - J(x)) \right) \tag{5.7}$$

where C refers to voxel samples in the local region around the edge of the contour.

5.3.2 Adaptive Meshing

In order to reduce the number of control points needed to register two images, an adaptive meshing approach was implemented in order to more efficiently place control points in areas of high information content (such as high contrast borders) while reducing the control point density in homogenous regions. This is accomplished through the use of the Floyd-Steinberg dithering filter [159]. Dithering is a technique originally developed for newsprint in order to convey gray scale when the only options available for printed were a binary ability to place ink or leave the page blank. By regulating the density of dots, shades of gray can be conveyed to the human eye at a larger scale. A dithering filter is a method of transforming a grayscale image into a binary one without the loss of conveyed shade as shown in Figure 5–2. Our implementation begins by determining a mask that encompasses the object of interest, in this case the lungs through simple thresholding. The iso2mesh package developed by Qianqian Fang [160] was used to convert the binary mask into an outer shell mesh for the lungs. Due to the fact that the iso2mesh package deals exclusively

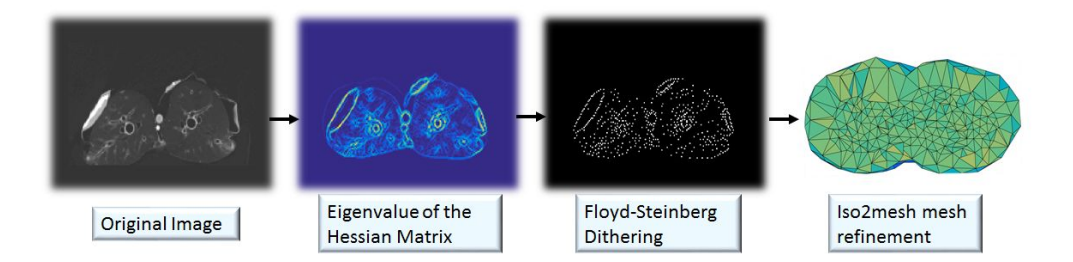


Figure 5–2: Adaptive meshing pipeline beginning with uing the eigenvalue of the Hessian matrix to exemplify image features. The Floyd-Steinberg dithering filter is used to determine the locaton of points which after randomly selecting can be used to produce a 3D mesh.

with presegmented image volumes, the Floyd Steinberg dithering filter was used to extract control point locations. The input to the filter was the first eigenvalue of the Hessian matrix derived for each voxel in the image. To control the total number of control points, the control points generated from the dithering filter were selected using a randomized permutation and checked to ensure that they fell outside of a user-defined radius of any other previously chosen control points. This simple method regulated the size of the final tetrahedra created in the mesh. These chosen control points were then added to the initial mesh shell using the mesh refinement tool included in iso2mesh.

Registration

The overall energy criteria for the registration process is presented as a combination of the registration and coupling term. The coupling term is zero for most control points unless they are part of an element overlapping with the contour. The control point positions are defined by $[p_x, p_y, p_z]$.

$$\frac{\partial p_i}{\partial t} = \int_{\Omega} \frac{\partial JR_{reg}(p_x, p_y, p_z)}{\partial p_i} + C \frac{\partial JR_{coup}(p_x, p_y, p_z)}{\partial p_i} dx + S_i(p_x, p_y, p_z)$$
(5.8)

In this formulation i refers to any one of the dimensions x, y or z (in 3D) while the regularization term is represented by S_i to ensure a smooth vector field and t is the time step. The function S_i in this implementation represents a Gaussian smoothing function using Equation 5.9, where d_i is the distance between the current control point (p_x, p_y, p_z) and an adjacent control point indexed by i.

$$S(p_x, p_y, p_z) = \frac{1}{3} \sum_{i}^{n} p_i \frac{\frac{1}{r\sqrt{2\pi}} \exp{-\frac{d_i^2}{2r^2}}}{\sum_{j}^{n} \frac{1}{r\sqrt{2\pi}} \exp{-\frac{d_j^2}{2r^2}}}$$
(5.9)

In this context r represents a radius parameter set by the user which scales the distance of influence for each of the control points. The variable n represents the collection of control points connected to $[p_x, p_y, p_z]$ through the mesh structure.

The registration force is calculated from Equation 5.10 where P_1 represents the probability of an intensity value belonging to the distribution of the target image and P_2 the reference image. Since moving the control points only deforms the reference image, finding the gradient requires taking the derivative with respect to P_2 .

$$\frac{\partial JR_{reg}}{\partial t} = \frac{\alpha}{1 - \alpha} \frac{\int_{\Re} \left(w_1 P_1 \left(J(x), \Omega \right) + w_2 P_2 \left(J(x), \Omega \right) \right)^{\alpha - 1} w_2 \frac{\partial P_2 \left(J(x), \Omega \right)}{\partial t} dx}{\int_{\Re} \left(w_1 P_1 \left(J(x), \Omega \right) + w_2 P_2 \left(J(x), \Omega \right) \right)^{\alpha} dx} - w_2 \frac{\int_{\Re} \left(P_2 \left(J(x), \Omega \right) \right)^{\alpha - 1} \frac{\partial P_2 \left(J(x), \Omega \right)}{\partial t}}{P_2 \left(J(x), \Omega \right)^{\alpha} dx} \tag{5.10}$$

Applying the chain rule, the derivative of P_2 is calculated using the Guassian kernel from Equation 5.2 to produce Equation 5.11.

$$\frac{\partial P_2(J(x), \Omega)}{\partial t} = \sum_{x_i \in A} (2\pi)^{-\frac{p}{2}} |\psi|^{-\frac{1}{2}} (J(x) - J(x_i))^T \psi^{-1} \cdot \left(\frac{\partial J(X_i)}{\partial t}\right) exp\left(-\frac{1}{2} (J(x) - J(x_i))^T \psi^{-1} (J(x) - J(x_i))\right)$$
(5.11)

Where $(J(x), \Omega) \partial t$ is calculated from Equations 5.23, 5.24, 5.25 and 5.25. For the coupled metric, the inputs are multi-dimensional (from each image) and thus for the simplest case of two images, it is defined by

$$\frac{\partial J((x,\Omega)}{\partial t} = \left(\frac{\partial u(x_i)}{\partial t}, \frac{\partial v(x_i)}{\partial t}\right) \tag{5.12}$$

Further derivations regarding the gradient terms including the coupled gradient definition are presented in the appendix.

The mapping function is outlined in a paper by Wang et al. [161] which uses any mesh comprised of triangular elements. The 3D extension, using tetrahedrons, is outlined in the appendix (see Equation 5.29. The forward mapping function can be represented in the affine form

$$w_m^t(u) = \begin{bmatrix} a_1 + a_2s + a_3t \\ b_1 + b_2s + b_3t \end{bmatrix}$$
 (5.13)

where the coefficients are calculated from the control point coordinates of the element vertices ([x1,y1],[x2,y2] and [x3,y3]) in the reference space.

$$\begin{bmatrix} a_1 \\ a_2 \\ a_3 \end{bmatrix} = \begin{bmatrix} x_3 \\ x_1 - x_3 \\ x_2 - x_3 \end{bmatrix}$$
 (5.14)

$$\begin{bmatrix} b_1 \\ b_2 \\ b_3 \end{bmatrix} = \begin{bmatrix} y_3 \\ y_1 - y_3 \\ y_2 - y_3 \end{bmatrix}$$
 (5.15)

The Jacobian of this mapping function is

$$A_m = a_2b_3 - a_3b_2 = x_1y_2 + x_2y_3 + x_3y_1 - y_1x_2 - y_2x_3 - y_3x_1$$
 (5.16)

5.3.3 4D Phantom Based Evaluation

A 4D biomechanical phantom (shown in Figure 5–3) was produced in house in order to provide a dataset with a well known yet realistic ground truth. A Bioquest preserved swine lung was used as the tissue phantom due to its similarity to human lungs and MR compatibility. The ground truth for segmentation is provided by a dual-compartment vacuum sealed natural sea sponge. Each compartment is accessible through rubber tubing attached to a Microclave connector (ICU Medical Inc, San Clemente, CA). Figure 5–4 shows an example of the synthetic tumor compartments. The inner compartment acts as the target with the surrounding outer compartment as the background.

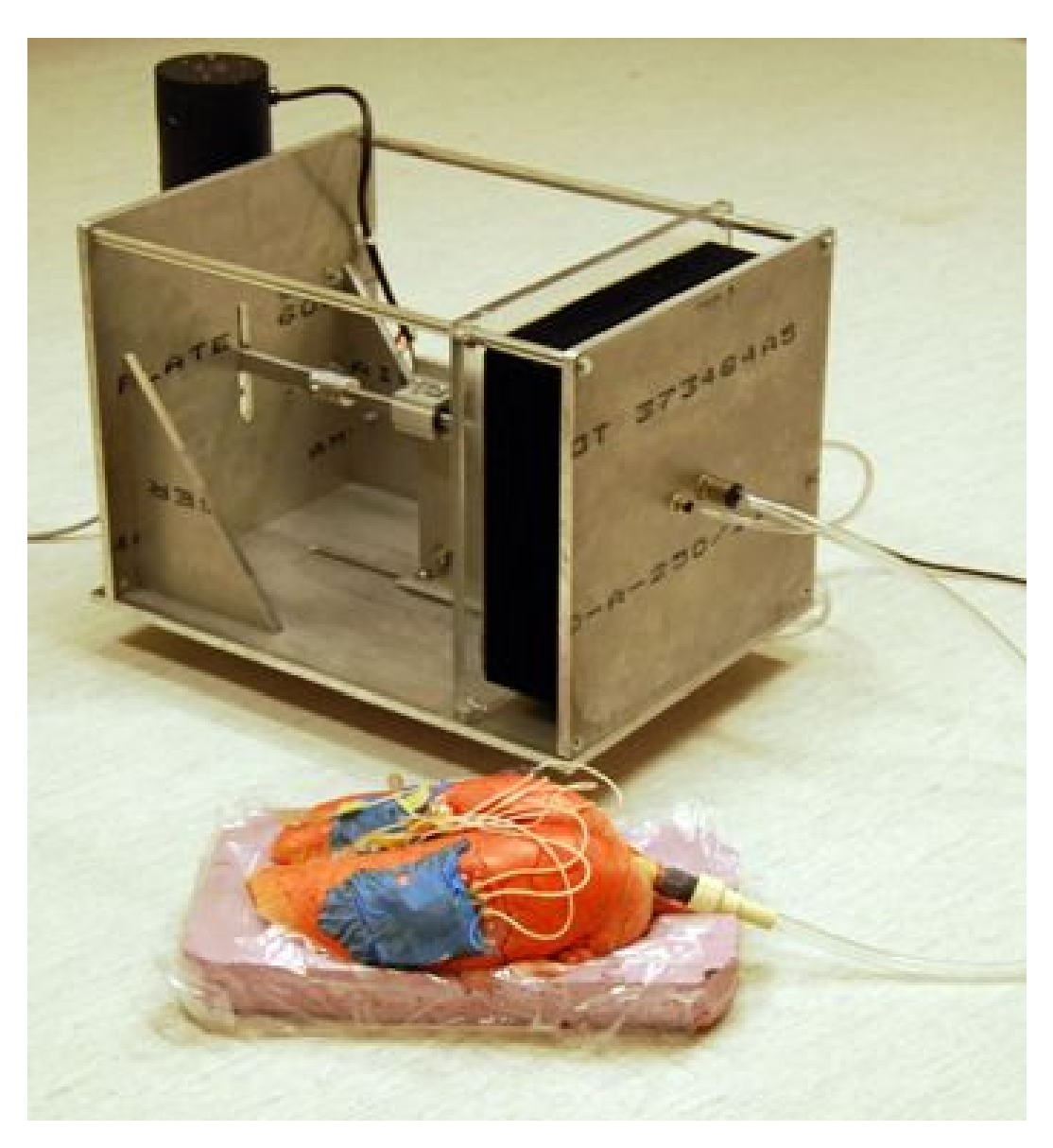


Figure 5–3: Photo of the computer controlled respirator connected to the preserved swine lungs. A 186 watt motor is used to manipulate the rubber bellows at the end, inflating and deflating the lungs.



Figure 5–4: Photo of the synthetic tumor consisting of multiple vacuum sealed compartments.

The registration ground truth is provided by the bifurcations of the bronchi of the lungs which act as anatomical landmarks for comparison. A bifurcation tracking pipeline was created to automatically detect and match congruent bifurcations between two datasets. The pipeline first segments the bronchial tree of the lungs using region growing with the seed planted in the airway of the bronchi. Following this a 3D skeletonization procedure is used to reduce this binary image to a 1 voxel thick medial axis that runs through the center of the bronchi as shown in Figure 5–5.

The skeleton is used to determine where bifurcations occur by using a 3D extension of the rotationally invariant masks used by Bhuiyan et al. [162]. A library of 3264 3x3x3 voxel neighbourhood templates of possible patterns was used to detect bifurcations in the skeleton. The templates were compared to 3x3x3 voxel neighbourhoods in the binary mask of the skeleton that contained exactly 4 voxels belonging

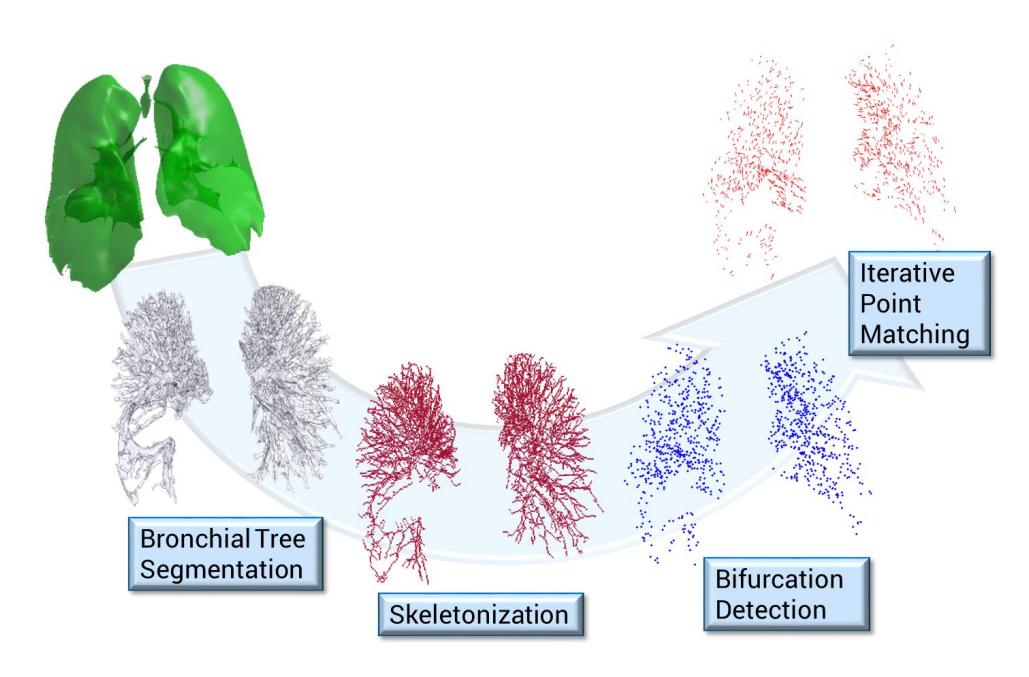


Figure 5–5: The bifurcation pipeline used to provide a ground truth for registration evaluation.

to the skeleton. Once bifurcations are detected in the target and reference images, they're matched by first determining an appropriate rigid transormation. The transformation is estimated using fuzzy clustering to determine cluster centers of the bifurcation point clouds of each lung in both images. After rigidly translating the reference point cloud, a modified version of the thin plate spline robust point matching algorithm[163] written by Jinzhong Yang in 2011 [41], was used to match point pairs. The algorithm uses a non-rigid transformation to match point clouds and allows for an unequal number of points in each set. A user interface was developed to present the results to the user as a final verification of the candidate point pairs, allowing the user to accept, reject or re-match them.

The lungs were controlled pneumatically using a computer controlled in-house respirator with the ability to provide highly custom breathing profiles. The breathing profiles themselves were traced from patient breathing data taken during CT simulation using a pneumatic belt (Philips Medical Systems, Cleveland, OH, USA). The respirator is connected to the lungs via a 7.6 m long PVC tube which runs into the scan room.

5.3.4 Noise Simulation

Noise was artificially added to CT images of the lung using a simplified technique similar to the technique published by Massoumzadeh et al. [164] involving the following steps.

• Export data from CT scanner

- Convert Hounsfield units to units of linear attenuation coefficient under the assumption of a monenergetic photon source matching the average energy of the CT energy spectrum.
- Produce sinograms of the volume using the radon transform.
- Convert the sinograms units to those linearly scaled to flux.
- Additional noise is added to the sinogram by generation of Poisson distributed noise with a mean value equivalent to the flux values contained within the sinogram. An multiplicative amplitude coefficient is added here to the mean value in order to manually scale the final noise variance.
- Using the new noisier sinogram, convert back to units of integrated linear attenuation coefficients and reconstruct the images using inverse radon transforms and a Ram-Lak filter.
- Convert back to Hounsfield Units.

The listed approach ignores a number of factors such as beam current, collimation area and the detector noise variance due to the presence of a bowtie filter. Since our goal was to observe the effects of lower SNR CT scans on algorithm performance we deemed the simplified method sufficient. The resulting images are shown in Figure 5–6.

5.3.5 Sensitivity Analysis

The dependency of registration and segmentation accuracy on three key parameters was investigated in this work. The coupling parameter c, the α term within Equation 5.1 and the contrast and noise characterized by the signal to noise ratio.

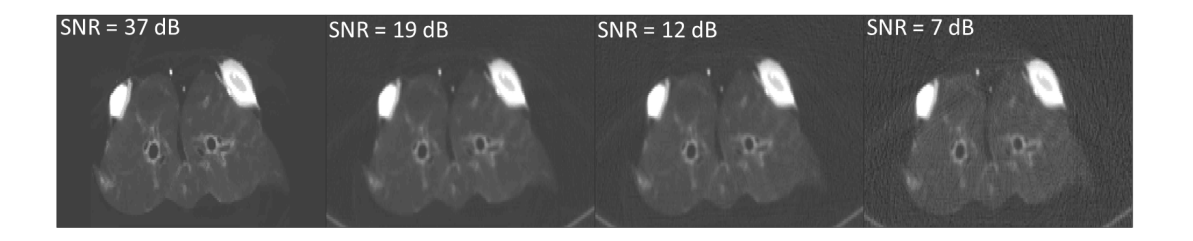


Figure 5–6: Examples of the addition of artificial noise to the CT volumes for varying SNR values.

Alpha Dependency

In our previous work [158] we determined that the most appropriate α value is highly modality dependant and thus appropriate values were discerned for the modality combinations tested. A similar tuning had to be performed here, the results of which are shown in Figure 5–7.

Figure 5–7 was collected with the assumption that the chosen α used for the registration term of Equation 5.8 was equal to that used during the segmentation phase. Preliminary results showed that segmentation accuracy was not optimized by the same α value used during the registration step. As such two α values were used to mitigate this divergent relationship. Figure 5–8 shows the results of the parameter space search using the Dice Similarity Coefficient (DSC) with the segmentation ground truth as the figure of merit.

An α_2 of 0.5 was found to optimize the segmentation results for targets 1 and 2 while the performance of target 3 increased slightly past 0.5 up to 0.65.

5.3.6 Coupling Dependency

Figure 5–10 demonstrates the relationship between target registration accuracy (TRE) and the coupling parameter C shown in Equation 5.8. TRE was measured

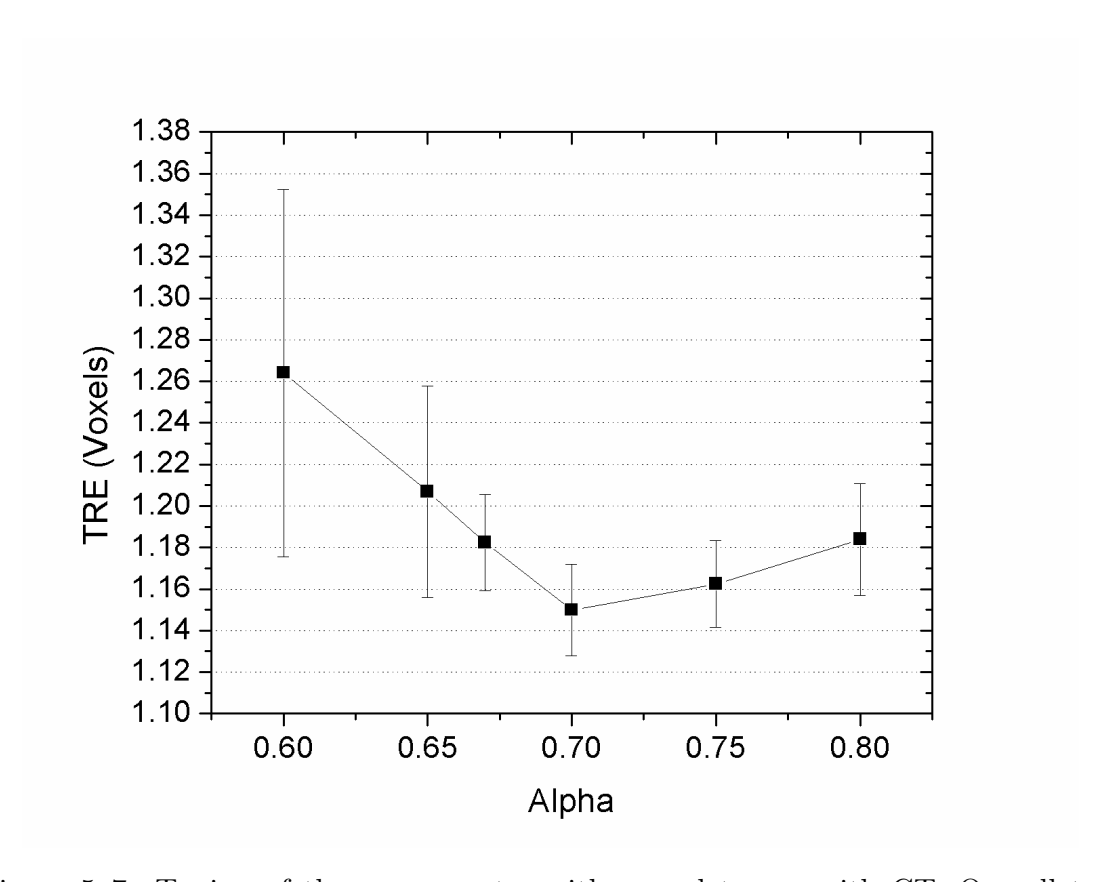


Figure 5–7: Tuning of the α parameter with regard to use with CT. Overall target registration was minimized with a value of 0.7. Error bars represent the 95% confidence interval.

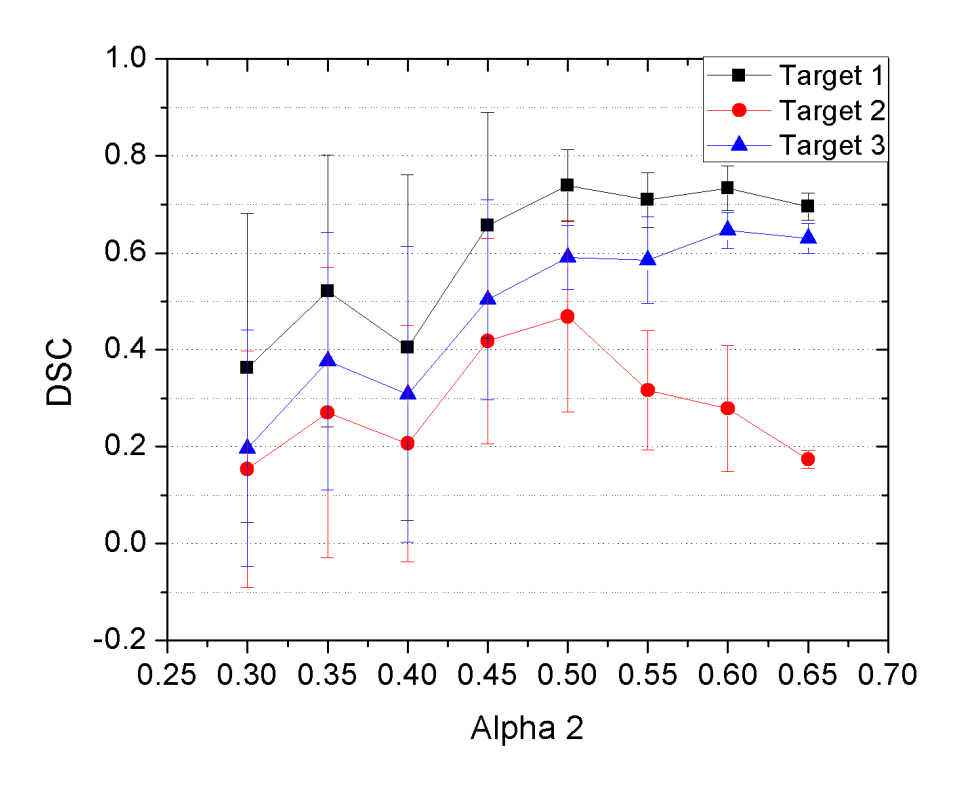


Figure 5–8: Tuning of α_2 the seperate α value applied solely to the segmentation step of the regmentation process. Error bars represent the standard deviation across 10 trials for each data point.

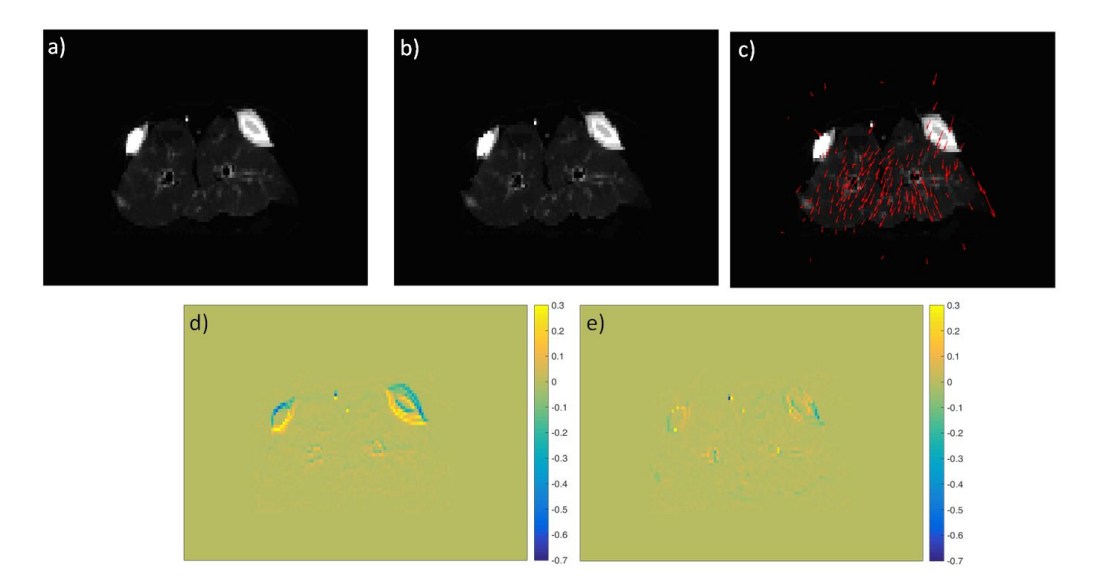


Figure 5–9: Example of the registration performed on the lungs at two adjacent phases of breathing. Shown is a)the reference image, b) the deformed reference image and c)the deformed image along with the registrations vectors in proximity to that slice. Also shown is d) the difference image between the reference and target images before registration and e) following registration.

from the mean difference in voxel units between the ground truth vector field and that calculated by the JR regmentation algorithm.

Each data point shown in Figure 5–10 represents the mean of registrations performed using the stated coupling parameter, an example of which is shown in Figure 5–9. Alpha was kept constant at 0.7, utilizing the information from Figure 5–7.

The TRE within the local region of the targets is plotted along with the overall TRE for the entire lung. A clear minimum is seen for the local TRE around a C-value of 0.55. The coupling term has an inverse relationship with the overall TRE for the entire lung. The increase in alignment accuracy around the objects being segmented comes at the cost of accuracy elsewhere in the image.

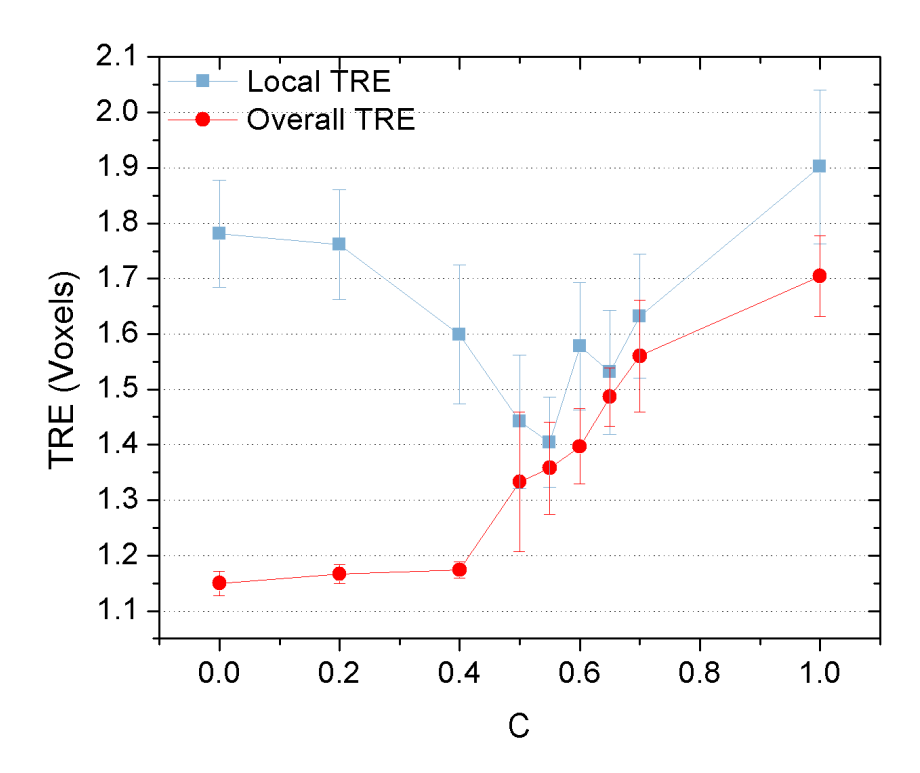


Figure 5–10: Dependancy of target registration error (TRE) on the coupling parameter within the local region of the targets being segmented and for overall lung region.

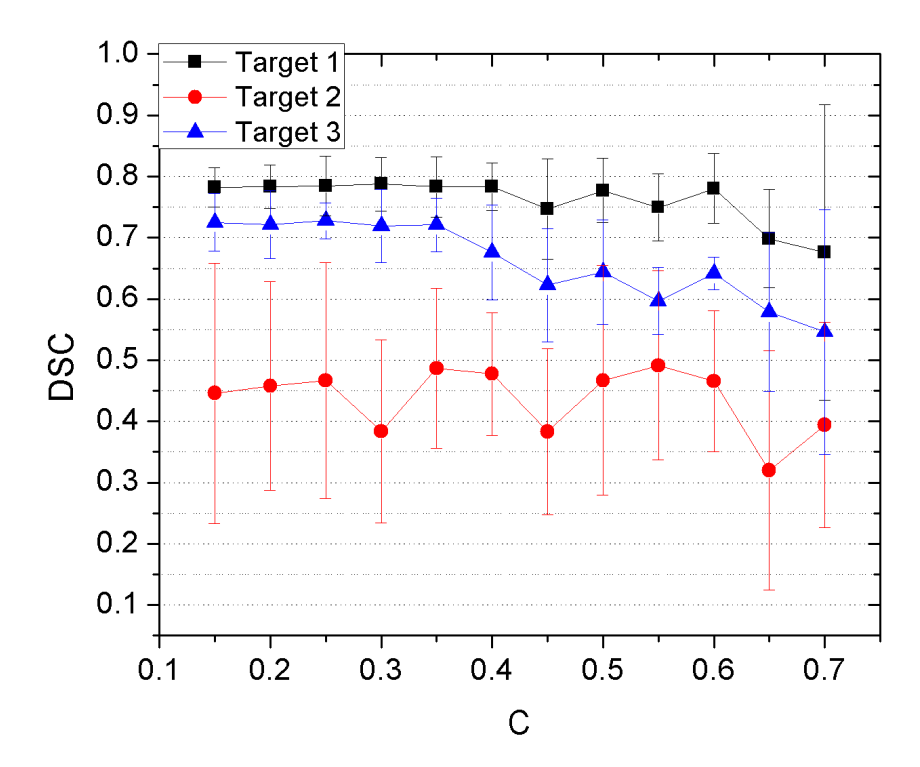


Figure 5–11: Dependency of the DSC on the coupling term C for the three targets within the biomechanical phantom.

The segmentation accuracy unfortunately does not show a distinct relationship to the coupling term as shown in Figure 5–11.

A modest curve can be seen for target 2 which reaches a maximum at C=0.55, which is in agreement with the results of Figure 5–10. The DSC of targets 1 and 3 remain relatively stable up until C=0.6 where they then begin to decline.

SNR Dependancy

As previous literature has reported upon the relationship between the Jensen Rényi divergence and the signal to noise ratio [73] this was also evaluated using the

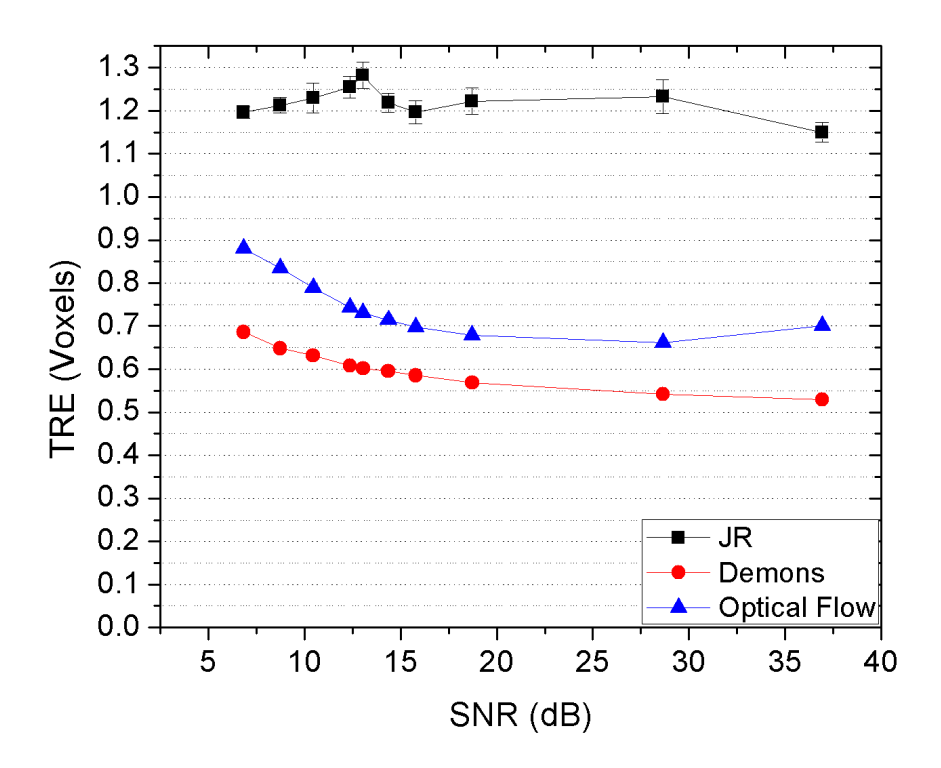


Figure 5–12: Dependency of the JR regmentation method compared to the Demons algorithm and Lucas-Kinade optical flow method for various SNR values.

lung phantom. Figure 5–12 summarizes the registration results using the Jensen Rényi based regmentation algorithm (C=0.55, $\alpha=0.7$) using the lung phantom for a variety of simulated noise images. The proposed algorithm was compared to two alternative registration algorithms, an implementation of the Lucas-Kinade optical flow method or non-rigid registration [165] and an alternative Demons implementation using a multi-resolution pyramid approach included in Matlab 2015a (The Mathworks, Inc., Natick, MA).

Figure 5–12 shows an increase in TRE of 26%, 30% and 4% for the optical flow, demons and JR regmentation method respectively when decreasing the SNR from 37 to 6.8 dB. The overall TRE for the JR regmentation method is however consistently higher than the other two methods.

5.4 Discussion

This works presents the joint coupling of segmentation and registration processes using the Jensen Rényi divergence in order to investigate optimal parameter choices for α and C along with a characterization of response to increased artificial noise. The proposed method has direct applications to adaptive radiotherapy planning and has the potential to improve replanning efficiency and robustness.

Using an in-house built phantom along with synthetic lesions and a software pipeline for bifurcating tracking of the lung airways we were able to evaluate both the segmentation and registration accuracy under varying SNR and parameter values. For CT regmentation an optimal α value of 0.7 was found to maximize the registration accuracy where as the optimal α_2 parameter to use for the segmentation step was not as clear. A value of 0.7 lies close to the recommended value of 0.85 found during our previous work [158] for CT. Considering that a different subject was being scanned along with a different application (registration versus segmentation) this is not surprising. We also note that a systematic parameter search was not presented in our earlier work. We saw that segmentation accuracy was maximized for targets 1 and 2 at a value of $\alpha_2 = 0.5$ which also differs from earlier results. When discussing this value it is also important to consider that there is a more complex interplay at work as the segmentation accuracy affects the registration accuracy and vice versa.

Optimization of the coupling parameter, demonstrated in Figures 5–10 and 5–11 was found to be less complex with an optimal value found at C=0.55 for both registration and segmentation tasks. The dependency of segmentation accuracy on C shown in Figure 5–11 was much less pronounced with the largest variation shown by target 2. This is unsurprising as it contained the smallest active compartment of the three and would thus be more susceptible to registration errors.

When investigating the effect of CT noise on registration performance we found a significant reduction in TRE for the Lucas-Kinade optical flow and Demon algorithms on the order of 26% and 30% respectively compared to the case when no artificial noise was added. While the overall TRE was worse for the JR regmentation algorithm the performance was remarkably resilient to added noise with a TRE reduction of only 4%. This would agree with previously published results regarding the use of the Jensen Rényi divergence [73, 158]. The difference in TRE between the JR regmentation algorithm and the other two algorithms can be attributed to the choice of a dense control selection scheme and our adaptive approach along with a less advanced regularization technique. Unfortunately, the sampling requirements of our algorithm prevent the use of a dense selection approach (where every voxel is a control point), not to mention that such a high density would make gradient calculations prohibitively intensive.

While the phantom used in this work is used to simulate different target sizes, arrangements, deformation magnitudes and noise conditions, evaluation (even if subpar) on a clinical dataset is necessary. This will highlight glaring differences in performance and confirm the performance of the algorithm in a clinical context.

5.5 Conclusions

We have presented a framework for coupling a level sets segmentation algorithm with a non-rigid deformable registration algorithm using the Jensen Rényi statistical divergence metric. With the use of a custom biomechanical phantom made specifically to simultaneously evaluate joint segmentation/registration algorithms, we optimized the choice of parameters α and the coupling coefficient C. Values of $\alpha = 0.7$ for registration and $\alpha_2 = 0.5$ for segmentation were found to maximize the registration and segmentation accuracy respectively. A coupling coefficient of 0.55 was determined to also minimize the local registration accuracy surrounding the targets being segmented and maximize segmentation accuracy. The regmentation algorithm was also compared to a Lucas-Kinade optical flow and Demons registration algorithm and despite showing a higher overall TRE, was found to exhibit significantly less (4% compared to 24% and 30% for the optical flow and Demons) variance in TRE for SNRs as low as 6.8.

5.6 Acknowledgements

The authors would like to acknowledge Paul Gravel and Stephane Frenette of the PERFORM Centre at Concordia University for their work in scanning and reconstructing the 4D scans of lung phantom.

5.7 Appendix

5.7.1 Continuing the 2D Case

The coupled metric is defined here by Equation 5.18 where in this case P_1 and P_2 represent the probability of a sample belonging to the inside and outside of the contour respectively. Since each distribution relies on the two-dimensional sample

from the reference and target image, they're both influenced by movement of the control points and hence both are treated as variables in the derivation.

$$\partial JR_{coup}(\theta)/\partial t = \frac{1}{1-\alpha} \frac{\int_{\Re} \alpha(w_1 P_1(J(x),\Omega) + w_2 P_2(J(x),\Omega))^{\alpha-1} \left(w_1 \frac{\partial P_1(J(x),\Omega)}{\partial p} + w_2 \frac{\partial P_2(J(x),\Omega)}{\partial p}\right) dx}{\int_{\Re} (w_1 P_1(J(x),\Omega) + w_2 P_2(J(x),\Omega))^{\alpha} dx} - \frac{1}{1-\alpha} w_1 \frac{\int_{\Re} \alpha P_1(J(x),\Omega)^{\alpha-1} \frac{\partial P_1(J(x),\Omega)}{\partial p} dx}{\int_{\Re} P_1(J(x),\Omega)^{\alpha} dx} - \frac{1}{1-\alpha} w_2 \frac{\int_{\Re} \alpha P_2(J(x),\Omega)^{\alpha-1} \frac{\partial P_2(J(x),\Omega)}{\partial p} dx}{\int_{\Re} P_2(J(x),\Omega)^{\alpha} dx}$$

$$(5.17)$$

In this formulation, J is a two dimensional list of voxel intensity samples from each image $[J_1, J'_2]$. In this case J'_2 is the transformed reference image. In Equation 5.18 $w_{1,m}$ and $w_{2,m}$ refer to the forward and inverse mapping functions to and from the master domain $D_{2,m}$.

$$J_2'(p) = J_2(w_{1,m}(w_{2,m}(p))), p \in D_{2,m}$$
(5.18)

The partial derivative then becomes

$$\frac{\partial J_2'(p)}{\partial p} = \nabla J_2\left(w_{1,m}\left(w_{2,m}(p)\right)\right) \frac{\partial w_{1,m}\left(w_{2,m}(p)\right)}{\partial p}$$
(5.19)

The forward mapping functions shown here are were defined earlier in Equation 5.13, while the Jacobian A_m of Equation 5.16 is used to simplify the inverse mapping

function defined by inverting Equation 5.13.

$$w_m^{-1}(u) = \begin{bmatrix} \xi_m^{-1} \\ \eta_m^{-1} \end{bmatrix} = \frac{1}{A_m} \begin{bmatrix} (x_2y_3 - x_3y_2) + (y_2 - y_3)x + (x_3 - x_2)y \\ (x_3y_1 - x_1y_3) + (y_3 - y_1)x + (x_1 - x_3)y \end{bmatrix}$$
(5.20)

$$\begin{bmatrix}
\frac{\partial J_{1}(w_{1,m}(w_{2,m}^{-1}(p)))}{\partial x_{1}} \\
\frac{\partial J_{1}(w_{1,m}(w_{2,m}^{-1}(p)))}{\partial y_{1}}
\end{bmatrix} = \begin{bmatrix}
\frac{\partial J_{1}(w_{1,m}(w_{2,m}^{-1}(p)))}{\partial w_{1,m}(w_{2,m}^{-1}(p))} \cdot \frac{\partial w_{1,m}(w_{2,m}^{-1}(p))}{\partial x_{1}} \\
\frac{\partial J_{1}(w_{1,m}(w_{2,m}^{-1}(p)))}{\partial w_{1,m}(w_{2,m}^{-1}(p))} \cdot \frac{\partial w_{1,m}(w_{2,m}^{-1}(p))}{\partial y_{1}}
\end{bmatrix} (5.21)$$

To simplify notation, let us refer to $w_{1,m}\left(w_{2,m}^{-1}(p)\right)$ as $[w_x,w_y]$ from now on.

$$\begin{bmatrix} \frac{\partial w_x}{x_1} \\ \frac{\partial w_x}{y_1} \end{bmatrix} = \begin{bmatrix} a_2 \frac{\partial \xi_m^{-1}(x,y)}{\partial x_1} + a_3 \frac{\partial \eta_m^{-1}(x,y)}{\partial x_1} \\ a_2 \frac{\partial \xi_m^{-1}(x,y)}{\partial y_1} + a_3 \frac{\partial \eta_m^{-1}(x,y)}{\partial y_1} \end{bmatrix}$$

$$= \begin{bmatrix} a_2 \frac{-\xi_m^{-1}(x,y)(y_2 - y_3)}{A_m} + a_3 \left(\frac{(y - y_3)}{A_m} - \frac{\eta_m^{-1}(x,y)(y_2 - y_3)}{A_m} \right) \\ a_2 \frac{-\xi_m^{-1}(x,y)(x_3 - x_2)}{A_m} + a_3 \left(\frac{(x_3 - x)}{A_m} - \frac{\eta_m^{-1}(x,y)(x_3 - x_2)}{A_m} \right) \end{bmatrix}$$
(5.22)

Similarly,

$$\begin{bmatrix} \frac{\partial w_y}{x_1} \\ \frac{\partial w_y}{y_1} \end{bmatrix} = \begin{bmatrix} b_2 \frac{-\xi_m^{-1}(x,y)(y_2 - y_3)}{A_m} + b_3 \left(\frac{(y - y_3)}{A_m} - \frac{\eta_m^1(x,y)(y_2 - y_3)}{A_m} \right) \\ b_2 \frac{-\xi_m^{-1}(x,y)(x_3 - x_2)}{A_m} + b_3 \left(\frac{(x_3 - x)}{A_m} - \frac{\eta_m^1(x,y)(x_3 - x_2)}{A_m} \right) \end{bmatrix}$$
 (5.23)

$$\begin{bmatrix} \frac{\partial w_x}{x_2} \\ \frac{\partial w_x}{y_2} \\ \frac{\partial w_y}{x_2} \\ \frac{\partial w_y}{y_2} \end{bmatrix} = \begin{bmatrix} a_2 \left(\frac{-\xi_m^{-1}(x,y)(y_3-y_1)}{A_m} + \frac{(y_3-y)}{A_m} \right) + a_3 \left(\frac{\eta_m^1(x,y)(y_1-y_3)}{A_m} \right) \\ a_2 \left(\frac{-\xi_m^{-1}(x,y)(x_1-x_3)}{A_m} + \frac{(x-x_3)}{A_m} \right) + a_3 \left(\frac{\eta_m^1(x,y)(x_3-x_1)}{A_m} \right) \\ b_2 \left(\frac{-\xi_m^{-1}(x,y)(y_3-y_1)}{A_m} + \frac{(y_3-y)}{A_m} \right) + b_3 \left(\frac{\eta_m^1(x,y)(y_1-y_3)}{A_m} \right) \\ b_2 \left(\frac{-\xi_m^{-1}(x,y)(x_1-x_3)}{A_m} + \frac{(x-x_3)}{A_m} \right) + b_3 \left(\frac{\eta_m^1(x,y)(x_3-x_1)}{A_m} \right) \end{bmatrix}$$

$$(5.24)$$

$$\begin{bmatrix} \frac{\partial w_x}{y_3} \\ \frac{\partial w_y}{x_3} \\ \frac{\partial w_y}{y_3} \end{bmatrix} = \begin{bmatrix} a_2 \left(\frac{-\xi_m^{-1}(x,y)(y_1 - y_2)}{A_m} + \frac{(y - y_2)}{A_m} \right) + a_3 \left(\frac{-\eta_m^{-1}(x,y)(y_1 - y_2)}{A_m} + \frac{(y_1 - y)}{A_m} \right) \\ a_2 \left(\frac{-\xi_m^{-1}(x,y)(x_2 - x_1)}{A_m} + \frac{(x_2 - x)}{A_m} \right) + a_3 \left(\frac{-\eta_m^{-1}(x,y)(x_2 - x_1)}{A_m} + \frac{(x_2 - x_1)}{A_m} \right) \\ b_2 \left(\frac{-\xi_m^{-1}(x,y)(y_1 - y_2)}{A_m} + \frac{(y - y_2)}{A_m} \right) + b_3 \left(\frac{-\eta_m^{-1}(x,y)(y_1 - y_2)}{A_m} + \frac{(y_1 - y)}{A_m} \right) \\ b_2 \left(\frac{-\xi_m^{-1}(x,y)(x_2 - x_1)}{A_m} + \frac{(x_2 - x)}{A_m} \right) + b_3 \left(\frac{-\eta_m^{-1}(x,y)(x_2 - x_1)}{A_m} + \frac{(x_2 - x_1)}{A_m} \right) \end{bmatrix}$$
 (5.25)

5.7.2 Extension to 3D

The following affine function is used to fit the forward mapping function in the 3 dimensional case.

$$\phi(s,t,u) = a_1 + a_2 s + a_3 t + a_4 u \tag{5.26}$$

with coefficients

$$\begin{bmatrix} a_1 \\ a_2 \\ a_3 \\ a_4 \end{bmatrix} = \begin{bmatrix} \psi_4 \\ \psi_1 - \psi_4 \\ \psi_2 - \psi_4 \\ \psi_3 - \psi_4 \end{bmatrix}$$
 (5.27)

$$w_m^t(u) = \begin{bmatrix} a_1 + a_2s + a_3t + a_4u \\ b_1 + b_2s + b_3t + b_4u \\ c_1 + c_2s + c_3t + c_4u \end{bmatrix}$$
(5.28)

$$M = \begin{bmatrix} a_2, a_3, a_4 \\ b_2, b_3, b_4 \\ c_2, c_3, c_4 \end{bmatrix}$$
 (5.29)

$$M^{-1} = \frac{1}{A_m} \begin{bmatrix} b_3c_4 - b_4c_3, a_4c_3 - a_3c_4, a_3b_4 - a_4b_3 \\ b_4c_2 - b_2c_4, a_2c_4 - a_4c_2, a_4b_2 - a_2b_4 \\ b_2c_3 - b_3c_2, a_3c_2 - a_2c_3, a_2b_3 - a_3b_2 \end{bmatrix}$$
(5.30)

Where
$$A_m = a_2(b_3c_4 - c_3b_4) - a_3(b_2c_4 - c_2b_4) + a_4(b_2c_3 - c_2b_3)$$

$$= (x_1 - x_4)((y_2 - y_4)(z_3 - z_4) - (z_2 - z_4)(y_3 - y_4)) - (x_2 - x_4)((y_1 - y_4)(z_3 - z_4)$$

$$- (z_1 - z_4)(y_3 - y_4)) + (x_3 - x_4)((y_1 - y_4)(z_2 - z_4) - (z_1 - z_4)(y_2 - y_4))$$

$$\begin{bmatrix} s \\ t \\ u \end{bmatrix} = A_m^{-1} \begin{bmatrix} (x - x_4)(b_3c_4 - b_4c_3) + (y - y_4)(a_4c_3 - a_3c_4) + (z - z_4)(a_3b_4 - a_4b_3) \\ (x - x_4)(b_4c_2 - b_2c_4) + (y - y_4)(a_2c_4 - a_4c_2) + (z - z_4)(a_4b_2 - a_2b_4) \\ (x - x_4)(b_2c_3 - b_3c_2) + (y - y_4)(a_3c_2 - a_2c_3) + (z - z_4)(a_2b_3 - a_3b_2) \end{bmatrix} (5.31)$$

$$\begin{bmatrix} \frac{\delta s}{\delta x_1} \\ \frac{\delta s}{\delta x_2} \\ \frac{\delta s}{\delta x_3} \\ \frac{\delta s}{\delta x_4} \end{bmatrix} = \begin{bmatrix} -s(b_3c_4 - c_3b_4)A_m^{-1} \\ [s(b_2c_4 - b_4c_2) - ((y - y_4)c_4 - b4(z - z_4))]A_m^{-1} \\ [(c_3(y - y_4) - b_3(z - z_4)) - (b_2c_3 - b_3c_2)s]A_m^{-1} \\ [s(b_2c_3 - b_3c_2 - b_2c_4 + b_4c_2 + b_3c_4 - c_3b_4) - ((y - y_4)(z_2 - z_3) - (y_2 - y_3)(z - z_4) + b_3c_4 - b_4c_3)]A_m^{-1} \end{bmatrix}$$

$$\begin{bmatrix} \frac{\delta s}{\delta y_1} \\ \frac{\delta s}{\delta y_2} \\ \frac{\delta s}{\delta y_3} \\ \frac{\delta s}{\delta y_4} \end{bmatrix} = \begin{bmatrix} (c_4(x - x_4) - a_4(z - z_4)) - s(a_2c_4 - a_4c_2)]A_m^{-1} \\ [(c_4(x - x_4) - a_3(z - z_4)) + (a_2c_3 - a_3c_2)s]A_m^{-1} \\ [(c_4(x - x_4) - a_3(z - z_4)) + (a_2c_3 - a_3c_2)s]A_m^{-1} \end{bmatrix}$$

$$\begin{bmatrix} \frac{\delta s}{\delta z_1} \\ \frac{\delta s}{\delta z_2} \\ \frac{\delta s}{\delta z_3} \\ \frac{\delta s}{\delta z_3} \end{bmatrix} = \begin{bmatrix} -s(a_3b_4 - b_3a_4)A_m^{-1} \\ [(b_3(x - x_4) - a_4(y - y_4)) - s(a_4b_2 - a_2b_4)]A_m^{-1} \\ [(b_3(x - x_4) - a_3(y - y_4)) - (a_2b_3 - a_3b_2)s]A_m^{-1} \end{bmatrix}$$

$$= \begin{bmatrix} (b_3(x - x_4) - a_3(y - y_4)) - (a_2b_3 - a_3b_2)s]A_m^{-1} \\ [(b_3(x - x_4) - a_3(y - y_4)) - (a_2b_3 - a_3b_2)s]A_m^{-1} \end{bmatrix}$$

$$\begin{bmatrix} \frac{\delta i}{\delta x_1} \\ \frac{\delta i}{\delta x_2} \\ \frac{\delta i}{\delta x_2} \\ \frac{\delta i}{\delta x_3} \\ \frac{\delta i}{\delta x_4} \\ \frac{\delta i}{\delta x_2} \\ \frac{\delta i}{\delta x_3} \\ \frac{\delta i}{\delta x_4} \\ \frac{\delta i}{\delta x_3} \\ \frac{\delta i}{\delta x_4} \\ \frac{\delta i}{\delta x_3} \\ \frac{\delta i}{\delta x_4} \\ \frac{\delta i}{\delta x_2} \\ \frac{\delta i}{\delta x_3} \\ \frac{\delta i}{\delta y_1} \\ \frac{\delta i}{\delta y_2} \\ \frac{\delta i}{\delta y_2} \\ \frac{\delta i}{\delta y_2} \\ \frac{\delta i}{\delta y_2} \\ \frac{\delta i}{\delta y_3} \\ \frac{\delta i}{\delta y_4} \\ \frac{\delta i}{\delta y_2} \\ \frac{\delta i}{\delta y_2} \\ \frac{\delta i}{\delta y_3} \\ \frac{\delta i}{\delta y_4} \\ \frac{\delta i}{\delta y_2} \\ \frac{\delta i}{\delta y_3} \\ \frac{\delta i}{\delta y_4} \\ \frac{\delta i}{\delta y_2} \\ \frac{\delta i}{\delta y_3} \\ \frac{\delta i}{\delta y_2} \\ \frac{\delta i}{\delta y_3} \\ \frac{\delta i}{\delta z_2} \\ \frac{\delta i}{\delta z_2} \\ \frac{\delta i}{\delta z_3} \\ \frac{\delta i}{\delta z_3} \\ \frac{\delta i}{\delta z_3} \\ \frac{\delta i}{\delta z_3} \\ \frac{\delta i}{\delta z_4} \\ \frac{\delta i}{\delta x_2} \\ \frac{\delta i}{\delta x_3} \\ \frac{\delta i}{\delta x_4} \\ \frac{\delta i}{\delta x_2} \\ \frac{\delta i}{\delta x_3} \\ \frac{\delta i}{\delta x_2} \\ \frac{\delta i}{\delta x_3} \\ \frac{\delta i}{\delta x_4} \\ \frac{\delta i}{\delta x_2} \\ \frac{\delta i}{\delta x_3} \\ \frac{\delta i}{\delta x_4} \\ \frac{\delta i}{\delta x_2} \\ \frac{\delta i}{\delta x_3} \\ \frac{\delta i}{\delta x_4} \\ \frac{\delta i}{\delta x_2} \\ \frac{\delta i}{\delta x_3} \\ \frac{\delta i}{\delta x_4} \\ \frac{\delta i}{\delta x_2} \\ \frac{\delta i}{\delta x_3} \\ \frac{\delta i}{\delta x_4} \\ \frac{\delta i}{\delta x_2} \\ \frac{\delta i}{\delta x_3} \\ \frac{\delta i}{\delta x_4} \\ \frac{\delta i}{\delta x_2} \\ \frac{\delta i}{\delta x_3} \\ \frac{\delta i}{\delta x_4} \\ \frac{\delta i}{\delta x_2} \\ \frac{\delta i}{\delta x_3} \\ \frac{\delta i}{\delta x_4} \\ \frac{\delta i}{\delta x_2} \\ \frac{\delta i}{\delta x_3} \\ \frac{\delta i}{\delta x_4} \\ \frac{\delta i}{\delta x_2} \\ \frac{\delta i}{\delta x_3} \\ \frac{\delta i}{\delta x_4} \\ \frac{\delta i}{\delta x_2} \\ \frac{\delta i}{\delta x_3} \\ \frac{\delta i}{\delta x_4} \\ \frac{\delta i}{\delta x_2} \\ \frac{\delta i}{\delta x_3} \\ \frac{\delta i}{\delta x_4} \\ \frac{\delta i}{\delta x_2} \\ \frac{\delta i}{\delta x_3} \\ \frac{\delta i}{\delta x_4} \\ \frac{\delta i}{\delta x_2} \\ \frac{\delta i}{\delta x_3} \\ \frac{\delta i}{\delta x_4} \\ \frac{\delta i}{\delta x_2} \\ \frac{\delta i}{\delta x_3} \\ \frac{\delta i}{\delta x_4} \\ \frac{\delta i}{\delta x_2} \\ \frac{\delta i}{\delta x_3} \\ \frac{\delta i}{\delta x_4} \\ \frac{\delta i}{\delta x_4} \\ \frac{\delta i}{\delta x_3} \\ \frac{\delta i}{\delta x_4} \\ \frac{\delta i}{\delta$$

$$\frac{\delta w_m^t(u)}{\delta \psi_i} = \begin{bmatrix}
a_2 \frac{\delta s}{\delta \psi_i} + a_3 \frac{\delta t}{\delta \psi_i} + a_4 \frac{\delta u}{\delta \psi_i} \\
b_2 \frac{\delta s}{\delta \psi_i} + b_3 \frac{\delta t}{\delta \psi_i} + b_4 \frac{\delta u}{\delta \psi_i} \\
c_2 \frac{\delta s}{\delta \psi_i} + c_3 \frac{\delta t}{\delta \psi_i} + c_4 \frac{\delta u}{\delta \psi_i}
\end{bmatrix}$$
(5.32)

CHAPTER 6 Conclusions

6.1 Thesis Summary

The work presented in this thesis investigates the optimal usage of the Jensen Rényi divergence as applied to the tasks of segmentation and deformable registration, performed both independently and simultaneously. A custom biomechanical phantom capable of full reproduction of patient breathing traces was constructed for the purpose of evaluating joint segmentation/registration algorithms in a deformable manner with the possibility of scanning with PET/CT and MRI. The development of the algorithms outlined in this work is primarily motivated by the need to improve the practicality of adaptive radiotherapy planning. Our intention is the mitigation of possible errors introduced through the use of low quality images from CBCT [166] or PET [91].

This work began as the application of the Jensen Rényi divergence to the task of segmentation using a semi-automated level sets approach as detailed in Chapter 3. Previously this had only been applied as an edge detection filter [73]. Using an entropy based approach in this manner presented several attractive features such as the use of multiple modalities, lack of limits on the number of input images, robustness to noise and the ability to tailor the algorithm behaviour to the modality, or combination of modalities, in question. Our results were evaluated using 7 macroscopically derived contours from histological slides of resected pharyngolaryngeal squamous cell

carcinoma samples. Comparing to the results of 9 other algorithms evaluated using the same dataset the Jensen Rényi based segmentation technique had the second lowest mean classification error of 65% compared to 55% for the highest performing algorithm (FCM-SW). Additional evaluations were performed on thoracic PET/CT scans of non-small cell lung carcinoma patients where the maximal tumor diameter was the ground truth. Mean errors of 63%, 19.5% and 14.8% were found when using CT, PET and PET/CT for segmentation. Comparisons using a phantom scanned with varying parameters using CBCT showed a resilience to noise that was not seen when plotting the mutual information metric.

Following these promising results, we decided to investigate the utility of coupling our segmentation technique to a deformable registration algorithm, shown in Chapter 5. A non-rigid registration algorithm was designed using an adaptive meshing technique for control point selection. The two procedures were performed simultaneously. The coupling of the registration to the segmentation is dependent on the segmentation procedure using both the reference and target images as inputs. With improved registration accuracy, the segmentation also improves. The coupling in the other direction was achieved by introducing a coupling term into the registration gradient calculation. This term seeks to maximize the Jensen Rényi divergence as applied to the segmentation task, but by way of moving the control points. In order to properly evaluate this technique however, we first required the construction of a multi-modal deformable phantom with segmentation targets. This is covered in Chapter 4 with the utilization of preserved swine lungs, deformed using a computer controlled airflow system. Segmentation was evaluated through the use

of synthetic targets with multiples compartments and the use of modality specific contrast agents. Registration was evaluated using an in-house bifurcation tracking pipeline. With this dataset providing a reliable ground truth, the maximum overall registration accuracy was found to be 1.14 voxel widths or 2.01 mm with an α value of 0.7. An optimal coupling coefficient of 0.55 was found, improving the local registration accuracy surrounding the targets by 26% at the cost of overall registration accuracy.

6.2 Discussion and Future Work

The segmentation algorithm produced competitive results when applied to PET alone and with regard to PET and CT combined. As the algorithm has been observed to contain sensitivity to low contrast boundaries we envision that there are potential applications to the delineation of liver lesions, in particular when imaged with CT or CBCT[167]. MRI scans of the phantom described in Chapter 3 were also acquired using a T1-weighted fast field echo sequence on a Panorama 0.23 T (Phillips Medical Systems, Cleveland, OH, USA). By varying the TE time, SNRs of approximately 11.6-28.3 dB were acquired as shown in Figure 6–1.

Regarding the work presented in chapter 3, there was difficulty in acheiving consistent segmentations of the inner jar when using MRI due to field heterogeneities leading to gradients in the image intensity. This led to incomplete segmentation of the inner jar which is the reason these results were not included in the publication of Chapter 3. This is a possible artifact for many MRI scanning protocols which may lead to sub-par results when using the JR based level-set algorithm. A correction similar to the steps outlined in Figure 3–4, Chapter 3 could be applied but they are not

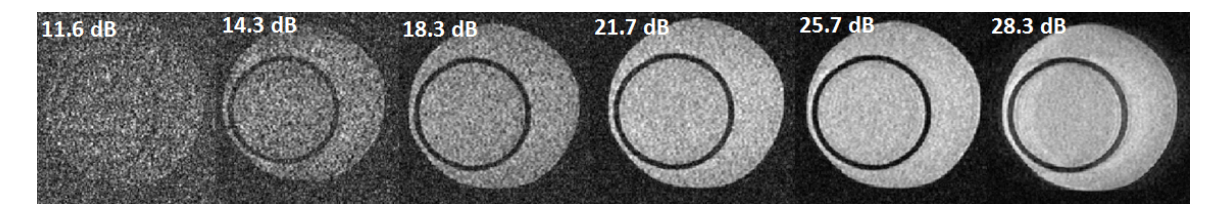


Figure 6–1: T1-weighted 3D FFE scans of the jar phantom with SNR values of 11.6,14.3,18.,21.7,25.7 and 28.3 dB.

practical for application in a clinical case. There are already established methods for inhomogeneity corrections of MRI images which would likely be better suited [168]. Alternatively, a piecewise formulation of the level sets method [169] using the Jensen Rényi divergence may be able to segment MRI volumes in cases where these artifacts exist without the need for inhomogeneity corrections. Segmentation accuracy with regard to macroscopically heterogenous tumor appearances in MRI may also benefit from this tactic. Similar difficulties with MRI images were experienced when using the simultaneous registration/segmentation algorithm presented in Chapter 5. This was primarily due to the loss of contrast between the lung and the background air in MRI compared to CT. This is caused by microscopic tissue inhomogeneity in the lung leading to a loss of signal. For this reason the modalities presented were somewhat limited. A larger study to investigate the relationship of α to the imaging modality would allow further adoption of this technique for other purposes whether they are research or clinically oriented. More complex interpolation and regularization methods would allow smoother deformations which were observed to compromise image quality during our experiments. An interesting observation made during the experiments was the fact that overall registration error increases as local registration error is reduced in the vicinity of the segmentation targets. This is understandable when one considers the regularization as a smoothing filter and that influences from the coupling term on regions outside the targets from smoothing may account for this. This could be remedied by implimenting an anisotropic filter that differentially smooths the local regions occupied by the segments similar to that proposed by Pace et al.[170].

A necessity of the biomechanical phantom to be considered for QA use in the clinic is longevity and reproducibility. While the manufacturers (Nasco, Fort Atkinson, WI) have suggested that the preserved swine lungs will last 6 months, the author would like to note that the samples used in this work have thus far remained functional following 2 years of proper storage. An additional procedure was conducted when dealing with 3D scans in order to ensure that the lungs were static throughout the acquisition. A ruler clamped to a tort stand was used to provide simple visual comparison of the inflation level in order to adjust the pump such that internal pressure of the lungs remained constant. This procedure was repeated 3 times for the same inflation level beginning from a deflated state. Volume measurements of the lungs from the acquired CT scans revealed a standard deviation of 3.75% of the mean volume. While this level of uncertainty is fairly low, it stresses the importance of further work to account for compromised tissue samples from the supplier.

As mentioned briefly in the final remarks of chapter 4, the addition of an outer shell in order to complete the appearance of a human torso is an obvious next step for the lung phantom. This is required not only for added realism and completeness but because intensity based registration accuracy is heavily influenced by high-contrast regions such as between the lung and chest wall. Currently the dataset presented

in this thesis can be considered challenging as the boundaries between lung and air are not as pronounced. Such an addition would not be challenging considering the availability of high quality plastinated specimens [171].

Further use of the lung phantom could be made by evaluating the accuracy of target tracking algorithms used to account for intra-fractional motion. This could be performed by accommodating the inclusion of a MOSFET, TLD or film measurement into the phantom in order to perform dosimetric comparisons with values predicted by the treatment planning system.

References

- [1] E. B. Podgorsak. Radiaton Oncology Physics: A Handbook for Teachers and Students. International Atomic Energy Agency, 2005.
- [2] L. Vaalavirta, N. Rasulova, K. Partanen, T. Joensuu, and K. Kairemo. [18f]-estradiol pet/ct imaging in breast cancer patients. *Journal of Diagnostic Imaging in Therapy*, 1(1):59–72, 2014.
- [3] H. Zaidi, M. Abdoli, C. L. Fuentes, and I. M. El Naqa. Comparative methods for PET image segmentation in pharyngolaryngeal squamous cell carcinoma. *Eur J Nucl Med*, 39:881–891, 2012.
- [4] American Cancer Society. Cancer facts and figures 2015. Technical report, American Cancer Society, 2015.
- [5] American Cancer Society. Cancer treatment and survivorship: Facts and figures 2014-2015. Technical report, American Cancer Society, 2014.
- [6] M. Oliver, W. Ansbacher, and W. A. Beckham. Comparing planning time, delivery time and plan quality for imrt, rapidarc and tomotherapy. J. App. Clin. Med. Phys., 10(4), 2009.
- [7] N. Ploquin and P. Dunscombe. A cost-outcome analysis of image-guided patient repositioning in the radiation treatment of cancer of the prostate. *Radio. and Oncol.*, 93:25.
- [8] E. Weiss and C. F. Hess. The impact of gross tumor volume (gtv) and clinical target volume (ctv) definition on the total accuracy in radiotherapy theoretical aspects and practical experiences. *Strahlentherapie und Onkologie*, 179:21.
- [9] K. Mah, C. B. Caldwell, Y. C. Ung, C. E. Danjoux, J. M. Balogh, S. N. Ganguli, L. E. Ehrlich, and R. Tirona. The impact of (18)FDG-PET on target and critical organs in CT-based treatment planning of patients with poorly defined non-small-cell lung carcinoma: a prospective study. *Int J Radiat Oncol Biol Phys*, 52(2):339–350, 2002.

- [10] J. Bussink, A. J. van der Kogel, and J. H. Kaanders. Activation of the pi3-k/akt pathway and implication for radioresistance mechanisms in head and neck cancer. *Lancet Oncol*, 9:288–296, 2008.
- [11] H. D. Skinner, V. C. Sandulache, T. J. Ow, R. E. Meyn, J. S. Yordy, B. M. Beadle, A. L. Fitzgerald, U. Giri, K.K. Ang, and J.N. Myers. Tp53 disruptive mutations lead to head and neck cancer treatment failure through inhibition of radiation-induced senescence. *Clinical Cancer Research*, 18:290–300, 2012.
- [12] K. K. Ang, J. Harris, R. Wheeler, R. Weber, D. I. Rosenthal, P. F. Nguyen-Tan, W. H. Westra, C. H. Chung, R. C. Jordan, C. Lu, H. Kim, R. Axelrod, C. C. Silverman, K. P. Redmond, and M. L. Gillison. Human papillomavirus and survival of patients with oropharyngeal cancer. New England Journal of Medicine, 63:24–35, 2010.
- [13] P. Sridhar, G. Mercier, J. Tan, M. T. Truong, B. Daly, and Subramaniam R. M. Fdg pet metabolic tumor volume segmentation and pathologic volume of primary human solid tumors. *American Journal of Roentgenology*, 202(5):1114–1119, 2014.
- [14] E Colvill, J Booth, S Nill, M Fast, J Bedford, U Oelfke, M Nakamura, P Poulsen, R Hansen, E Worm, T Ravkilde, J Scherman Rydhoeg, T Pommer, P Munck Af Rosenschoeld, S Lang, M Guckenberger, C Groh, C Herrmann, D Verellen, K Poels, L Wang, M Hadsell, O Blanck, T Sothmann, and P Keall. Th-ab-303-01: Benchmarking real-time adaptive radiotherapy systems: A multi- platform multi-institutional study. Medical Physics, 42(6):3710–3711, 2015.
- [15] C. Richmond. Sir godfrey hounsfield. British Medical Journal, 329(7467):687, 2004.
- [16] Mohamed Ahmed Youssef, Mahmoud Abdelaziz Dawoud, Aly Aly Elbarbary, Mohamed Mohamed Elbedewy, and Hasan Mohamed Elkhateeb. Role of 320slice multislice computed tomography coronary angiography in the assessment of coronary artery stenosis. The Egyptian Journal of Radiology and Nuclear Medicine, 45(2):317 – 324, 2014.
- [17] M. A. Blake and K. K. Mannudeep. Imaging in oncology. Cancer Treatment and Research, 143, 2008.

- [18] M. Sattarivand, C. Caldwell, I. Poon, H. Soliman, and K. Mah. Effects of roi placement on pet-based assessment of tumor response to therapy. *International Journal of Molecular Imaging*, (2013), 2013.
- [19] A. Ardeshir Goshtasby. *Principles of Magnetic Resonance Imaging*. Wiley-Interscience, 1996.
- [20] H. Huang, H. Lu, G. Feng, and H. Jiand et. al. Determining appropriate timing of adaptive radiation therapy for nasopharyngeal carcinoma during intensity-modulated radiation therapy. *Radiation Oncology*, 10:92, 2015.
- [21] Charlotte L. Brouwer, Roel J.H.M. Steenbakkers, Johannes A. Langendijk, and Nanna M. Sijtsema. Identifying patients who may benefit from adaptive radiotherapy: Does the literature on anatomic and dosimetric changes in head and neck organs at risk during radiotherapy provide information to help? *Radiotherapy and Oncology*, 115(3):285 294, 2015.
- [22] Robert M. Haralick and Linda G. Shapiro. Computer and Robot Vision. Addison-Wesley Longman Publishing Co., Inc., Boston, MA, USA, 1st edition, 1992.
- [23] Michael Kass, Andrew Witkin, and Demetri Terzopoulos. Snakes: Active contour models. *International Journal of Computer Vision*, 1(4):321–331, 1988.
- [24] S. Osher and J. Sethian. Comput. phys. Fronts propagating with curvature dependent speed: algorithms based on Hamilton-Jacobi formulations, 79(1):12–49, 1988.
- [25] D. Mumord and J. Shah. Comm. pure appl. math. Optimal approximations by piece-wise smooth functions and associated variational problems, 42:577–685, 1989.
- [26] T. F. Chan and L. A. Vese. Active contours without edges. *IEEE Transactions on Image Processing*, 10(2):266–277, 2001.
- [27] H. K. Zhao, T. Chan, B. Merriman, and S. Osher. A variational level set approach to multiphase motion. ournal of Computational Physics, 127:179– 195, 1996.
- [28] E. Schreibmann, D. M. Marcus, and T. Fox. Multiatlas segmentation of thoracic and abdominal anatomy with level set-based local search. *Journal of Applied Clinical Medical Physics*, 15(4):22–38, 2014.

- [29] Yongxin Zhou and Jing Bai. Organ segmentation using atlas registration and fuzzy connectedness. In 2005 IEEE Engineering in Medicine and Biology 27th Annual Conference, pages 3241–3244, 2005.
- [30] N. Kovačević, J. T. Henderson, E. Chan, N. Lifshitz, J. Bishop ad A.C. Evans, R.M. Henkelman, and X.J. Chen. A three-dimensional mri atlas of the mouse brain with estimates of the average and variability. *Cerebral Cortex*, 15:639–645, 2005.
- [31] Mikael Agn, Ian Law, Per Munck af Rosenschld, and Koen Van Leemput. A generative model for segmentation of tumor and organs-at-risk for radiation therapy planning of glioblastoma patients, 2016.
- [32] Jeongtae Kim and J. A. Fessler. Intensity-based image registration using robust correlation coefficients. *IEEE Transactions on Medical Imaging*, 23(11):1430–1444, 2004.
- [33] F. Maes, Andre Collignon, D. Vandermeulen, G. Marchal, and P. Suetens. Multimodality image registration by maximization of mutual information. *IEEE Transactions on Medical Imaging*, 16(2):187–198, 1997.
- [34] A. C. S. Chung, W. M. Wells III, A. Norbash, and W. E. L. Grimson. Multi-modal image registration by minimising kullback-leibler distance. MICCAI 2002 LNCS, 2489:525–532, 2002.
- [35] C. Chefd'Hotel, G. Hermosillo, and O. Faugeras. Multi-modal image registration by minimising kullback-leibler distance. MICCAI 2002 LNCS, 2489:525–532, 2002.
- [36] Floris F. Berendsen, Uulke A. van der Heide, Thomas R. Langerak, Alexis N.T.J. Kotte, and Josien P.W. Pluim. Free-form image registration regularized by a statistical shape model: application to organ segmentation in cervical {MR}. Computer Vision and Image Understanding, 117(9):1119 1127, 2013.
- [37] Jinzhong Yang, Beth M. Beadle, Adam S. Garden, David L. Schwartz, and Michalis Aristophanous. A multimodality segmentation framework for automatic target delineation in head and neck radiotherapy a). *Medical Physics*, 42(9):5310–5320, 2015.

- [38] Issam El Naqa, Deshan Yang, Aditya Apte, Divya Khullar, Sasa Mutic, Jie Zheng, Jeffrey D. Bradley, Perry Grigsby, and Joseph O. Deasy. Concurrent multimodality image segmentation by active contours for radiotherapy treatment planninga). *Medical Physics*, 34(12), 2007.
- [39] A. Gholipour, N. D. Kehtarnavaz, R.W. Briggs, M. Devous, and K.S. Gopinath. Brain functional localization: A survery of image registration techniques. *IEEE Transactional Medical Imaging*, 26(4):427 – 451, 2007.
- [40] P. Slomka and R. Baum. Multimodality image registration with software: state-of-the-art. European Journal of Nuclear Medicine and Molecular Imaging, 36:44 55, 2009.
- [41] J. Yang. The thin plate spline robust point matching (tps-rpm) algorithm: a revisit. Patt Recog Let, 32(7):910–18, 2011.
- [42] C. L. Guyader and L. A. Vese. A combined segmentation and registration framework with a nonlinear elasticity smoother. In *SSVM 2009*, *LNCS*, volume 5567, 2009.
- [43] J. M. Balter and C. A. Pelizzari et al. Correlation of projection radiographs in radiation therapy using open curve segments and points. *Med. Phys.*, 19(2):329 334, 1992.
- [44] J. Cai and C. H. J. Chu et al. A simple algorithm for planar image registration in radiation therapy. *Med. Phys.*, 25(6):824 829, 1998.
- [45] P. A. Viola. Alignment by maximization of mutual information. PhD thesis, Massachusetts Institute of Technology, 1995.
- [46] P. Viola and W. M. Wells. Alignment by maximization of mutual information. In Computer Vision, 1995. Proceedings., Fifth International Conference on, pages 16–23, Jun 1995.
- [47] G. K. Rohde, A. Aldroubi, and B. M. Dawant. The adaptive bases algorithm for intensity-based nonrigid image registration. *IEEE Transactions on Medical Imaging*, 22(11):1470–1479, 2003.
- [48] W. Sun, W. Zhou, and M. Yang. Medical image registration using thin-plate spline for automatically detecting and matching of point sets. In *Bioinformatics and Biomedical Engineering*, (iCBBE) 2011 5th International Conference on, pages 1–4, 2011.

- [49] B. Ahn, H. Il Koo, and N. Ik Cho. Image registration algorithm based on regular sparse correspondences and sift. In *APSIPA 2014*, 2014.
- [50] Z. Xie and G. E. Farin. Image registration using hierarchical b-splines. *IEEE Transactions on Visualization and Computer Graphics*, 10(1):1–10, 2004.
- [51] Tom Vercauteren, Xavier Pennec, Aymeric Perchant, and Nicholas Ayache. Diffeomorphic demons: Efficient non-parametric image registration. *NeuroImage*, 45(1, Supplement 1):S61 S72, 2009. Mathematics in Brain Imaging.
- [52] J.-P. Thirion. Image matching as a diffusion process: An analogy with maxwell's demons. *Medical Image Analysis*, 7(4):565-575, 1998.
- [53] K. K. Brock and The Deformable Registration Accuracy Consortium. Results of a multi-institution registration accuracy study (midras). *Int. J. Radiation Oncology Biol. Phys.*, 76(2):583–596, 2010.
- [54] B.B. Avants, C.L. Epstein, M. Grossman, and J.C. Gee. Symmetric diffeomorphic image registration with cross-correlation: Evaluating automated labeling of elderly and neurodegenerative brain. *Medical Image Analysis*, 12(1):26 41, 2008. Special Issue on The Third International Workshop on Biomedical Image Registration {WBIR} 2006.
- [55] Bjoern Menze, Andras Jakab, Mauricio Reyes, Stefan Bauer, Marcel Prastawa, and Koen Van Leemput, editors. *Proceedings of the MICCAI Challenge on Multimodal Brain Tumor Image Segmentation (BRATS) 2012*, Nice, France, October 2012. MICCAI.
- [56] K. Murphy, B. van Ginneken, J. M. Reinhardt, S. Kabus, K. Ding, X. Deng, K. Cao, K. Du, G. E. Christensen, V. Garcia, T. Vercauteren, N. Ayache, O. Commowick, G. Malandain, B. Glocker, N. Paragios, N. Navab, V. Gorbunova, J. Sporring, M. de Bruijne, X. Han, M. P. Heinrich, J. A. Schnabel, M. Jenkinson, C. Lorenz, M. Modat, J. R. McClelland, S. Ourselin, S. E. A. Muenzing, M. A. Viergever, D. De Nigris, D. L. Collins, T. Arbel, M. Peroni, R. Li, G. C. Sharp, A. Schmidt-Richberg, J. Ehrhardt, R. Werner, D. Smeets, D. Loeckx, G. Song, N. Tustison, B. Avants, J. C. Gee, M. Staring, S. Klein, B. C. Stoel, M. Urschler, M. Werlberger, J. Vandemeulebroucke, S. Rit, D. Sarrut, and J. P. W. Pluim. Evaluation of registration methods on thoracic ct: The empire10 challenge. IEEE Transactions on Medical Imaging, 30(11):1901–1920, Nov 2011.

- [57] R. P. Woods, S. T. Grafton, C. J. Holmes, S. R. Cherry, and J. C. Mazziotta. Automated image registration: I. general methods and intrasubject, intramodality validation. J. Comput. Assist. Tomogr., 22:139 – 52, 1998.
- [58] K. J. Friston, J. Ashburner, C. D. Frith, J.-B. Poline, J. D. Heather, and R. S. J. Frackowiak. A review of geometric transformations for nonrigid body registration. *Human Brain Mapping*, 2:165–189, 1995.
- [59] D. Rueckert, L. I. Sonoda, C. Hayes, D. L. G. Hill, M. O. Leach, and D. J. Hawkes. Nonrigid registration using free-form deformations: Application to breast mr images. *IEEE Transactions on Medical Imaging*, 18(8):712–721, 199.
- [60] A. Ardeshir Goshtasby. 2D and 3-D Image Registration: For Medical, Remote Sensing, and Industrial Applications. Wiley-Interscience, 2005.
- [61] M. Holden. A review of geometric transformations for nonrigid body registration. *IEEE Transactions on Medical Imaging*, 27(1):111–128, 2008.
- [62] M. Styner, C. Brechbühler, G. Szekély, and G. Gerig. Parametric estimate of intensity inhomogeneities applied to mri. *Med. Imaging*, 19:153–165, 2000.
- [63] J. C. Spall. An overview of the simultaneous perturbation method for efficient optimization. *John Hopkins APL Technical Digest*, 19:482–492, 1998.
- [64] S. Kirkpatrick, C. D. Gelatt, and M. P. Vecchi. Optimization by simulated annealing. *Science*, 220(4598):671–680, 1983.
- [65] Pascal Cachier, Xavier Pennec, and Nicholas Ayache. Fast Non Rigid Matching by Gradient Descent: Study and Improvements of the "Demons" Algorithm. Technical Report RR-3706, INRIA, June 1999.
- [66] Radu Stefanescu, Xavier Pennec, and Nicholas Ayache. Grid powered nonlinear image registration with locally adaptive regularization. *Medical Image Analy*sis, 8(3):325 – 342, 2004. Medical Image Computing and Computer-Assisted Intervention - {MICCAI} 2003.
- [67] Morten Bro-Nielsen and Claus Gramkow. Fast Fluid Registration of medical images, pages 265–276. Springer Berlin Heidelberg, Berlin, Heidelberg, 1996.

- [68] M. Staring, S. Klein, and J. P. W. Pluim. Nonrigid registration with tissue-dependent filtering of the deformation field. *Physics in Medicine and Biology*, 52:6879 6892, 2007. Phys. Med. Biol.
- [69] A. Trouve. Diffeomorphism groups and pattern matching in mage analysis. *Int. J. Comput. Vision*, 28:213 221, 1998.
- [70] C. Chefd'hotel, G. Hermosillo, and O. Faugeras. Flows of diffeomorphisms for multimodal image registration. In *Biomedical Imaging*, 2002. Proceedings. 2002 IEEE International Symposium on, pages 753–756, 2002.
- [71] E. Hader and J. Modersitzki. Numerical methods for volume preserving image registration. *Inverse Problems*, 20(5):1621, 2004.
- [72] R. Duda and P. Hart. Pattern classification and scene analysis. *Int. J. Comp. Vis.*, 24(2):137–154, 1973.
- [73] A. B. Hamza and H. Krim. Image registration and segmentation by maximizing the Jensen-Renyi Divergence. *Lect Notes Comput Sci*, 2683:147–163, 2003.
- [74] E. C. Halperin, C. A. Perez, and L. W. Brady. Perez and Bradys Principles and Practice of Radiation Oncology. Kluwer/Lippincott Williams & Wilkins, Philidelphia, PA, 2008.
- [75] J. V. D. Steene, N. Linthout, J. D. Mey, V. Vinh-Hung, C. Claassens, M. Noppen, A. Bel, and G. Storme. Definition of gross tumor volume in lung cancer: interobserver variability. *Radiother Oncol*, 62:37–49, 2002.
- [76] S. Senan, J. van Sornsen de Koste, M. Samson, H. Tankink, P. Jansen, P. J. Nowak, A. D. Krol, P. Schmitz, and F. J. Lagerwaard. Evaluation of a target contouring protocol for 3D conformal radiotherapy in non-small cell lung cancer. *Radiother Oncol*, 53:247–255, 1999.
- [77] J. J. Erasmus, G. W. Gladish, L. Broemeling, B. S. Sabloff, M. T. Truong, R. S. Herbst, and R. F. Munden. Interobserver and intraobserver variability in measurement of nonsmall-cell carcinoma lung lesions: Implications for assessment of tumor response. *J Clin Oncol*, 21(13):2574–2582, 2003.
- [78] P. A. Kupelian, C. Ramsey, S. L. Meeks, T. R. Willoughby, A. Forbes, T. H. Wagner, and K. M. Langen. Serial megavoltage {CT} imaging during external beam radiotherapy for non-small-cell lung cancer: Observations on tumor

- regression during treatment. Int J Radiat Oncol Biol Phys, 63(4):1024 1028, 2005.
- [79] J. L. Barker Jr, A. S. Garden, K. K. Ang, J. C. O'Daniel, H. Wang, L. E. Court, W. H. Morrison, D. I. Rosenthal, K. S. C. Chao, S. L. Tucker, R. Mohan, and L. Dong. Quantification of volumetric and geometric changes occurring during fractionated radiotherapy for head-and-neck cancer using an integrated ct/linear accelerator system. Int J Radiat Oncol Biol Phys, 59(4):960 970, 2004.
- [80] L. Xing, J. Seibers, and P. Keall. Computational challenges for image-guided radiation therapy: Framework and current research. *Semin Radiat Oncol*, 17:245–57, 2007.
- [81] J. Bradley, W. L. Thorstad, S. Mutic, T. R. Miller, F. Dehdashti, B. A. Siegel, W. Bosch, and R. J. Bertrand. Impact of FDG-PET on radiation therapy volume delineation in non-small-cell lung cancer. *Int J Radiat Oncol Biol Phys*, 59:78–86, 2004.
- [82] A. C. Paulino, M. Koshy, R. Howell, D. Schuster, and L. W. Davis. Comparison of CT- and FDG-PET-defined gross tumor volume in intensity-modulated radiotherapy for head-and-neck cancer. *Int J Radiat Oncol Biol Phys*, 61:1385–1392, 2005.
- [83] U. Nestle, K. Walter, S. Schmidt, N. Licht, C. Neider, B. Motaref, D. Hellwig, M. Niewald, D. Ukena, C. M. Kirsch, G. W. Sybrecht, and K. Schnabel. ¹⁸F-Deoxyglucose positron emission tomography (FDG-PET) for the planning of radiotherapy in lung cancer: high impact in patients with atelectasis. *Int J Radiat Oncol Biol Phys*, 44:593–597, 1999.
- [84] P. Giraud, D. Grahek, F. Montravers, M. F. Carette, E. Deniaud-Alexandre, F. Julia ad J. C. Rosenwald, J. M. Cosset, J. N. Talbot, M. Housset, and E. Touboul. CT and ¹⁸F-deoxyglucose (FDG) image fusion for optimization of conformal radiotherapy of lung cancers. *Int J Radiat Oncol Biol Phys*, 49:1249–1257, 2001.
- [85] U. Nestle, S. Kremp, A. Schaefer-Schuler, C. Sebastian-Welsch, D. Hellwig, C. Rube, and C. M. Kirsch. Comparison of different methods for delineation of ¹⁸F-FDG PET-positive tissue for target volume deinition in radiotherapy of patients with non-small cell lung cancer. *J Nucl Med*, 46:1342–1348, 2005.

- [86] A. C. Paulino and P. A. Johnstone. FDG-PET in radiotherapy treatment planning: pandoras box? *Int J Radiat Oncol Biol Phys*, 59:4–5, 2004.
- [87] Q. C. Black, I. S. Grills, L. L. Kestin, C. Y. Wong, J. W. Wong, A. A. Martinez, and D. Yan. Defining a radiotherapy target with positron emission tomography. Int J Radiat Oncol Biol Phys, 60(4):1272–1282, 2003.
- [88] K. J. Biehl, F. M. Kong, F. Dehdashti, J. Y. Jin, S. Mutic, I. El Naqa, B. A. Siegel, and J. D. Bradley. 18F-FDG PET definition of gross tumor volume for radiotherapy of non-small cell lung cancer: is a single standardized uptake value threshold approach appropriate? J Nucl Med, 47(11):1808–1812, 2006.
- [89] A. V. Baardwijk, G. Bosmans, L. Boersma, J. Buijsen, S. Wanders, M. Hochstenbag, R. J. Van Suylen, A. Dekker, C. Dehing-Oberije, R. Houben, S. M. Bentzen, M. Van Kroonenburgh, P. Lambin, and D. de Ruysscher. PET-CT-based auto-contouring in non-small-cell lung cancer correlates with pathology and reduces interobserver variability in the delineation of the primary tumor and involved nodal volumes. Int J Radiat Oncol Biol Phys, 68:771–778, 2007.
- [90] D. A. Schinagl, W. V. Vogel, A. L. Hoffmann, J. A. V. Dalen, W. J. Oyen, and J. H. Kaanders. Comparison of five segmentation tools for 18F-fluoro-deoxyglucose-positron emission tomography-based target volume definition in head and neck cancer. Int J Radiat Oncol Biol Phys, 69:1282–1289, 2007.
- [91] M. Hatt, F. Lamare, N. Boussion, A. Turzo, C. Collet, F. Salzenstein, C. Roux, P. Jarritt, K. Carson, C. C.-L. Rest, and D. Visvikis. Fuzzy hidden markov chains segmentation for volume determination and quantitation in pet. *Physics* in Medicine and Biology, 52(12):3467 –3491, 2007.
- [92] D. W. G. Montgomery, A. Amira, and H. Zaidi. Fully automated segmentation of oncological PET volumes using a combined multiscale and statistical model. *Med Phys*, 34(2):722–724, 2007.
- [93] D. L. Pham and J. L. Prince. An adaptive fuzzy c-means algorithm for image segmentation in the presence of intensity inhomogeneities. *Pattern Recognit* Lett, 20:57–68, 1999.
- [94] J. C. Bezdek, L. O. Hall, M. C. Clark, D. B. Goldgof, and L. P. Clarke. Medical image analysis with fuzzy models. *Statist Methods Med Res*, 6:191–214, 1997.

- [95] S. Belhassen and H. Zaidi. A novel fuzzy C-means algorithm for unsupervised heterogeneous tumor quantification in PET. *Med Phys*, 37(3):1309–1324, 2010.
- [96] Varian Medical Systems. Eclipse: Treatment Planning System. Promotional brochure, 2013. downloaded on May 2nd, 2013 from http://www.varian.com/media/oncology/products/eclipse/pdf/EclipseBrochure.pdf.
- [97] A. Lin, G. Kubicek, J. W. Piper, A. S. Nelson, A. P. Dicker, and R. K. Valicenti. Atlas-based segmentation in prostate IMRT: timesavings in the clinical workflow. *Int J Radiat Oncol Biol Phys*, 72(1):S328–S329, 2008.
- [98] H. Zaidi and I. El Naqa. PET-guided delineation of radiation therapy treatment volumes: a survey of image segmentation techniques. Eur J Nucl Med, 37:2165– 2187, 2010.
- [99] T. Sheperd, M. Teras, R. R. Beichel, R. Boellard, M. Bruynooghe, V. Dicken, M. J. Gooding, P. J. Julyan, J. A. Lee, S. Lefevre, M. Mix, V. Naranjo, X. Wu, H. Zaidi, Z. Zeng, and H. Minn. Comparative study with new accuracy metrics or target volume contouring in PET image guided radiation therapy. *IEEE Trans Med Im*, 31(11):2006–2024, 2012.
- [100] C. Xu and J.L. Prince. Snakes, shapes, and gradient vector flow. *IEEE Trans Image Process*, 7:359–369, 1998.
- [101] I. El Naqa, D. Yang, A. Apte, D. Khullar, S. Mutic, J. Zheng, J. D. Bradley, P. Grigsby, and J. O. Deasy. Concurrent multimodality image segmentation by active contours for radiotherapy treatment planning. *Med Phys*, 34(12):4738– 4749, 2007.
- [102] S. Milker-Zabel, A. Zabel du Bois, M. Henze, P. Huber, D. Schulz-Ertner, A. Hoess, U. Haberkorn, and J. Debus. Improved target volume definition for fractionated stereotactic radiotherapy in patients with intracranial meningiomas by correlation of CT, MRI and [68Ga]-DOTATOC-PET. Int J Radiat Oncol Biol Phys, 65(1):222–227, 2006.
- [103] C. C. Caldwell, K. Mah, Y. C. Ung, C. E. Danjoux, J. M. Balogh, S.N. Ganguli, and L. E. Ehrlich. Observer variation in contouring gross tumor volume in patients with poorly defined non-small-cell lung tumors on CT: the impact of ¹⁸FDG-hybrid PET fusion. *Int J Radiat Oncol Biol Phys*, 51(4):923–931, 2001.

- [104] C. Greco, K. Rosenzweig, G. L. Cascini, and O. Tamburrini. Current status of PET/CT for tumour volume definition in radiotherapy treatment planning for non-small cell lung cancer (NSCLC). *Lung Cancer*, 57(2):125–134, 2007.
- [105] I. Avazpour, R. E. Roslan, P. Bayat, M. I. Saripan, A. J. Nordin, and R. S. A. R. Abdullah. Segmenting CT images of Bronchogenic carcinoma with bone metastases using PET intensity markers approach. *Rad Oncol*, 43(3):180–186, 2009.
- [106] H. Yu, C. B. Caldwell, K. Mah, and D. Mozeg. Coregistered FDG PET/CT-Based Textural Characterization of Head and Neck Cancer for Radiation Treatment Planning. *IEEE Trans Med Im*, 28(3):374–383, 2009.
- [107] D. Han, J. Bayouth, Q. Song, A. Taurani, M. Sonka, J. Buatti, and X. Wu. Globally optimal tumor segmentation in PET-CT images: a graph-based co-segmentation method. *Inf Process Med Imaging*, 22:245–256, 2011.
- [108] Q. Song, J. Bai, D. Han, S. Bhatia, W. Sun, J. Bayouth, J. Buatti, and X. Wu. Optimal co-segmentation of tumor in PET-CT images with context information. *IEEE Trans Med Imaging*, 32(9):1685–1697, 2013.
- [109] F. Wang, T Syeda-Mahmood, B.C. Vemuri ad D. Beymer, and A. Rangarajan. Closed-form Jensen Renyi divergence for mixture of Gaussians and applications to group-wise shape registration. *MICCAI*, 12:648–655, 2009.
- [110] J. N. Kapur, P. K. Shaoo, and A. K. C. Wong. A new method or gray level picture thresholding using the entropy of histogram. *Comput Vision Graph Image Process*, 29:273 285, 1985.
- [111] T. Pun. A new method for gray-level picture thresholding using the entropy of the histogram. Signal Processing, 2(3):223 237, 1980.
- [112] T. Pun. Entropic thresholding, a new method for image segmentation. *Comput Graph Image Process*, 81, 1981.
- [113] J. Kim, J. W. Fisher, A. Yezzi, M. Çetin, and A. S. Willsky. A nonparametric statistical method or image segmentation using information theory and curve evolution. *IEEE Trans Image Process*, 14(10), 2005.
- [114] W. M. Wells III, P. Viola, H. Atsumi, S. Nakajima, and R. Kikinis. Multi-modal volume registration by maximization of mutual information. *Med Image Anal*, 1(1):35–51, 1996.

- [115] J. F. Daisne, T. Duprez, B. Weynand, M. Lonneux, M. Hamoir, H. Reychler, and V. Grégoire. Tumor volume in pharyngolaryngeal squamous cell carcinoma: comparison at CT, MR imaging, and FDG PET and validation with surgical specimen. *Radiology*, 233:93–100, 2004.
- [116] J. F. Daisne, M. Sibomana, A. Bol, G. Cosnard, M. Lonneux, and V. Grégoire. Evaluation of a multimodality image (CT, MRI and PET) coregistration procedure on phantom and head and neck cancer patients: accuracy reproducibility and consistency. *Radiother Oncol*, 69:237–245, 2003.
- [117] M. C. Chiang, R. A. Dutton, K. M. Hayashi, A. W. Toga, O. L. Lopez, H. J. Aizenstein, J. T. Becker, and P. M. Thompson. Fluid registration of medical images using Jense-Renyi divergence receals 3D profile of brain atrophy in HIV/AIDS. *IEEE Int. Symp. Biomed. Imag. (ISBI2006)*, pages 193–196, 2006.
- [118] A. Boss, S. Bisdas, A. Kolb, M. Hosmann, U. Ernemann, C. D. Claussen, C. Pfannenber, B. J. Pichler, M. Reimold, and L. Stegger. Hybrid pet/mri of intracranial masses: initial experiences and comparison to pet/ct. *J Nucl Med*, 51(8):1198–1205, 2010.
- [119] H. Aerts, E. Velazquez, R. Leijenaar, C. Parmar, P. Grossmann, S. Cavalho, and J. Bussink. Decoding tumour phenotype by noninvasive imaging using a quantitative radiomics approach. *Nature*, 5(1):4006, 2014.
- [120] A Carass, M.B. Wheeler, J. Cuzzocreo, P. L Bazin, S.S. Bassett, and J.L. Prince. A joint registration and segmentation approach to skull stripping. In *Biomedical Imaging: From Nano to Macro*, 2007. ISBI 2007. 4th IEEE International Symposium on, pages 656–659, April 2007.
- [121] Fei Wang, Baba C. Vemuri, and Stephan J. Eisenschenk. Joint registration and segmentation of neuroanatomic structures from brain {MRI}. Academic Radiology, 13(9):1104 1111, 2006.
- [122] A. Gooya, K. M. Pohl, M. Bilello, G. Biros, and C. Davatzikos. Joint segmentation and deformable registration of brain scans guided by a tumor growth model. *Med. Image Comput. Comput. Assist. Interv.*, 14(pt 2):532–540, 2011.

- [123] Ravi Bansal, Lawrence H. Staib, Zhe Chen, Ravinder Nath, and James S. Duncan. Entropy-based, multiple-portal-to-3dct registration for prostate radiotherapy using iteratively estimated segmentation. In *Medical Image Computing and Computer-Assisted Intervention MICCAI '99*, year = 1999, pages = 567–578, publisher = Springer Verlag.
- [124] A Yezzi, L. Zollei, and T. Kapur. A variational framework for joint segmentation and registration. In *Mathematical Methods in Biomedical Image Analysis*, 2001. MMBIA 2001. IEEE Workshop on, pages 44–51, 2001.
- [125] Zhong Xue, Kelvin Wong, and Stephen T.C. Wong. Joint registration and segmentation of serial lung {CT} images for image-guided lung cancer diagnosis and therapy. *Computerized Medical Imaging and Graphics*, 34(1):55 60, 2010. Image-Guided Surgical Planning and Therapy.
- [126] A Ayvaci and D. Freedman. Joint segmentation-registration of organs using geometric models. In *Engineering in Medicine and Biology Society*, 2007. EMBS 2007. 29th Annual International Conference of the IEEE, pages 5251–5254, Aug 2007.
- [127] A. Kerdok, S. Cotin, M. Ottensmeyer, A. Galea, R. Howe, and S. Dawson. Truth cube: establishing physical standards for soft tissue simulation. *Med Image Anal*, 7(3):283–91, 2003.
- [128] F. Liu, Y. Hu, Q. Zhang, R. Kincaid, K. A. Goodman, and G. S. Mageras. Evaluation of deformable image registration and a motion model in ct images with limited features. *Phys Med Biol*, 57:2539–2554, 2012.
- [129] R. Kashani, K. Lam, D. Litzenberg, and J. Balter. Technical note: a deformable phantom for dynamic modeling in radiation therapy. *Med Phys*, 3:199–201, 2007.
- [130] M. Serban, E. Heath, G. Stroian, D. Louis Collins, and J. Seuntjens. A deformable phantom or 4d radiotherapy verification: design and image registration evaluation. *Med Phys*, 35:1094–102, 2008.
- [131] J. Chang, T. S. Suh, and D. S. Lee. Development of a deformable lung phantom for the evaluation of deformable registration. *J App Clin Med Phys*, 11(1):281–86, 2010.

- [132] WP Segars. Development of a new dynamic nurbs-based cardiac-torso (ncat) phantom, phd dissertation. The University of North Carolina, 2001.
- [133] W. P. Segars, G. Sturgeon, S. Mendonca, J. Grimes, and B. M. W. Tsui. 4d xcat phantom for multimodality imaging research. *Phys Med Biol*, 37(9):4902– 15, 2010.
- [134] X. G. Xu, T. C. Chao, and A. Bozkurt. Vip-man: an image-based whole-body adult male model constructed rom color photographs of the visible human project for multi-particle monte carlo calculations. *Health Physics*, 78(5):476–86, 2000.
- [135] B. Zhang, J. Ma, L. Liu, and J. Cheng. Cnman: a chinese adult male voxel phantom constructed from color photographs of a visible anatomical data set. *Radiation Protection Dosimetry*, 124(2):430–36, 2007.
- [136] P. Jannin, J. M. Fitzpatrick, D. J. Hawkes, X. Pennec, R. Shahidi, and M. W. Vannier. Validation of medical image processing in image-guieded therapy. IEEE Trans Med Imaging, 21:1445–9, 2002.
- [137] D. Yang, J. Hubenschmidt, S. Goddu, P. Parikh, J. Deasy, D. Low, and I. El Naqa. A biomechanical phantom for validation of deformable multimodality image algorithms. *Med Phys*, 24:2636, 2007.
- [138] J. Hutchinson. On the capacity of the lungs, and on the respiratory functions, with a view of establishing a precise and easy method of detecting disease by the spirometer. J. Royal Soc. Med., 29:137–252, 1846.
- [139] J. G. Ziegler and N. B. Nichols. Optimum setting or automatic controllers. Trans. ASME, 64:759–768, 1942.
- [140] Joachim Weickert and Hanno Scharr. A scheme for coherence-enhancing diffusion filtering with optimized rotation invariance. *Journal of Visual Communication and Image Representation*, 13(1):103 118, 2002.
- [141] T.C. Lee and R. L. Kashyap. Building skeleton models via 3-d medial surface/axis thinning algorithms. CVGIP: Graphical Models and Image Processing, 56(6):462–478, 1994.
- [142] K. Nallaperumal, A. L. Fred, and S. Padmapriya. A novel technque for fingerprint feature extraction using fixed size templates. *INDICON*, 2005 Annual IEEE, pages 371–374, 2005.

- [143] T. Chan and L. Vese. Active contours without edges. In *Proceeding of the Second International Conference*, Scale-Space '99, pages 141–151. Nielsen, 1999.
- [144] Y. Zhang, B. J. Matuszewski, L.-K. Shark, and C. J. Moore. Medical image segmentation using new hybrid level-set method. *IEEE International Conference on Biomedical Visualization*, pages 71–76, July 2008.
- [145] T. Vercauteren, X. Pennec, A. Perchant, and N. Ayache. Diffeomorphic demons using itk's finite difference solver hierarchy. 11 2008.
- [146] S. Pirozzi, J. Piper, A. Nelson, M. Duchateau, D. Verellen, and M. De Riddler. A novel framework for user-intervened correction of deformable registration. *IJROBP*, 87(2):S144, 2013.
- [147] R. Castillo, E. Castillo, and R. Guerra et al. A framework for evaluation of deformable image registration spatial accuracy using large landmark point sets. *Phys Med Biol*, 54(7):1849–70, 2009.
- [148] Y. Ou, H. Akbari, M. Bilello, X. Da, and C. Davatzikos. Comparative evaluation of registration algorithms in different brain databases with varying difficulty:results and insights. *IEE Trans Med Imaging*, 33(10):2039–2065, 2014.
- [149] J. K. Kearney, W. B. Thompson, and D. L. Boley. Optical flow estimation: An error analysis of gradient-based methods with local optimization. *IEEE Transactions on Pattern Analysis and Machine Intelligence*, PAMI-9(2):229–244, 1987.
- [150] J. Kalpathy-Cramer, B. Zhao, D. Goldgof, Y. Gu, X. Wang, H. Yang, Y. Tan, R. Gillies, and S. Napel. A comparison of lung nodule segmentation algorithms: methods and results from a multi-institutional study. *J Digit Imaging*, pages 1–12, Feb 2016.
- [151] B. H. Menze, A. Jakab, and S. Bauer et al. Developing a methodology for three-dimensional correlation of pet-ct images and whole-mount histopathology in non-small-cell lung cancer. *IEEE Trans Med. Im.*, 34(10):1993–2024, 2015.
- [152] J. A. Tanyi and M. H. Fuss. Volumetric image-guidance: Does routine usage prompt adaptive re-planning? An institutional review. *Acta Oncol*, 47:1444– 53, 2008.

- [153] A. Z. Kibrom and K. A. Knight. Adaptive radiation therapy for bladder cancer: a review of adaptive techniques used in clinical practice. *J. Med. Radiat. Sci.*, 62:277–85, 2015.
- [154] Systematic evaluation of three different commercial software solutions for automatic segmentation for adaptive therapy in head-and-neck, prostate and pleural cancer. *Radiation Oncology*, 7:160, 2012.
- [155] M. R. Kaus, S. K. Warfield, A. Nabavi, P. M. Black, A. Jolesz, and R. Kikinis. Automated segmentation of MR images in brain tumors. *Radiology*, 218:586–591, 2001.
- [156] M. Chao, S. Bhide, and H. Chen et al. Reduce in variation and improve efficiency of target volume delineation by a computer-assisted system using a deformable image registration approach. *Int. J. Rad. Oncol. Biol. Phys.*, 68:1512–1521, 2007.
- [157] M. Erdt, S. Steger, and G. Sakas. Regmentation: a new view of image segmentation and registration. *Journal of Radiation Oncology Informatics*, 1(1):1 23, 2012.
- [158] Daniel Markel, Habib Zaidi, and Issam El Naqa. Novel multimodality segmentation using level sets and jensen-rnyi divergence. *Medical Physics*, 40(12):–, 2013.
- [159] R. W. Floyd and L. Steingberg. An adaptive algorithm for spatial gray scale. In International Symposium of Technical Papers, page 36. Society for Information Displays, 1975.
- [160] Q. Fang and D. Boas. Tetrehedral mesh generation from columetric binary and gray-scale images. In *Proceedings of IEEE International Symposium on Biomedical Imaging*, pages 1142–1145, 2009.
- [161] Yao Wang and O. Lee. Use of two-dimensional deformable mesh structures for video coding i. the synthesis problem: mesh-based function approximation and mapping. *Circuits and Systems for Video Technology, IEEE Transactions on*, 6(6):636–646, Dec 1996.
- [162] A. Bhuiyan, B. Nath, J. Chua, and K. Ramamohanarao. Automatic detection of vascular bifurcations and crossovers from color retinal fundus images. In

- Signal-Image Technologies and Internet-Based System, 2007. SITIS '07. Third International IEEE Conference on, pages 711–718, Dec 2007.
- [163] H. Chui and A. Rangarajan. A new point matching algorithm for non-rigid registration. *Computer Vision and Image Understanding*, 89:114–141, 2003.
- [164] P. Massoumzadeh, O. A. Earl, and B. R. Whiting. Noise simulation in x-ray CT. *Medical Imaging*, 5745:898–909, 2005.
- [165] Bruce D. Lucas and Takeo Kanade. An iterative image registration technique with an application to stereo vision. pages 674–679, 1981.
- [166] Miet Loubele, Frederik Maes, Filip Schutyser, Guy Marchal, Reinhilde Jacobs, and Paul Suetens. Assessment of bone segmentation quality of cone-beam {CT} versus multislice spiral ct: a pilot study. Oral Surgery, Oral Medicine, Oral Pathology, Oral Radiology, and Endodontology, 102(2):225 234, 2006.
- [167] A. Behnaz, J. Snider, C. Eneh, G. Esposito, E. Wilson, Z. Yaniv, E. Cohen, and K. Cleary. Quantitative ct for volumetric analysis o medical images: initial results for liver tumors. In *Proc. SPIE 7623, Medical Imaging 2010: Image Processing*, volume 76233U, 2010.
- [168] U. Vovk, F. Pernus, and B. Likar. A review of methods for correction of intensity inhomogeneity in mri. *IEEE Transactions on Medical Imaging*, 26(3):405–421, 2007.
- [169] L. A. Vese and T. F. Chan. A multiphase level set framework for image segmentation using the mumford and shah framework. *International Journal of Computer Vision*, 50(3):271–293, 2002.
- [170] D. F. Pace, S. R. Aylward, and M. Niethammer. A locally adaptive regularization based on anisotropic diffusion for deormable image registration of sliding organs. *IEEE Transactions on Medical Imaging*, 32(11):2114–2126, 2013.
- [171] von hagens plastinations. http://www.vonhagens-plastination.com/teaching-specimens. Accessed: 2016-06-09.